UNIVERSITY OF ROCHESTER
LABORATORY FOR LASER ENERGETICS

Volume 61
October–December 1994
DOE/SF/19460-58

LLE Review

Quarterly Report

UR
LLE

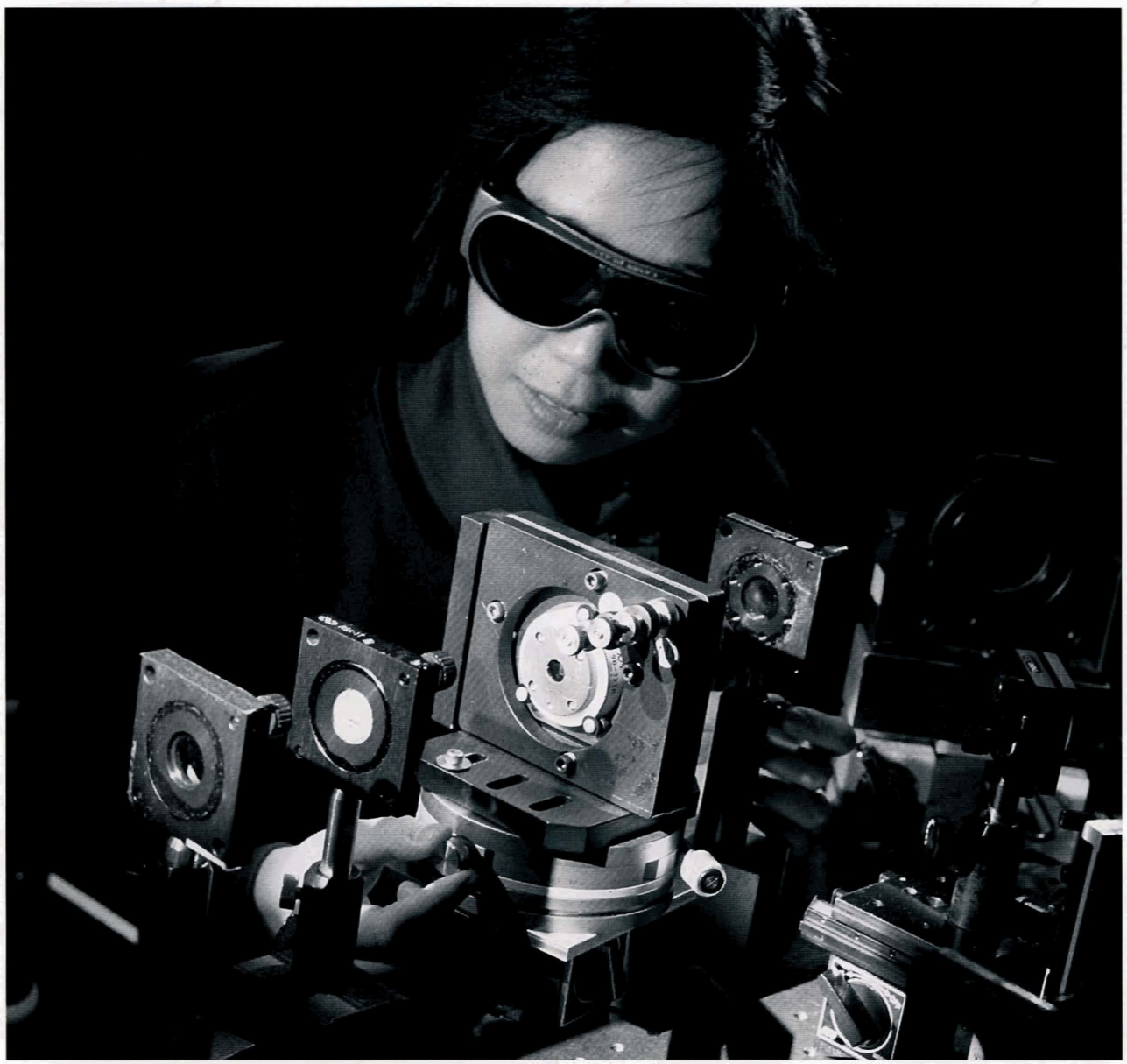

About the Cover:

Graduate student Lily Li Zheng makes final adjustments to a KDP crystal prior to measuring the group-velocity walkaway (GVW) of ultrashort pulses, using a novel frequency-domain interferometer setup. This new technique has the advantage of allowing GVW measurements to be made directly and in real-time, which is useful for nonlinear frequency conversion applications in which the GVW can be controlled by crystal tuning.

The work described in this volume includes current research at the Laboratory for Laser Energetics, which is supported by New York State Research and Development Authority, the University of Rochester, the U.S. Department of Energy Office of Inertial Confinement Fusion under Cooperative Agreement No. DE-FC03-92SF19460, and other agencies.

Printed in the United States of America
Available from
National Technical Information Services
U.S. Department of Commerce
5285 Port Royal Road
Springfield, VA 22161

Price codes: Printed Copy A04
Microfiche A01

For questions or comments, contact Kenneth L. Marshall, *Editor*, Laboratory for Laser Energetics, 250 East River Road, Rochester, NY 14623-1299, (716) 275-8247.

UNIVERSITY OF ROCHESTER
LABORATORY FOR LASER ENERGETICS

Volume 61
October–December 1994
DOE/SF/19460-58

LLE Review

UR LLE

Quarterly Report

Contents

In Brief

This volume of the LLE review, covering the period of October–December 1994, contains articles on a diagnostic method employing krypton spectroscopy for measurement of temperature and shell-fuel mixing in high-temperature implosions; the first direct assessment of the ion-acoustic decay instability in a large-scale-length, hot plasma; measurements of polarization mode dispersion and group-velocity walkaway in birefringent media using a frequency domain interferometer; an evaluation of the magnetic flux dynamics occurring in an optically triggered, thin-film superconducting switch; the effect of slurry fluid chemistry on particle size distribution during aqueous polishing of optical glass; and the influence of thermal and mechanical processing history in the preparation of well-ordered liquid crystal elastomer systems.

Highlights of the research presented in this issue are

- The addition of ~0.01 atm of krypton gas to the fuel allows the implosion temperature to be conveniently diagnosed through the spectrum of helium-like (Kr^{+34}) and hydrogen-like (Kr^{+35}) lines. The ratio of intensities for the two Kr lines as a function of temperature is sufficient to allow temperature measurements of up to ~10 keV with a maximum error of $<\pm 10\%$.

- The electron plasma wave excited by the ion-acoustic decay instability was observed directly using a novel Thomson scattering diagnostic. The electron temperature in the interaction region, as determined from the frequency of the detected wave obtained using this diagnostic, is in reasonably good agreement with the value predicted by computer simulations.

- A new technique based on frequency domain interferometry for the direct measurement of polarization mode dispersion (PMD) in birefringent media was used experimentally to determine the group velocity walkaway (GVW) of short pulses in nonlinear optical crystals. Experimental measurements of walkaway dependence versus propagation angle in KDP-II crystals using this technique fit the theoretical prediction based on the material dispersion to within an accuracy of $\pm 10\%$.

- A theoretical model of the flux dynamics in an optically irradiated YCBO thin-film superconducting switch has been developed and experimentally verified. Both the magnitude of the peak switched voltage in the secondary coil and its response time show a marked dependence on the intensity of the laser pulse used to initiate switching.

- The slurry charge control effect, a relationship between the polishing slurry pH and the isoelectric point (IEP) of the polishing agent, was identified and established as a key process parameter for the rapid production of high-quality optical surfaces from silica-based glass types. Combinations of slurry fluids and polishing agents in which the fluid pH value was larger than the polishing agent IEP consistently produced surfaces with the lowest surface roughness through inhibition of suspended particle agglomeration and enhanced dissolution of in-process glass constituents.

- The ability to readily induce uniform bulk molecular alignment in liquid crystalline polysiloxane elastomeric films by application of mechanical forces during the final crosslinking stage has been demonstrated. X-ray diffraction data indicate that an externally imposed stress or strain is critical in achieving a monodomain nematic character, and that alignment uniformity is retained after repeated thermal cycling from the nematic-isotropic phase transition ($T_{n\text{-}i}$) to room temperature.

Kenneth L. Marshall
Editor

Krypton Spectroscopy Diagnosis of High-Temperature Implosions

High-temperature implosions are planned for the OMEGA Upgrade experimental program. By using relatively thin shell targets, temperatures much higher than 1 keV at modest compressed densities (~1 to 5 g/cm^3) are predicted. The goal of this work is to demonstrate that by adding a small admixture of krypton gas (~0.01 atm) to the fuel, the temperature can be conveniently diagnosed through the spectrum of helium-like (Kr^{+34}) and hydrogen-like (Kr^{+35}) lines. By increasing the fill pressure, resonant Kr lines can become opaque, through self-absorption, and their relative intensities can be used to diagnose shell-fuel mixing.

As an example of predicted high-temperature implosion on the OMEGA Upgrade system, in Fig. 61.1 we show temperature and density profiles, at peak compression, calculated by the *LILAC* code for a CH shell of 1-mm diameter and 10-μm thickness, filled with a 10-atm pressure of DT. Typical Upgrade laser parameters (laser energy of 30 kJ in a Gaussian pulse of 650-ps width) were assumed. As Fig. 61.1 shows, the core temperature and density are fairly uniform at ~5 keV and ~4.5 g/cm^3, respectively. In the analysis that follows, the core profiles will be assumed to be uniform as well. The relatively high temperature of the shell is expected to play an important role in transmitting core radiation.

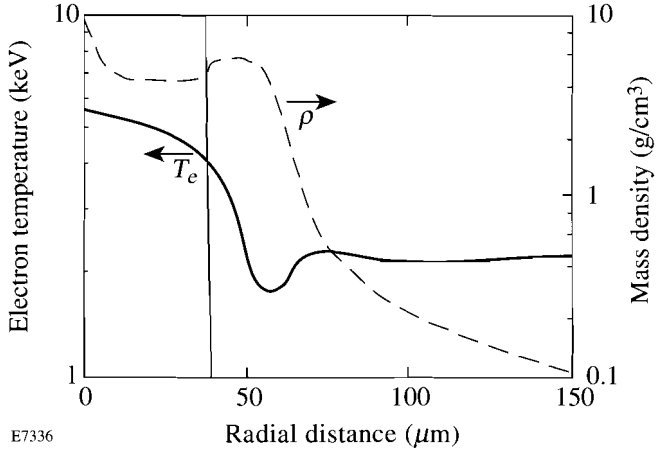

Figure 61.1
Electron temperature and mass density at peak compression, predicted by *LILAC*, for a DT-filled, high-temperature implosion on the OMEGA Upgrade system. The vertical line marks the fuel-shell interface.

Observation of K-Shell Krypton Lines

The wavelengths and transition probabilities of Kr lines are not fully known from the literature. We have used atomic data calculated by M. Klapisch,[1] using a detailed relativistic atomic structure code that includes intermediate coupling, higher-multipole interactions, and many-body and QED effects. The K-shell lines are of much shorter wavelength than past spectral line emission from laser targets; for example, the Kr^{+34} resonance line has a wavelength[1] of 0.94538 Å, or photon energy of 13.11347 keV. For this reason, we addressed the question of observability of these lines. A simple way to estimate the expected intensity of krypton lines is to make a comparison with past experiments on argon-filled targets. In recent experiments on OMEGA, strong helium-like and hydrogen-like argon lines were observed when the argon fill pressure was 0.1 atm (in 20-atm deuterium).[2] In other experiments the argon fill pressure was as low as 0.01 atm but still yielded significant spectral intensity. We chose to calculate the intensity of K-shell krypton lines using the corona approximation. This approximation was used to show only the intensity scaling; for the temperature-determination curves, the more general collisional-radiative model was used. The corona approximation is valid in the limit of low density, high temperature, and high nuclear charge Z, while the converse is true for the LTE approximation. The condition for the applicability of the corona model to excited states can be written as [Eq. (6-55) in Ref. 3]

$$N_e\left(\mathrm{cm}^{-3}\right) \ll 10^{18}\left(Z^7/n^{17/2}\right)\left(kT/E_i\right)^{1/2}, \qquad (1)$$

where E_i is the ionization energy and n is the highest principal quantum number for which the model applies. For helium-like krypton (of energy of ionization[4] E_i = 17.296 keV) and the predicted densities of up to $N_e \sim 10^{24}$ cm^{-3} ($\rho \sim 4$ g/cm^3), the model applies to quantum numbers n of up to at least $n = 3$, over the entire 1- to 10-keV temperature range. In the corona

approximation, the line intensity is given by the rate of excitation by electron collisions:[5]

$$I_\nu = h\nu\langle\sigma_{\text{exc}}v\rangle N_i N_e$$
$$= 1.6\times10^{-5} f\langle g\rangle N_e\left[\Delta E(kT)^{1/2}\right]^{-1}\exp\left[-(\Delta E/kT)\right], \qquad (2)$$

where ΔE is the excitation energy, N_i and N_e are the densities of emitting ions and electrons, respectively, f is the absorption oscillator strength, and $\langle g\rangle$ is the Maxwellian-averaged Gaunt factor[5] (kT and ΔE are in eV). Thus, if the ratio $\Delta E/kT$ is maintained when krypton is used instead of argon, the intensity of the same transition should drop by a factor of ~8 since ΔE increases by a factor of 4. The actual drop in intensity would be much smaller for the following reasons: (a) For argon, Eq. (2) would yield an overestimate of the intensity since in the corona approximation every excitation leads to a photon emission, while for argon some of the excitations result in super-elastic collisions with free electrons; (b) whereas the predicted compressed density is comparable to what was achieved with argon, the krypton targets will be bigger and thus contain more mass (by a factor of ~64) for the same fill pressure. This leads to the conclusion that the strong K-shell krypton lines will be readily observable for temperatures ≥ 3 keV.

Supportive evidence can be found in the fact that the resonance line of Kr^{+34} (at 0.94538 Å) was easily observable on previous short-pulse (100-ps) experiments[6] on OMEGA, using a Von-Hamos focusing spectrometer. The peak laser power in those experiments was ~6 TW, which is much lower than that of the OMEGA Upgrade (~30 TW).

Determination of Temperature by Line-Intensity Ratio

We now calculate the temperature dependence of a particular Kr line-intensity ratio under steady-state conditions, using the collisional-radiative atomic code POPION.[7] Although the corona model is largely applicable for the cases under discussion, as was mentioned previously, the collisional-radiative model is more precise. For example, we examined the calculated relative specie and level populations for Kr^{+34} and Kr^{+35} ions. In Fig. 61.2 we show examples of level populations in Kr^{+34} (helium-like krypton); the sum of populations in all levels of krypton ions adds up to 1. The ground-level population (especially at the higher temperatures) is essentially independent of the electron density N_e, which is a characteristic of the corona model [see Eq. (6-95) in Ref. 3]. At lower temperatures, the relative ground-level population approaches an inverse dependence on N_e, which in turn is a characteristic of the LTE model [as can be seen from the Saha equation, Eq. (6-29) in Ref. 3]. Also, the $n = 2$ population increases like N_e—also a characteristic of the corona model. The latter can be seen from Eq. (2), by equating I_ν with $h\nu\, N_i\, Q_n$, where Q_n is the relative level population in the level n. On the other hand, at the lower temperatures the $n = 2$ level population approaches independence of N_e, a characteristic of the LTE model (where relative level populations depend only on the temperature, through the Boltzmann factors). Thus, to cover the whole relevant parameter space, a full collisional-radiative model is necessary.

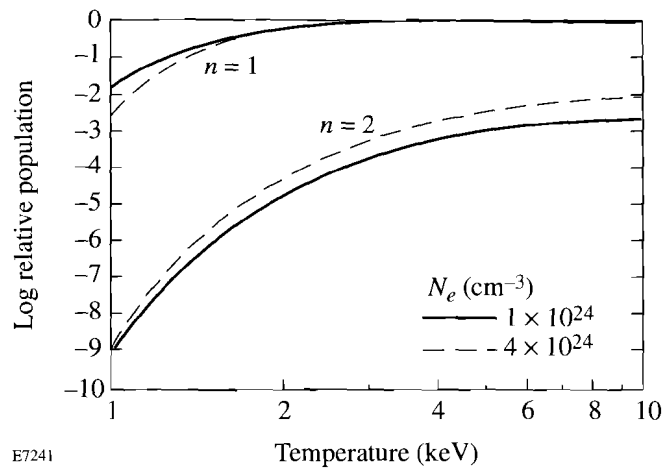

Figure 61.2
Relative populations in levels of Kr^{+34} (helium-like krypton), as calculated by the POPION[7] atomic code. The sum of populations in all levels of krypton ions adds up to 1.

For a temperature-sensitive line-intensity ratio we choose the ratio of a hydrogen-like line to a helium-like line. To minimize opacity effects we use the following two lines: (a) the Lyman-α line of Kr^{+35} of wavelength 0.9196 Å,[8] and (b) the helium-β line of Kr^{+34} of wavelength 0.8033 Å and absorption oscillator strength 0.1293.[1] We must show that the opacity of these lines will be negligible for the method to be applicable. We concentrate on the helium-β line since the opacity of the Lyman-α line is much smaller. The line opacity at an energy separation δE from the unperturbed position can be expressed as [see Eq. (8-14) in Ref. 3]

$$\tau(\delta E = 0) = \left(\pi e^2 h/Mmc\right)P(\delta E = 0) f\, \rho R\, \varepsilon Q_n, \qquad (3)$$

where M is the krypton ionic mass, $P(\delta E)$ is the line profile at δE in inverse energy units, f is the absorption oscillator

strength of the line, ρR is the total areal density (mostly that of the fuel), ε is the fraction of krypton in the fuel (by mass), and Q_n is the fraction of krypton ions in the absorbing level (i.e., the lower level of the transition). For unshifted lines one usually calculates $\tau_0 = \tau(\delta E = 0)$, but for the helium-$\beta$ line, which is shifted by the Stark effect, we designate τ_0 as the maximum opacity at the shifted peak position. In either case, $P(0) \sim 1/\Delta E$, where ΔE is the line width. We assume the addition of 0.01 atm krypton to the DT-filled target implosion that was simulated in Fig. 61.1. In that implosion the DT fill pressure was 10 atm, and the total ρR at peak compression was ~16 mg/cm^2. According to the POPION code results (Fig. 61.2), Q_1 for helium-like Kr over a wide temperature range is very close to 1.

Next we need to estimate the line width, which is related to $P(0)$ in Eq. (3) as explained previously. The code results of Fig. 61.1 show that the ion temperature at peak compression is about twice the electron temperature, or $T_i \sim 10$ keV, for which the Doppler width of the helium-β line is about 12.9 eV. A rough estimate of the Stark width of the Kr^{+34} helium-β line can be obtained by noting that for a given density and temperature the Stark width is proportional to $1/Z$. More specifically, the scaling for the Stark width of hydrogenic lines is[11] given by $\Delta E \sim \left(Z_p/Z\right)\left(n_i^2 - n_f^2\right)N_p^{2/3}$, where Z_p and N_p are respectively the nuclear charge and ion density of the perturber, Z is the nuclear charge of the emitter, and n_i, n_f are the principal quantum numbers of the initial and final levels of the transition. Although the ion under discussion is helium-like, the Stark width of the upper level, $1s3p\,^1P$, turns out to exceed the separation to the nearby $1s3d\,^1D$ level, which makes the transition close to hydrogenic (i.e., the level splitting increases linearly with the perturbing field as in single-electron ions). The above formula for the Stark width is only approximate and does not include such effects as perturbers correlation. However, we use its Z scaling only for extrapolating the detailed calculations[10] for the same transition in argon at the same density and ignore the weak temperature dependence of the Stark broadening. The Stark width of the Kr^{+34} helium-β line at $\rho = 4.5$ g/cm^3 is thus estimated to be ~17 eV. Convolving this Stark width with the Doppler width yields a total width of ~26 eV, from which the normalized composite profile yields the value of $P(\delta E)$. Substituting these values into Eq. (3) yields an optical depth for the helium-β line of $\tau_0 \sim 0.56$. This opacity value was estimated for an electron temperature of 5 keV ($T_i \sim 2\,T_e$) and density of 4.5 g/cm^3. For other temperatures (but the same doping fraction) the opacity will not change appreciably because (1) Q_1 is weakly dependent on T in the range T_e ~3 to 10 keV (see Fig. 61.2), and (2) the linewidth depends mainly on the density. For other densities the opacity will vary as $\sim\rho^{-2/3}$ due to the change in linewidth. The opacity of the Lyman-α line of Kr^{+35} is much smaller than that of the helium-β line because the ratio of Kr^{+35} to Kr^{+34} ground-state populations at $N_e = 10^{24}$ cm^{-3} varies over the 1- to 10-keV temperature range from $\sim 10^{-10}$ to $\sim 10^{-1}$.

The curves in Fig. 61.2 and the temperature curves calculated below assume a steady-state situation. To justify this assumption we show in Fig. 61.3 the calculated ionization time t_i of the Kr^{+34} ion as a function of temperature for $N_e = 10^{24}$ cm^{-3}; t_i depends inversely on N_e and is given by $t_i = \left(\langle\sigma_{\text{ion}}v\rangle N_e\right)^{-1}$. The ionization rate was taken as[11]

$$\langle\sigma_{\text{ion}}\rangle = 2.5\times10^{-6}\,\eta\,E_i^{-3/2}\left(kt/E_i\right) \times \left[1+\left(kT/E_i\right)\right]^{-1}\exp\left[-\left(E_i/kT\right)\right], \quad (4)$$

where E_i is the ionization energy (in eV) and η is the number of outer-shell electrons ($\eta = 2$ for helium-like ions). The time constant for approaching a steady state of level populations for a given set of hydrodynamic conditions is given by t_i since t_i is the slowest of the relevant processes. An example can be found in the excitation rate from the ground level to the 2^1P level of Kr^{+34}, which is faster than the ionization rate by a factor that varies from ~700 at the low end of the temperature range to ~3 at the higher end. We see from Fig. 61.3 that for a value of T of 5 keV, the ionization time t_i is ~50 ps, which is about the time period t_{peak} predicted for the volume-averaged temperature to be within ~90% of its peak value. Thus, the

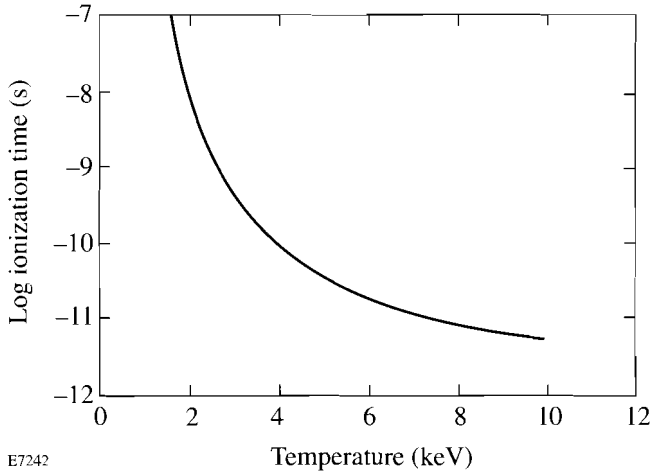

Figure 61.3
Calculated ionization time t_i of Kr^{+34} as a function of temperature, for $N_e = 10^{24}$ cm^{-3}. The ionization time serves as a time constant for approaching a steady state of level populations for a given set of hydrodynamic conditions.

density of hydrogen-like ions will reach only the fraction $\left[1-\exp\left(-t_{\text{peak}}/t_i\right)\right] \sim 0.63$ of its steady-state value. Neglecting this effect will result in an underestimate of the temperature (in the above example, 4.6 keV instead of 5 keV). An underestimate will also result if the spectral measurement is not time resolved, since the emission time of helium-like lines will be longer than that of hydrogen-like lines.

We show in Fig. 61.4 the calculated intensity ratio of the Lyman-α line of Kr^{+35} to the helium-β line of Kr^{+35} as a function of temperature for two electron-density values. Clearly, the intensity-ratio change is sensitive to temperature, but the Lyman-α line may be too weak to be observed for temperatures smaller than ~4 keV. In going from $T = 10$ keV to $T = 4$ keV, both the ratio in Fig. 61.4 and the intensity of the helium-β line drop by an order of magnitude, which causes the intensity of the Lyman-α line to drop by two orders of magnitude. Over a wide density range (changing by a factor of 20), the temperature-dependence curve changes very little. This behavior is due to the close resemblance to the corona model, where the line ratio is completely independent of density. If we know the density to be within this range, the maximum error in determining the temperature would be less than ±10%. The required precision in the intensity measurements is modest: to achieve a ±10% precision in the temperature, the intensity ratio must be measured with a precision of only a factor of ~3 (at $T = 4$ keV) or a factor of ~2 (at $T = 6$ keV). The attenuation of these two lines through the compressed CH polymer shell is of no concern, as a cold $\rho\Delta R$ of more than 1 g/cm^2 is needed to significantly attenuate them.

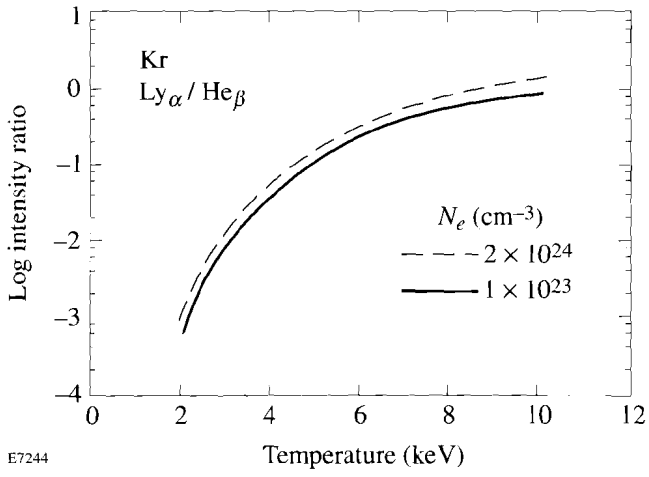

Figure 61.4
Intensity ratio of the Lyman-α line of Kr^{+35} to the helium-β line of Kr^{-35} as a function of temperature at two electron-density values. The opacity of both lines, which was shown to be small, was neglected.

Mixing Diagnosis Based on High-Opacity Kr Lines

In the previous section the opacity of the helium-β line of Kr^{+34} for a fill pressure of 0.01 atm was shown to be smaller than 1 ($\tau_0 \sim 0.56$), and thus negligible. We now examine the case of much higher fill pressures, where the helium-β line is optically thick at peak compression. Although the intensity ratio in Fig. 61.4 is then not applicable, a different type of information can be obtained on the target behavior. Anticipating the last section, we choose the helium-β line rather than the higher-opacity helium-α line.

The intensity of an optically thick line emerging from the plasma volume is related to the escape factor parameter, which has been the subject of numerous publications.[12–15] The escape factor G is defined by

$$G(\tau_0) = \int_{-\infty}^{\infty} P(\delta E)\exp\left[-\tau_0 P(\delta E)/P(\delta E = 0)\right] d(\delta E), \quad (5)$$

where $G(\tau_0)$ in spherical geometry corresponds to a point source at the center of the sphere and τ_0 is the opacity over the radius. For a source uniformly distributed over the sphere, Mancini *et al.*[15] have shown that $G(\tau_0)$ is twice as big as the point-source case and depends primarily on the type of line profile. For example, for a Gaussian (i.e., Doppler) profile, $G(\tau_0)$ does not depend explicitly on the linewidth; for $\tau_0 >> 1$, $G(\tau_0) \sim 1/\left(\pi \ln \tau_0\right)^{1/2} \tau_0$. For Stark profiles the corresponding asymptotic relation was found to be $G(\tau_0) \sim 1/{\tau_0}^{3/5}$. For example, a Holtzmarkian profile (the simplest approximation to a Stark profile) yields the universal asymptotic expression[12]

$$G(\tau_0) = 0.451/{\tau_0}^{3/5} \qquad (\tau_0 >> 1). \quad (6)$$

Mancini *et al.*[15] have calculated $G(\tau_0)$ for the Lyman-α line of argon using complete Stark profiles. They showed that for an accurate value of G, a detailed calculation with an actual Stark profile should be performed. However, their curves (for a point source) can still be approximated by Eq. (6) if G is expressed as a function of τ_0, rather than as a function of $\tau_0/P(\delta E = 0)$, because an approximate Stark profile that changes only the line width without changing the profile shape will not affect Eq. (6).

A measurement of the escape factor of a high-opacity line can yield the value of τ_0, using Eq. (6) or the equivalent result of a more detailed calculation.[15] As Eq. (3) shows, τ_0 depends on ρR and, through $P(\delta E)$, on ρ. For a high-opacity line, most of the emergent intensity is located in the far wings of the

spectral profile. Because the Doppler profile drops much faster than the Stark profile, the wings are dominated by the latter, although the two separate linewidths are comparable. For this reason we consider the escape factor for a purely Stark profile. For the helium-β line, $P_0 = P(\delta E = 0) \sim \rho^{-2/3}$, when the density is high enough to merge the $1s3p$ and $1s3d$ levels, which we have argued to be the case here. For the crude estimate of 17-eV Stark width, this relationship reads

$$P_0\left(\mathrm{eV}^{-1}\right) = 0.15\,\rho^{-2/3}, \tag{7}$$

where, as explained, P_0 refers to the peak of the profile rather than to the line center. On the other hand, in an imploding spherical target

$$\rho R = \left(3M_F/4\pi\right)^{1/3}\rho^{2/3} \tag{8}$$

in terms of the total fill mass (fuel and krypton) M_F. Thus τ_0 is independent of the target compression because the opacity increases with increasing ρR but decreases due to the increasing width (or decreasing P_0). The two quantities change as $\rho^{2/3}$ and cancel each other's effect on τ_0.

The foregoing discussion shows that measuring the escape factor cannot yield information on the density or ρR. Mixing of shell material into the fuel, however, does affect the escape factor measurement because the ρR deduced from the absorption of Kr lines yields the ρR of only the fuel $(\rho R)_F$, whereas the Stark profile depends on the total density ρ_T, including shell material mixed into the fuel. Combining Eqs. (3), (7), and (8), we can relate the volume-averaged fraction of density due to mixing $\xi = \rho_{\mathrm{mix}}/\rho_F$ to τ_0:

$$1 + \xi = \left[0.15\,\pi e^2 h\, f\left(eM_F/4\pi\right)/\left(mMc\,\tau_0\right)\right]^{3/2}. \tag{9}$$

We can understand the effect of mixing on the opacity as follows: Without mixing, the opacity τ_0 is approximately constant during the compression because of the two opposing effects: (1) increase in the ρR of absorbing ions and (2) increase in the linewidth. The mixed shell material is involved only in the second effect, which causes a net reduction in the opacity.

The experimental determination of the mixing fraction consists of measuring the escape factor $G(\tau_0)$, deducing τ_0 from Eq. (6) (or from a more detailed equivalent thereof), and, finally, finding ξ from Eq. (9). In addition to using a crude Stark profile, Eq. (9) is correct only for a point source (central hot spot). As mentioned earlier, Mancini *et al.*[15] have shown that for a spherically uniform source, $G(\tau_0)$ is twice as big as for the point-source case. To determine which geometry conforms better to the experiment we can examine two experimental signatures: (a) for a uniform source, the core image size at high photon energy will be about the same as that at low photon energy, whereas for a hot-spot source the former will be much smaller than the latter; and (b) for a uniform source the observed line profile will be flat topped, whereas for a hot-spot source a self-reversal (or minimum) will be observed at the position of the profile peaks.

A Method for Measuring the Escape Factor

The escape factor of a line can be measured by comparing its measured intensity to that of another line, both of which have the same upper level. The first should have an opacity $\tau_0 >> 1$, the second $\tau_0 << 1$. The two helium-like Kr lines we selected are (a) the Lyman-β line, $1s3p\,^1P - 1s^2\,^1S$ (at 0.8033 Å) and (b) the Balmer-α line, $1s3p\,^1P - 1s2s\,^1S$ (at 5.0508 Å). Note that what we refer to here as Balmer-α is the helium-like, 3-2 transition that shares an upper level with the helium-β line (and not, for example, to the stronger $1s3d\,^1D - 1s2p\,^1P$ transition at 5.3463 Å). Previously, we mentioned the helium-α line corresponding to the $1s2p\,^1P - 1s^2\,^1S$ transition. For krypton ions, both the transitions to the ground level and the 3-2 transitions are easily accessible to x-ray measurement. Thus, for argon, the 3-2 transitions are too soft ($\lambda > 20$ Å) for common x-ray crystal instruments, and they also suffer very high opacity in traversing the target.

By making an appropriate choice of the krypton fill pressure, the opacity (for resonant absorption) of the Lyman-β line at peak compression will be >>1, while that of the Balmer-α will be <<1. It was estimated earlier that for a Kr fill pressure of 0.01 atm, the opacity τ_0 of the helium-β line will be ~0.5. Thus, for a fill pressure in the range of 0.1 to 1.0 atm, τ_0 will be in the range of 5 to 50. The opacity of the Balmer-α line will still be negligible since it is absorbed by ions in the $n = 2$ shell (whereas the helium-β line is absorbed by ground-level ions). Figure 61.2 shows that the population of $n = 2$ absorbing ions is smaller than that of $n = 1$ absorbing ions by several orders of magnitude. Due to the expected merging of the $1s3p\,^1P$ and $1s3d\,^1D$ levels, both ions in the $1s2p\,^1P$ and $1s2p\,^1S$ levels can absorb the broadened Balmer-α line; these constitute 1/3 of all $n = 2$ ions. With no merging, only 1/16 of the $n = 2$ ions can absorb the $1s3p\,^1P - 1s2s\,^1S$ transition. The high opacity of the resonance line $1s^2 - 1s2p\,^1P$

will also increase the $n = 2$ population (this effect is not included in Fig. 61.2).

In the absence of any absorption, the intensity ratio of these two lines I_{Ly}/I_{Ba} would simply be given by the ratio of the Einstein A coefficients (spontaneous emission probabilities) A_{Ly}/A_{Ba} and be independent of any atomic modeling. Since A (Lyman-β) = 4.453×10^{14} s^{-1} and A (Balmer-α) = 6.163×10^{12} s^{-1}, $A_{Ly}/A_{Ba} = 72.25$. In the case discussed here, the observed intensity ratio I_{Ly}/I_{Ba} will be lower than the ratio of the Einstein A coefficients A_{Ly}/A_{Ba}, by the escape factor G for the helium-β line. Thus, G can be found from

$$G = \left(I_{Ly}/I_{Ba}\right)/\left(A_{Ly}/A_{Ba}\right) = \left(I_{Ly}/I_{Ba}\right)/72.25. \quad (10)$$

It should be noted that the emergent intensity of a high-opacity line may not depend uniquely on the escape factor because of the possibility of re-emission of absorbed photons.[16] This is equivalent to allowing for the increased excited-level population (and thus emission) due to the absorption itself. In our case this effect is already included in the ratio of line intensity because the measured intensity of the optically thin Balmer-α line does reflect the actual excited-level population.

The nonresonant absorption by the target material (mostly the shell) should be negligibly small to insure the validity of this method. The attenuation of the Lyman-β line through the shell is negligible: it takes a $\rho\Delta R$ of ~1.8 g/cm^2 of cold CH to attenuate that line by $1/e$. On the other hand, the Balmer-α line will be attenuated by the same amount in going through only a $\rho\Delta R$ of ~5.5 mg/cm^2 of cold CH. Figure 61.1 shows that the shell at peak compression is hot enough to minimize this attenuation. The opacity of the CH shell at a wavelength λ, due to inverse bremsstrahlung absorption, is given by[17] $\tau = 2.23 \times 10^{-3} \lambda^3 (\rho\Delta R)\rho/T^{1/2}$, where λ is in Å and T in keV. For the target profiles of Fig. 61.1, the inverse bremsstrahlung opacity is $\tau \sim 0.014$. The opacity of CH due to photoionization is given by[17] $\tau = 0.54\ \lambda^3(\rho\Delta R)\Psi$, where Ψ is the fraction of carbon ions that are not stripped. Results from POPION calculations show that, at the given shell temperature and density values, $\Psi < 10^{-3}$ so that the photoionization opacity is $\tau < 10^{-3}$.

Finally we estimate the expected sensitivity of the method for measuring the degree of shell-fuel mixing. To find G from Eq. (10) with a precision of approximately ±20%, the relative intensity of each of the lines must be measured with a precision of ±10%, which requires the relative calibration of two instruments for the two very different wavelengths used here. A suitable procedure is as follows: the intensity ratio I_{Ly}/I_{Ba} for the case of a very low Kr fill pressure (~0.01 atm) is simply given by the known ratio A_{Ly}/A_{Ba}. Since, for Stark profiles, G depends[15] asymptotically on τ_0 like $1/\tau_0^{3/5}$, an error of ±20% in G will result in an error of ±33% in τ_0. Finally, finding the relative mixing from Eq. (9), this error translates into an error of ±50% in $1 + \xi$. Thus, the method is useful only for extensive mixing, where ξ is not much smaller than 1.

ACKNOWLEDGMENT

This work was supported by the U.S. Department of Energy Office of Inertial Confinement Fusion under Cooperative Agreement No. DE-FC03-92SF19460, the University of Rochester, and the New York State Energy Research and Development Authority. The support of DOE does not constitute an endorsement by DOE of the views expressed in this article.

REFERENCES

1. M. Klapisch (private communication).
2. B. Yaakobi, R. Epstein, F. J. Marshall, D. K. Bradley, P. A. Jaanimagi, and Q. Su, Optics Commun. **111**, 556 (1994).
3. H. R. Griem, *Plasma Spectroscopy* (McGraw-Hill, New York, 1964).
4. U. I. Safranova, Physica Scripta **23**, 241 (1981).
5. H. Van Regemorter, Astrophys. J. **136**, 906 (1962).
6. B. Yaakobi and A. J. Burek, IEEE J. Quantum Electron. **QE-19**, 1841 (1983).
7. R. Epstein, S. Skupsky, and J. Delettrez, J. Quant. Spectrosc. Radiat. Transfer **35**, 131 (1986).
8. G. W. Ericson, J. Phys. Chem. Ref. Data **6**, 831 (1977).
9. H. R. Griem, *Spectral Line Broadening by Plasmas* (Academic Press, New York, 1974).
10. C. F. Hooper (private communication).
11. H.-J. Kunze, A. H. Gabriel, and H. R. Griem, Phys. Rev. **165**, 267 (1968).
12. F. E. Irons, J. Quant. Spectrosc. Radiat. Transfer **22**, 1 (1979).

13. J. P. Apruzese, *ibid.* **34,** 447 (1985).

14. C. Chenais-Popovics, P. Alaterre, P. Audebert, J. P. Geindre, and J. C. Gauthier, *ibid.* **36**, 355 (1986).

15. R. C. Mancini, R. F. Joyce, and C. F. Hooper, Jr., J. Phys. B: At. Mol. Phys. **20**, 2975 (1987).

16. A. G. Hearn, Proc. Phys. Soc. (GB) **81**, 648 (1963).

17. B. Yaakobi, R. Epstein, and F. J. Marshall, Phys. Rev. A **44**, 8429 (1991).

Direct Measurements of the Ion-Acoustic Decay Instability in a Laser-Produced, Large-Scale, Hot Plasma

The final experiment carried out on the 24-beam OMEGA laser (in collaboration with scientists from Lawrence Livermore and the University of California, Davis) involved the investigation of the ion-acoustic decay instability (IADI) in large-scale-length (~1-mm), hot (~1-keV) plasmas.

In the IADI, an electromagnetic wave (i.e., an incident laser beam) decays into an electron plasma wave (epw) and an ion-acoustic wave (iaw), near the critical density n_c (where the electromagnetic wave frequency equals the plasma frequency). A unique feature of this experiment was the first direct observation of the epw using collective Thomson scattering (CTS). Further, it was possible from the spectral width of the CTS signal to estimate the electron temperature T_e in the plasma, the result ($T_e = 1.5$ keV) being in reasonably good agreement with the value (1.1 keV) predicted by the two-dimensional code *SAGE*.

The IADI[1] is a fundamentally important subject in plasma physics that has been studied by numerous authors in the context of laser-plasma interactions,[2,3] microwave experiments,[4] and ionospheric studies.[5] It is potentially significant in the large-scale plasmas relevant to laser fusion because anomalous electron heating can occur even when the instability is relatively weak, if the unstable volume is sufficiently large. In addition, the instability can lead to anomalous dc resistivity and a reduction in electron thermal transport, and it has an application as a critical surface diagnostic. Despite the significance of the IADI to large-scale plasmas, all previous experiments have been carried out in relatively small-scale plasmas.

In this article we present two original results: (1) the first direct observation of the epw excited by the IADI, and (2) the first study of the IADI in a plasma that approaches laser-fusion conditions, in the sense of having a density scale length of the order of 1 mm and an electron temperature T_e in excess of 1 keV. Previous observations of the epw's have been based on the second-harmonic emission, from which little can be inferred because the emission is produced by unknown pairs of epw's, integrated in a complicated way over wave-number space and real space. In contrast, we have directly observed the epw by using the 90°, collective Thomson scattering of a UV laser (at the third harmonic of the pump) from the epw's. Because the ratio of probe frequency to electron plasma frequency is only about 3, the scattering is collective (i.e., $k_{epw}\lambda_{De}$ is small, where k_{epw} is the epw wave number and λ_{De} is the Debye length), even though the scattering angle is large. The electron temperature can then be deduced from the ion sound velocity, obtained from the measurement of the frequency at which growth is maximum at the scattering wave number.

The experiments were carried out using a large-scale (~1-mm), hot (~1-keV) plasma[6] produced by the OMEGA laser in the geometry shown in Fig. 61.5. Two opposed sets of four UV beams, peaking at time $t = 1.0$ ns, were used to explode a polystyrene (CH) foil of 6-μm thickness and 600-μm diameter overcoated with 500 Å of Al. Four beams from each side were used as secondary heating beams and were incident later at $t = 1.6$ ns. The on-target laser energy was typically 50 to 60 J per beam with a pulse duration of 0.60 to 0.65 ns at a wavelength of 351 nm. One of the OMEGA beams was used as a 1.054-μm pump beam (at ω_0) to drive the IADI and timed to peak at $t = 2.2$ ns. This beam was incident through a phase plate with 3-mm cells and an *f*/3.6 lens to produce a focal spot of 210-μm diam (at half-maximum), with 36 J in the central Airy lobe, giving a maximum intensity in space and time of ~1.25×10^{14} W/cm^2. Another beam was attenuated and used as the $3\omega_0$ probe. A wave plate was used to rotate the (elliptical) polarization of the pump beam to the optimum angle for exciting the epw's being diagnosed. The typical plasma had a center density of 1 to 2×10^{21} cm^{-3}, which was maintained within a factor of 2 at $T_e \sim 1$ keV for approximately 1 ns. The scale length was of the order of 1 mm at $t = 2.2$ ns.

The scattering geometry is shown in Fig. 61.6. The CTS signal was collected by a focusing mirror at 90° to the Thomson scattering beam and focused onto the detector system (at the opposite port), which included a 1-m spectrometer, a UV streak camera, and a CCD camera. The measured wave vector

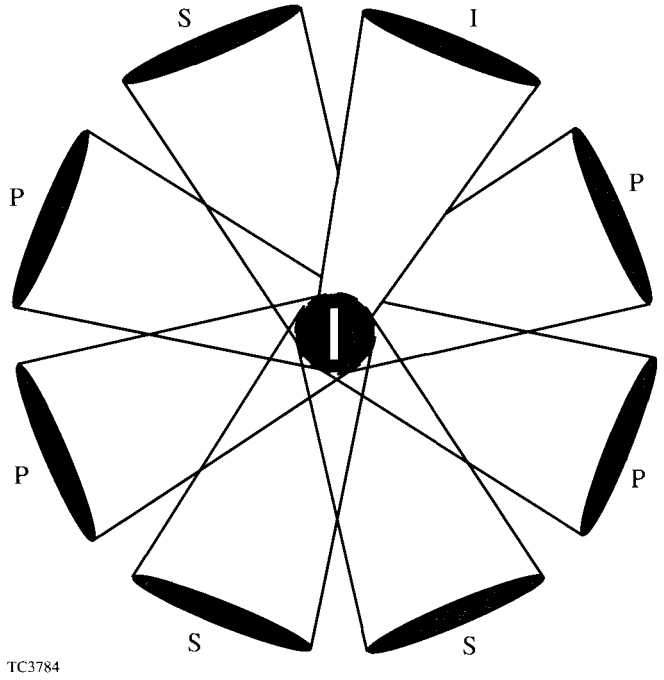

Figure 61.5
Configuration for long-scale-length plasma experiments. A plastic (CH) disk target is first irradiated by four near-normal-incidence, primary beams (P) from each side, forming an approximately spherical plasma. This plasma is then heated by four obliquely incident, secondary beams (S) from each side and one 1054-nm interaction beam (I). The interaction beam (shown shaded) is focused more tightly than the other beams.

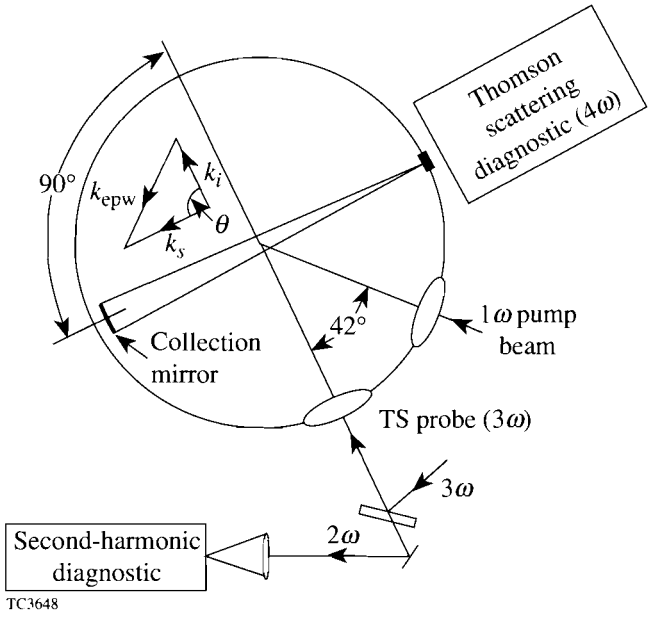

Figure 61.6
Schematic diagram of the experiment in the scattering plane. The IR pump beam is incident 6° below this plane. The initial target normal (the z axis of the simulations) is in the plane perpendicular to the scattering vector k_s and 69° below the scattering plane. It is also 69° from the pump beam. The k-matching diagram of the CTS is shown in the inset. Note that k_{epw} is nearly perpendicular to the pump laser.

k_{epw} was nearly parallel to the pump electric field. Simultaneously, the time-resolved, second-harmonic spectrum (through the Thomson-scattering port) was measured using a 1/3-m spectrometer, a streak camera, and another CCD camera.

Collective Thomson scattering[7] is a three-wave process satisfying the k-matching condition $k_s = k_i \pm k_{epw}$ and the energy conservation law $\omega_s = \omega_i \pm \omega_{epw}$. (The k's and ω's are the wave vectors and frequencies of the three waves; the subscripts i, s, and epw refer to the incident and scattered probe beam and the electron plasma wave.) We have measured the up-shifted signal at $4\omega_0 \left(= \omega_i + \omega_{epw}\right)$ to reduce the problems of incoherent harmonic emission and refraction. The scattering angle θ is given from the k-matching condition by $k_{epw}^2 = k_i^2 + k_s^2 - 2k_i k_s \cos\theta$. For the up-shifted scattering, we have $\omega_s \sim 4/3\ \omega_i$ and $k_s \sim 4/3\ k_i$. The geometry of the experiment selected a 90° scattering angle (Fig. 61.6) and $k_{epw} = 2.9 \times 10^5\ \text{cm}^{-1}$. At this angle the CTS signal intensity is maximum for out-of-plane polarization of the probe beam.[7] For $T_e \sim 1$ keV, the observed angle is close to the optimum scattering angle of 89° for measurement of the most unstable IADI mode, which has $k_{epw}\lambda_{De} \sim 0.23$. The density at which the observed k_{epw} is resonant for the IADI depends upon T_e, becoming higher as T_e decreases.

Our experiments were guided by two-dimensional calculations using the computer code *SAGE*.[8] Figure 61.7 shows spatial profiles of n_e, T_e, and ion temperature T_i along the center z axis at a time of 2.2 ns, corresponding to the peak of the pump beam. This timing was chosen so that the center plasma density would be slightly higher than the critical density $n_c \sim 10^{21}\ \text{cm}^{-3}$ of the pump laser. When the pump laser is applied to the preformed plasma, no significant density change is predicted, but the electrons in its path are heated by classical electron-ion collisions as is shown by the hump on the right-hand side of the T_e curve. The peak value of T_e is just above 1 keV. The *SAGE* calculations indicate that 15%–70% of the pump laser energy reaches the instability region, depending on the laser intensity.

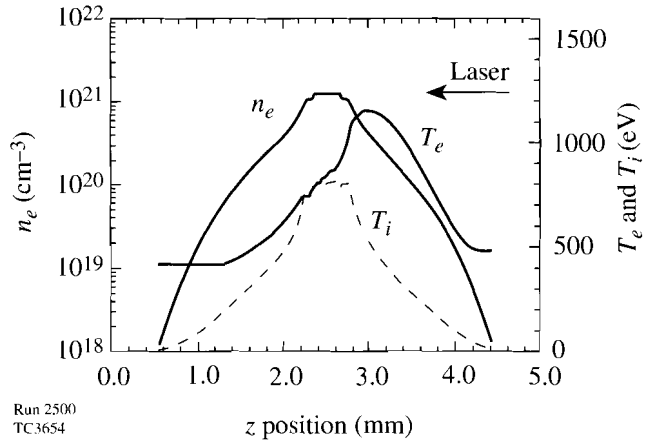

Figure 61.7
Calculated spatial profiles of the electron density n_e and the electron and ion temperatures (T_e, T_i) at 2.2 ns. The pump laser enters from the right.

Owing to the three-dimensional nature of the experiment, some approximations were necessary. The pump beam was modeled as incident along the target normal (z), for consistency with the cylindrical symmetry about this direction assumed by *SAGE*, although the actual angle of incidence was 69°. At 2.2 ns the 0.86 n_c contour, at which the measured epw ($k_{epw} = 2.9 \times 10^5$ cm^{-1}) is resonantly excited, is close to a prolate ellipsoid with diameters 560 μm along and 162 μm transverse to the z axis. Typical rays are incident at 21° to the ellipsoid normal and see flow velocities v_f of 1 to 2 $\times$ 10^7 cm/s generally directed away from the plasma center. The experimental geometry is such that $v_f \cdot k_{epw} \approx 0$.

We verified that the measured signals were caused by CTS from the IADI-excited epw as follows: (1) the $4\omega_0$ intensity decreased rapidly as the pump laser intensity decreased, and the signal disappeared when the pump was below the IADI threshold (as determined by conventional second-harmonic emission measurements); (2) when the probe beam was turned off, no $4\omega_0$ signal was observed; and (3) the $4\omega_0$ intensity varied drastically (decreased about ten times) when the probe beam polarization was changed from out-of-plane to in-plane. Moreover, the measurements discussed in the remainder of this article are all consistent with standard instability theory for a uniform plasma.[1]

The experimental threshold value of the spatially averaged intensity in the instability region was estimated to be ~(1.4–2.8) $\times$ 10^{12} W/cm^2, based on the measured threshold laser energy for a CTS signal (5 J) and taking into account the collisional attenuation and refraction as estimated by *SAGE*. This result is in satisfactory agreement with the theoretical value[9] of ~(0.8–2.3) $\times$ 10^{12} W/cm^2 calculated using T_e = 0.8 keV (appropriate for a low pump intensity), taking into account the swelling at the instability region and the multiple-species ion sound theory of Ref. 10.

Figure 61.8(a) shows a CTS measurement of the time evolution of the epw spectral density function with k_{epw} = 2.9×10^5 cm^{-1}. A clear red shift relative to the $4\omega_0$ wavelength is evident. This Stokes peak is due to the primary IADI decay process: in these experiments, where the pump laser energy is less than 50 J, no cascade decay process[11] is observed. The solid curve in Fig. 61.8(b) shows the spectral density function at the time of the peak signal of Fig. 61.8(a) plotted against the normalized frequency shift $(\omega_0 - \omega_{epw})/\Omega_{iaw}$, where Ω_{iaw} is chosen to center the spectrum on a normalized shift of 1. The CTS timing is not known precisely, but Fig. 61.8(b) is presumed to correspond to 2.2 ns, the peak of the pump beam. The dashed curve gives the IADI growth rate calculated using the experimental parameters; its peak is calculated to occur at $\omega_0 - \omega_{epw} = \Omega_{iaw}$. The IADI resonance condition is thus satisfied, and the normal mode of the iaw is excited. The measured CTS spectrum is consistent with the growth-rate curve. If the pump laser intensity were instead much larger than ten times the threshold, the growth rate peak would shift to a higher frequency and the iaw frequency would increase with the laser intensity (driven mode).

We can now estimate the phase velocity of the iaw. Since the dipole approximation is valid in these experiments, the pump laser wave number is given by $k_0 \sim k_{epw} + k_{iaw} \sim 0$, so that the wave numbers k_{iaw} and k_{epw} are approximately equal in magnitude. The ion-acoustic wave frequency used for the normalization of Fig. 61.8(b) is given by

$$\Omega_{iaw} = 2\pi c \Delta\lambda / \lambda_{4\omega}^2 \approx 9 \times 10^{12}\ \text{Hz},$$

where $\Delta\lambda$ is the wavelength shift of the peak of the CTS signal (3.3±0.2 Å). The phase velocity Ω_{iaw}/k_{iaw} of the iaw is then determined to be about 3×10^7 cm/s and may now be used to estimate the electron temperature.

The electron temperature depends on the ion-acoustic dispersion relation. To calculate this with greater accuracy, the multiple-ion nature of the plasma was included. Williams *et al.*[10] have obtained fast- and slow-wave solutions for CH plasmas and have shown that the slow wave is the important one, as it is eight times less damped than the fast wave. The phase velocity of the slow wave is effectively independent of

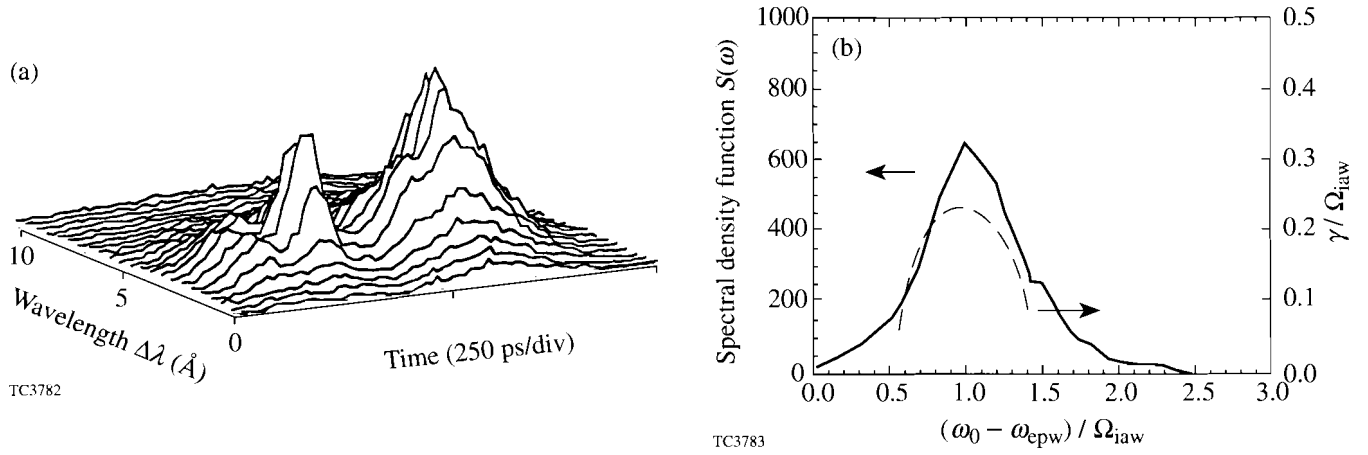

Figure 61.8
(a) Time evolution of the spectral density function of the epw (with $k_{epw} = 2.9 \times 10^5$ cm^{-1}) measured by CTS. (b) Solid line: the spectral density function of the same epw at $t \approx 2.2$ ns. Dashed line: the IADI growth rate calculated for a laser intensity five times threshold.

T_i in the range $0.3 < T_i/T_e < 1$, being about 0.8 $(k_B T_e/M)^{1/2}$ or $1.87 \times 10^{-2}\, v_e$, where M is the proton mass, k_B is Boltzmann's constant, and v_e is the electron thermal velocity. The slow iaw frequency at a given wave number is thus an excellent diagnostic for T_e: from the measured peak-signal frequency shift and the scattering wave vector (known from the geometry), one immediately obtains the slow iaw velocity and hence T_e. In this experiment, the iaw phase velocity is 3×10^7 cm/s, giving $T_e = 1.5$ keV and $v_e = 1.6 \times 10^9$ cm/s. The theoretical values ($v_e = 1.4 \times 10^9$ cm/s and $T_e = 1.1$ keV) given by the *SAGE* calculation (Fig. 61.7) are somewhat lower than the experimental values (about 13% for v_e and 27% for T_e). However, if the complicated nature of the large-scale plasma produced, the possibility of hot spots within the focal spot, and the three-dimensional nature of the experiment are all taken into account, the theoretical and experimental values are in reasonably good agreement.

Several conditions were met that enabled the diagnostic to work well:

- The scattering angle was chosen to be large to measure the most unstable epw.
- Between the thresholds for the slow-ion-wave IADI (I_{th}) and the fast-ion-wave IADI (8 I_{th}), only the former was significantly excited.
- The refraction of the probe beam itself was small (less than 7% for this experiment) and that of the up-shifted signal even smaller.
- The complications of plasma flow effects on the diagnostic were minimized because the detection vector ($k_{epw} = k_s - k_i$) was perpendicular to the direction of plasma expansion.
- Because this is a collective scattering, the scattering rate is much larger than that from thermal electrons, and it is relatively easy to exceed the background bremsstrahlung emissions.
- The experimental design assured that only a narrow range of densities could contribute to the observed signals.[12]

We also measured the conventional second-harmonic signal (from the coupling between two epw's) and found its threshold laser energy to be comparable to that of the CTS threshold energy, consistent with the presence of the IADI. The Stokes signal is spread over a large wavelength range and decreases gradually without a distinct peak. This finding indicates that the epw intensity is spread over a wide range of wave numbers in the large-scale plasma.

In summary, we have studied the ion-acoustic decay instability in a large-scale-length (~1-mm), hot (~1-keV) plasma, which is relevant to a laser fusion reactor target, and have shown that the IADI threshold is low. We have also developed a novel collective Thomson scattering diagnostic for the interaction of a 1-μm pump laser near its critical density, using the third harmonic of the interaction laser at a 90° scattering angle, and we have used this diagnostic to measure the electron plasma wave excited by the ion-acoustic decay insta-

bility near the critical density ($n_e \sim 0.86\, n_c$). The frequency of the detected wave obtained from this diagnostic has been used to determine the electron temperature in the interaction region, yielding a result reasonably close to that predicted by the *SAGE* computer code.

ACKNOWLEDGMENT

This work was carried out in collaboration with K. Mizuno, B. S. Bauer, J. S. DeGroot, R. P. Drake, and B. Sleaford of the Plasma Physics Research Institute at the Lawrence Livermore National Laboratory and the University of California at Davis. We thank T. W. Johnston and E. A. Williams for many useful discussions, and W. L. Kruer and E. M. Campbell for their help and encouragement. This work was supported by the U.S. Department of Energy National Laser Users Facility at the University of Rochester, the U.S. Department of Energy Office of Inertial Confinement Fusion under Cooperative Agreement No. DE-FC03-92SF19460, and the U.S. Department of Energy under contract W-7405-ENG-48 with the Lawrence Livermore National Laboratory.

REFERENCES

1. W. L. Kruer, *The Physics of Laser Plasma Interactions*, Frontiers in Physics, Vol. 73 (Addison-Wesley, Redwood City, CA, 1988); K. Nishikawa, J. Phys. Soc. Jpn. **24**, 916 (1968); **24**, 1152 (1968).

2. C. Yamanaka *et al.*, Phys. Rev. Lett. **32**, 1038 (1974); K. Tanaka, W. Seka, L. M. Goldman, M. C. Richardson, R. W. Short, J. M. Soures, and E. A. Williams, Phys. Fluids **27**, 2187 (1984).

3. K. Mizuno, P. E. Young, W. Seka, R. Bahr, J. S. De Groot, R. P. Drake, and K. G. Estabrook, Phys. Rev. Lett. **65**, 428 (1990); K. Mizuno, R. P. Drake, P. E. Young, R. Bahr, W. Seka, and K. G. Estabrook, Phys. Fluids B **3**, 1983 (1991).

4. K. Mizuno *et al.*, Phys. Rev. Lett. **52**, 271 (1984); K. Mizuno, F. Kehl, and J. S. DeGroot, Phys. Rev. Lett. **56**, 2184 (1986).

5. D. F. DuBois, H. A. Rose, and D. Russell, Phys. Rev. Lett. **66**, 1970 (1991).

6. W. Seka, R. S. Craxton, R. E. Bahr, D. L. Brown, D. K. Bradley, P. A. Jaanimagi, B. Yaakobi, and R. Epstein, Phys. Fluids B **4**, 432 (1992).

7. J. Sheffield, *Plasma Scattering of Electromagnetic Radiation* (Academic Press, New York, 1975).

8. R. S. Craxton and R. L. McCrory, J. Appl. Phys. **56**, 108 (1984).

9. There is some uncertainty in this estimate, principally because the local electric field, which determines the IADI threshold, depends on the angle between the pump laser and the plasma density gradient at the instability region, due to the angular dependence of the swelling.

10. E. A. Williams *et al.*, submitted to Physics of Plasmas.

11. The cascade process for a fixed k_{epw} is that $\omega_{epw}^{(n)} = \omega_{epw}^{(n+1)} + \omega_{iaw}^{(n+1)}$, and $k_{epw}^{(n)} = k_{epw}^{(n+1)} + k_{iaw}^{(n+1)}$ (which indicates that

$$\left|k_{epw}^{(n)}\right| = \left|k_{epw}^{(n+1)}\right| = 1/2\left|k_{iaw}^{(n+1)}\right| ,$$

where $n = 1, 2 \ldots$, and $n = 1$ is the epw excited by the primary IADI process).

12. The epw's excited at densities above $0.86\, n_c$ have smaller wave numbers and cannot produce the observed wave vector by propagation. The epw's driven at densities much below $0.86\, n_c$ are very strongly Landau damped.

Frequency-Domain Interferometer for Measurement of the Group-Velocity Walkaway of Ultrashort Pulses in Birefringent Media

A new technique based on frequency-domain interferometry (FDI)[1,2] has been used to measure the group-velocity walkaway (GVW) of ultrashort pulses in birefringent media. As the name implies, this technique is based on the spectral interference of two short pulses in the frequency domain and makes use of the intrinsic phase delay between the fast and slow modes of a birefringent medium. Due to the different group delays, two pulses launched along the fast and slow axes will come out of the medium at different times. In the frequency domain, two temporally separated pulses interfere in the same way that two waves with different frequencies do in the time domain. In the frequency-domain interferometer described here, measurement of the modulation period of the interference fringes in the frequency domain gives the GVW directly without the need for further assumptions about the properties of the light source. By analogy with an ordinary interferometer, the two optical axes of the birefringent medium can be regarded as two interfering arms. A polarizer placed at the output end of the medium combines the two field components to generate interference fringes in the frequency domain. Temporally separated pulses can interfere owing to the linear dispersion of the grating in a spectrometer.[1,2] Different frequency components propagate along different directions, resulting in a frequency-dependent time delay. Therefore, two temporally separated pulses can physically overlap on the detector surface of the spectrometer. In comparison with other methods, the experimental setup of our interferometer is quite simple, and the alignment is very easy. Of greater significance is the fact that the experimental data is directly related to the GVW and no further curve fitting is needed.

To understand the physics of the frequency-domain interferometer, we must understand the properties of a spectrometer. A simplified version of a spectrometer is shown in Fig. 61.9. The incident beam is collimated and has a diameter D. The incident angle to the grating is i, while the diffracted angle is α. Assuming two pulses with pulse width τ_p that are separated by T, we find that the amplitude fronts of these two pulses are no longer parallel to the phase fronts after the grating. At the focus of the image lens, each pulse is temporally stretched to a duration of $DN\lambda/\cos(i)c$, where N is the groove number of the grating, λ is the wavelength of the pulses, and c is the speed of light. The two separate pulses can physically overlap for a time t_0 in at the focal (frequency) plane, provided that the original separation T is less than the grating-induced stretching $DN\lambda/\cos(i)c$ shown in Fig. 61.9.

FDI for the Measurement of Polarization Mode Dispersion of Single-Mode Optical Fibers

Single-mode optical fibers have seen increasing use in coherent optical transmission systems and as polarization-dependent fiber-optic sensors. A knowledge of the polarization properties of single-mode fibers is of fundamental importance in these applications since these properties govern the degree and state of the polarization of the radiation. It is well-known that birefringence in optical fibers can be induced by

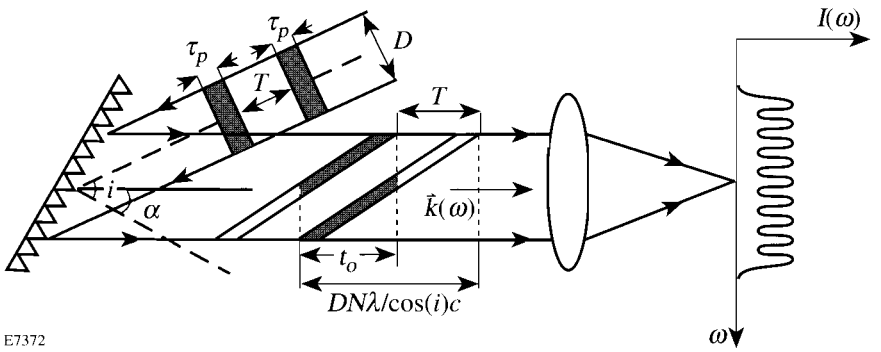

Figure 61.9
A simplified diagram illustrating temporal stretching of short pulses in a spectrometer. The incident angle to the grating is i; the diffracted angle is α.

built-in stress or by geometric deformation of the fiber core. The most important parameters characterizing birefringent fibers are the polarization mode dispersion (PMD) and modal birefringence (MB). Polarization mode dispersion is the group delay time difference between two orthogonally polarized HE_{11} modes, while modal birefringence is the refractive index difference between these two modes. In optical fiber communication systems, the presence of PMD results in bandwidth limitations.[3] Polarization mode dispersion has two contributions: one is the phase delay, which is proportional to modal birefringence; the other arises from dispersion difference between two modes. Since the first experimental verifications of PMD in birefringent optical fibers made by Rashleigh and Ulrich,[4] many methods for measuring PMD in single-mode fibers have been reported.[4–18] These methods fall into four categories: optical short-pulse methods,[7] frequency domain techniques,[8,9] interferometric methods,[4,8–16] and optical heterodyne techniques.[17–18] The white-light interferometric method has proved to be very accurate and applicable to meter-length samples.[4,16]

The configuration of the frequency-domain interferometer as used in our experiment is shown schematically in Fig. 61.10. The birefringent axes are labeled as x and y; the laser light propagates along the z direction. Two identical pulses temporally displaced by T are launched into the birefringent fiber with their polarization directions aligned to the x and y axes, respectively. At the input plane ($z = 0$), the electric fields of these two pulses can be expressed by

$$\begin{aligned} E_x(t, z=0) &= E(t)\exp(i\,\omega_0\,t) \\ E_y(t, z=0) &= E(t-T)\exp[i\,\omega_0(t-T)], \end{aligned} \tag{1}$$

where $E(t)$ is the slowly varying envelope of the two pulses and ω_0 is the carrier frequency of the laser pulses. At the exit end of the fiber, the Fourier transformations of the electric fields are

$$\begin{aligned} E_x(\omega, z=L) &= E(\omega-\omega_0)\exp[-i\,\beta_x(\omega)\,L] \\ E_y(\omega, z=L) &= E(\omega-\omega_0)\exp[-i\,\beta_y(\omega)\,L] \\ &\quad \times \exp(-i\,\omega\,T), \end{aligned} \tag{2}$$

where $E(\omega-\omega_0)$ is the Fourier transform of $E(t)$ and $\beta_x(\omega)$ and $\beta_y(\omega)$ are propagation constants of the x and y modes.

A polarizer with its transmission axis set to 45° with respect to the x and y axes combines the two electric fields:

$$E_{\text{out}}(\omega, z=L) = \frac{1}{2}\left[E_x(\omega, z=L) + E_y(\omega, z=L)\right]. \tag{3}$$

The power spectrum detected by a spectrometer can be expressed as

$$I(\omega) = \frac{1}{4}\left|E(\omega-\omega_0)\right|^2\left\{1+\cos[\Delta\beta(\omega)L+\omega T]\right\}, \tag{4}$$

where $\Delta\beta(\omega) = \beta_x(\omega) - \beta_y(\omega)$ is the modal birefringence and can be expanded as follows:

$$\begin{aligned} \Delta\beta(\omega) &= \Delta\beta(\omega_0) + \frac{d\Delta\beta(\omega_0)}{d\omega}\Delta\omega \\ &\quad + \frac{1}{2}\frac{d^2\Delta\beta(\omega_0)}{d\omega^2}\Delta\omega^2 + \ldots, \end{aligned} \tag{5}$$

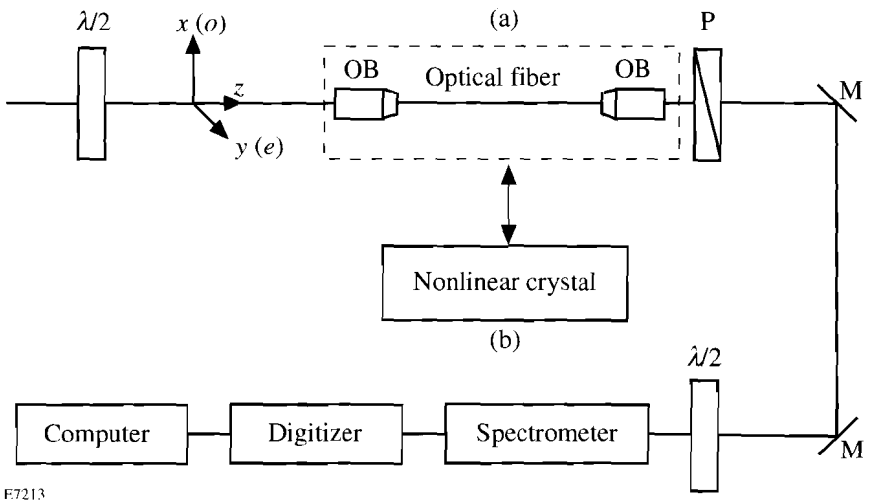

E7213

Figure 61.10
Experimental setup for measurement of GVW in birefringent media, where λ/2 = half-wave plate, OB = microscope objectives, P = polarizer, and M = mirror. Linearly polarized light is coupled into the birefringent sample with the polarization direction aligned 45° with respect to the optic axes. The microscope objectives and birefringent fiber (a) were replaced with CDA, KDP, or KD*P (b) for measurements of GVW in nonlinear crystalline media.

where $d\Delta\beta/d\omega$ is the polarization mode dispersion. The third term in Eq. (5) is the difference of group-velocity dispersion (GVD), which describes the difference in pulse spreading for the two principal axes. For subpicosecond pulses, the dispersion distance (the distance at which pulse width becomes twice the initial value) could be shorter than 1 m.[19] This term can be ignored, as pointed out in Ref. 4, since the difference in temporal spreading due to GVD is still negligible. Substituting Eq. (5) into Eq. (4) gives

$$I(\omega) = \frac{1}{4}\left|E(\omega-\omega_0)\right|^2 \times \left\{1+\cos\left[\Delta\beta(\omega_0)L+\frac{d\Delta\beta}{d\omega}\Delta\omega L+\omega T\right]\right\}. \quad (6)$$

From Eq. (6), the periodicity of the interference fringes is given by

$$\Omega = 2\pi\Big/\left(\frac{d\Delta\beta}{d\omega}L+T\right). \quad (7)$$

The polarization mode dispersion can be determined in terms of the measured quantity Ω, the fringe spacing in the frequency domain. From Eq. (7), we have

$$\frac{d\Delta\beta}{d\omega} = \left(\frac{2\pi}{\Omega}-T\right)\Big/L. \quad (8)$$

A careful examination of Eq. (8) reveals that there are two possible methods of measuring PMD. In the first method, no optical delay is needed ($T=0$), and a measurement of the fiber length L and interference spacing Ω gives the required result of PMD. This method has the advantage in that it is very simple to implement. The second method relies on adjustment of the temporal delay such that $\Omega=\infty$, which makes PMD $= -T/L$. Physically, this means that the predelay T is set so that two pulses come out of the fiber at the same time, resulting in no interference in the frequency domain.

The experimental setup is shown in Fig. 61.10. The laser beam originates from an actively mode-locked Nd:YLF oscillator that produces a 50-ps pulse train at a 1054-nm wavelength with a 100-MHz repetition rate. The pulse train goes through an 800-m, single-mode optical fiber that increases the bandwidth from 0.3 Å to 31.6 Å through the combined effects of self-phase-modulation (SPM) and GVD.[20] The pulses are then temporally compressed to 1 ps by a double-pass grating pair. Two microscope objectives are used to couple the laser beam into and out of a highly birefringent fiber (3M product, FS-HB-5651). A $\lambda/2$-wave plate placed in front of the fiber was used to control the polarization direction of the incident laser beam. A polarizer placed at the exit end of fiber was used to combine the electric field components of the fast and slow modes. Finally the collimated output beam was sent to a spectrometer equipped with an optical multichannel analyzer (OMA). Another $\lambda/2$-wave plate placed in front of the spectrometer was used to match the polarization direction of the laser beam to that of the grating inside the spectrometer. The waveguide parameters of the fiber used in the experiment are listed in Table 61.I.

Table 61.I: Waveguide parameters of the fiber used in the experiment.

Fiber length	2.750 m
Mode field diameter	6.8 μm
Fiber diameter	100 μm
Operating wavelength	1.060 μm
Cutoff wavelength	1.000 μm
Birefringence	4×10^{-4}
Loss	<2 dB/km

The input spectrum $\left[\left|E(\omega-\omega_0)\right|^2\right]$ is shown in Fig. 61.11. The power spectrum has nearly a square-top shape with a width of about 31.6 Å. In the experiment, the input polarization

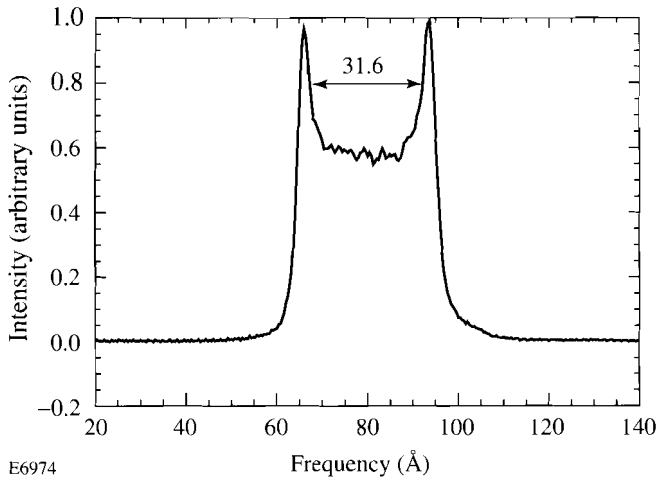

Figure 61.11
The spectrum of the incident pulses applied to the fiber. The spectrum shape is typical of the combined effects of SPM and GVD. The peak-peak width is 31.6 Å.

direction was adjusted to 45° with respect to the fast and slow axes of the birefringent fiber. The polarizer was also aligned to the same angle as described in Eq. (3). The frequency-domain interference fringes are shown in Fig. 61.12. The least-squares method was used to fit Fig. 61.12 using Eq. (6). The value of Ω was found to be 22.7±0.1 pixels, giving a modulational period of the interference fringes of 9.13±0.04 Å. The length of the fiber was measured to an accuracy of 1 mm. From Eq. (8), the PMD is found to be 1.42 ps/m with an accuracy of 1%. The term $d\Delta\beta/d\omega$ of Eq. (8) can also be expressed as

$$\frac{d\Delta\beta}{d\omega} = \frac{\Delta n}{c} + \frac{\omega}{c}\frac{d\Delta n}{d\omega}, \tag{9}$$

where Δn is the modal birefringence and c is the speed of light. Substituting the value for $\Delta\Omega$ from Table 61.I into Eq. (9) makes the first term on the right-hand side of Eq. (9) equal to 1.3±0.1 ps/m, which is very close to the measured PMD. The uncertainty comes from the fact that there is not enough information about the sample fiber. The contribution of the second term in Eq. (9) is much smaller than the first term, which is true in most stress-induced birefringent fibers.[20,21]

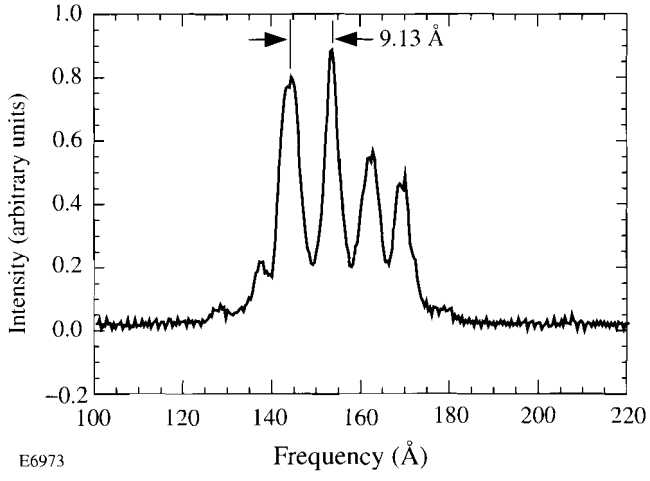

Figure 61.12
Frequency-domain interference fringes for the birefringent fiber. The fringe spacing is measured to be 9.13 Å.

FDI for the Measurement of GVW in Nonlinear Crystals

Frequency conversion in nonlinear crystals is an important method for obtaining coherent radiation sources for wavelengths not covered by lasers and is especially valuable in applications involving ultrashort laser pulses. Frequency conversion includes second (and higher) harmonic generation,[22–24] optical parametric oscillators (OPO), and optical parametric amplifiers (OPA).[25,26] A major limitation in ultrashort frequency conversion is the GVW between the ordinary (o-wave) and extraordinary (e-wave) waves due to the different group velocities for the two polarizations.[27] Since birefringence and dispersion exist in all nonlinear crystals, the GVW effect becomes a fundamental factor in determining the frequency-conversion efficiency. The walkaway has been used to increase the conversion efficiency in type-II doubling of 1-μm, 1-ps laser pulses by using a second crystal to predelay the extraordinary wave relative to the ordinary wave.[22,23] It was also found that the pulse duration could be reduced from 1 ps to 200 fs.[28] Chien *et al.*[24] have studied the conversion efficiency of high-power ultrashort pulses and have found that the GVW between two polarizations causes reconversion of the second harmonic back to the fundamental frequency.

The GVW between the e- and o-wave is of fundamental importance in the frequency conversion of ultrashort pulses. Typically, the walkaway is inferred by measuring the refractive indices and the dispersion of the e- and o-waves. Most values of the refractive index have been obtained by the minimum-deviation method (MDM) and are accurate to the fifth decimal place.[29] Extensive measurements of refractive indices of nonlinear crystals isomorphic to KH_2PO_4 have been made by Kirby and DeShazer.[30] Although MDM provides an accurate measurement of the refractive indices of e- and o-waves, it is not convenient for many applications involving nonlinear frequency conversion. Since the MDM measurement requires a high-quality prism made from the sample crystal, this method can be expensive and impractical for ordinary frequency-conversion applications. The dispersion properties are usually obtained by fitting to the Sellmeier or Zernike formula,[31,32] which requires multiple measurements with different light frequencies. Since narrow spectral lines of different lamps are used in MDM, it is possible that no experimental data exists for some specific wavelength that is used in frequency-conversion experiments. Another disadvantage of this method is that the refractive indices of o- and e-waves are a function of propagation direction. All calculations require that the locations of optical axes and the propagation angle, as well as the relative angle between the propagation direction and the optical axis, be known accurately.

In this section we report on an alternative method that allows direct measurement of the GVW between the e- and o-waves in a birefringent crystal. There are several other advantages of this technique as far as nonlinear frequency conversion is concerned. In practical applications of frequency

conversion involving short pulses, it is desirable to know the walkaway parameter for the laser frequency involved. Since the walkaway can be measured using the same laser pulses that will be used in frequency conversion, the measured data about the walkaway is immediately relevant. For the applications involving cascade processes of frequency conversion of short pulses, it is crucial to know either the polarization direction or the crystal orientation that corresponds to the minimum walkaway, so that the orientations of nonlinear crystal for the next stage of frequency conversion can be optimized.[28] To our knowledge, this method provides the first direct measurement of angular dependence of the GVW.

From Eq. (4), the power spectrum detected in the spectrometer takes the following form:

$$I(\omega) = \frac{1}{4}\left|E(\omega-\omega_0)\right|^2\left[1+\cos(\phi_0+\Delta\tau\Delta\omega)\right], \qquad (10)$$

where $E(\omega-\omega_0)$ is the spectrum of the incident pulse, ϕ_0 is a constant, $\Delta\tau$ is the temporal delay between the two pulses traveling along the fast and slow axes of the crystal, and $\Delta\omega = \omega - \omega_0$. The GVW is therefore equivalent to the periodicity of the interference pattern in the frequency domain.

The experimental setup is as shown in Fig. 61.10, except that the birefringent fiber and microscope objectives used for in-and-out coupling the incident light are replaced by a nonlinear crystal. The frequency-domain interference fringes for a 2.5-cm-thick CDA crystal are shown in Fig. 61.13. A least-squares method is used to fit Fig. 61.13 using Eq. (10), as shown by the dashed curve. There are three sources of error in the measurements: (1) measuring the length of the crystal, (2) calibrating the spectrometer, and (3) determining the spacing of the interference fringes. The error bar for thickness measurement is 1%. The calibration was performed using five spectral lines of a rubidium lamp ranging from 1053 nm to 1073 nm. The spectral lines were fitted with a Lorentzian line shape, and the overall error bar in the calibration was found to be 0.2%. The least-squares fit for the interference fringes gave an error of 0.3%. The largest source of error is in the measurement of the crystals' thickness. After taking into account these three error sources, we found that the error in determining the temporal walkaway is about 1%. The experimentally determined GVW values for several commonly used nonlinear crystals are listed in Table 61.II, along with the cut angles and lengths of the tested crystals. The last column of Table 61.II shows the calculated values of the GVW based on the dispersion data of Ref. 30; the measured results are very close to the calculated ones. As mentioned previously, this method can also be used to measure the length of a birefringent crystal if its GVW parameter is known. The last row of Table 61.II shows the length of a KDP-I crystal determined by this method using the calculated result of the walkaway; the resolution is about 50 μm.

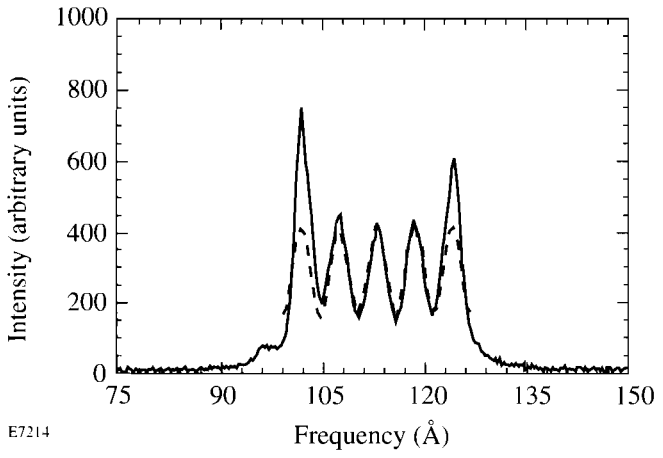

Figure 61.13
Frequency-domain interference fringes of the CDA-I sample. The fringe spacing is measured to be 6.7 Å. The solid line is the experimental data, while the dashed line is the theoretical fitting.

Table 61.II: Parameters of nonlinear crystals and measured walkaway.

Crystal	Cut angle	Length ×2 (cm)	Walkaway [(a)] (ps/cm)	Walkaway [(b)] (ps/cm)
CDA I	85.0°	2.50	1.00±0.01	1.01
KDP* II	53.7°	1.50	0.94±0.02	0.97
KDP II	59.2°	1.90	1.35±0.02	1.33
KDP I	41.2°	1.029±0.005	–	0.79

(a) Measured results
(b) Calculated results

Since the refractive index of the extraordinary wave is a function of propagation direction, the GVW will also be affected by the direction of propagation, as shown by the plot of walkaway dependence versus propagation angle in Fig. 61.14. The angle is measured with respect to the phase-matching angle of the crystal (KDP-II) in the YZ plane. The scattered triangles are experimental data, while the solid curve is the theoretical prediction based on the material dispersion.[24] The experimental data fits the theory very well, with an accuracy of 1%. The angle shown in Fig. 61.14 is the angle inside the crystal as obtained by Snell's law. The propagation

distance is also a function of angle due to the cube-shaped crystal, which has been taken into account in Fig. 61.14. In our experiment, the pulses were not transform limited (i.e., the pulses are slightly chirped). It is believed that the chirp may be responsible for the finite visibility of the interference patterns, which could affect the accuracy of the measurements when visibility is poor.

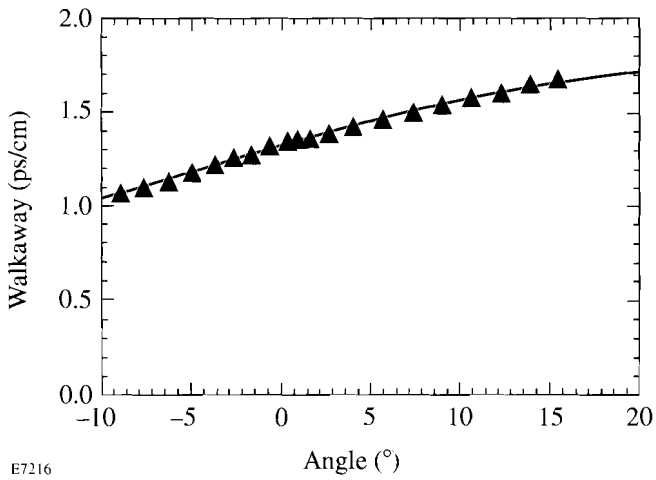

Figure 61.14
Dependence of the group-velocity walkaway on the propagation direction. The angle is measured with respect to the phase-matching angle of the sample (KDP-II).

Conclusions

A new technique based on frequency-domain interferometry has been used to measure the polarization mode dispersion of birefringent media. In contrast to the usual interferometric methods that measure the interference visibility as a function of optical delay between two interfering arms, we measure the periodicity of the interference fringes in the frequency domain by using short, broadband optical pulses. No curve fitting is needed to find the values of PMD since the measured modulation period of the fringes is directly related to PMD. Two schemes of measurement, differing only in the requirements for an optical delay line, have been presented, and one method (without the delay line) was demonstrated experimentally. Advantages of this new method include (1) direct, real-time measurement of the group-velocity walkaway, which is useful for applications in which the GVW can be controlled by tuning the crystals; (2) values of GVW at the appropriate wavelength for most frequency-conversion applications since the source is the same as that used in the nonlinear frequency conversion; and (3) determination of the angular dependence of GVW, which is useful for experiments involving serial frequency conversion in that the walkaway can be compensated for in the second crystal.[28] Compared to other methods, the frequency-domain interferometric technique provides reasonably good accuracy, experimental simplicity, and linearity in the sense that it is not dependent on the laser power.

ACKNOWLEDGMENTS

This work was supported by the U.S. Department of Energy, Office of Inertial Confinement Fusion under Cooperative Agreement No. DE-FC03-92SF19460, the University of Rochester, and the New York State Energy Research and Development Authority. The support of DOE does not constitute an endorsement by DOE of the views expressed in this article.

REFERENCES

1. N. F. Scherer *et al.*, J. Chem. Phys. **95**, 1487 (1991).
2. E. Tokunaga, A. Terasaki, and T. Kobayashi, Opt. Lett. **17**, 1131 (1992).
3. I. P. Kaminow, IEEE J. Quantum Electron. **QE-17**, 15 (1981).
4. S. C. Rashleigh and R. Ulrich, Opt. Lett. **3**, 60 (1978).
5. Y. Sasaki, N. Shibata, and J. Noda, Electron. Lett. **18**, 997 (1982).
6. M. Monerie, P. Lamouler, and L. Jeunhomme, Electron. Lett. **16**, 907 (1980).
7. Y. Yamabayashi and M. Saruwatari, Electron. Lett. **19**, 239 (1983).
8. K. Mochizuki, Y. Namihira, and H. Wakabayashi, Electron. Lett. **17**, 153 (1981).
9. N. Shibata, M. Tateda, and S. Seikai, IEEE J. Quantum Electron. **QE-18**, 53 (1982).
10. N. Imoto and M. Ikeda, IEEE J. Quantum Electron. **QE-17**, 542 (1981).
11. S. C. Rashleigh, Opt. Lett. **7**, 294 (1982).
12. S. C. Rashleigh, *ibid.* **8**, 336 (1983).
13. A. B. Grudinin, G. L. Dyankov, and V. B. Neustruev, Sov. J. Quantum Electron. **16**, 1522 (1986).
14. L. Thévenaz, V. de Coulon, and J.-P. Von der Weid, Opt. Lett. **12**, 619 (1987).
15. J.-P. Von der Weid, L. Thévenaz, and J.-P. Pellaux, Electron. Lett. **23**, 151 (1987).
16. W. J. Bock and W. Urbanczyk, Appl. Opt. **32**, 5841 (1993).
17. N. Shibata, M. Tsubokawa, and S. Seikai, Electron. Lett. **20**, 1055(1984).
18. N. Shibata, M. Tsubokawa, and S. Seikai, Opt. Lett. **10**, 92 (1985).
19. G. P. Agrawal, *Nonlinear Fiber Optics* (Academic, Boston, 1989), Chaps. 3–5.
20. N. K. Sinha, Phys. Chem. Glasses **18**, 66 (1978).

21. N. Shibata *et al.*, J. Opt. Soc. Am. **73**, 1972 (1983).

22. Y. Wang and R. Dragila, Phys. Rev. A **41**, 5645 (1990).

23. Y. Wang, B. Luther-Davis, Y.-H. Chuang, R. S. Craxton, and D. D. Meyerhofer, Opt. Lett. **16**, 1862 (1991).

24. C. Y. Chien, G. Korn, J. S. Coe, J. Squier, G. Mourou, and R. S. Craxton, submitted to Optics Letters.

25. R. L. Byer, J. Opt. Soc. Am. B **10**, 1656 (1993).

26. R. L. Byer, *ibid.* **10**, 2148 (1993).

27. R. W. Boyd, *Nonlinear Optics* (Academic Press, San Diego, 1992).

28. Y. Wang and B. Luther-Davies, Opt. Lett. **17**, 1459 (1992).

29. W. L. Wolfe, "Properties of Optical Materials," in *Handbook of Optics*, edited by W. G. Driscoll (McGraw-Hill, 1978), Sec. 7, pp. 7-1–7-157.

30. K. W. Kirby and L. G. DeShazer, J. Opt. Soc. Am. B **4**, 1072 (1987).

31. M. Born and E. Wolf, *Principles of Optics*, 6th ed. (Pergamon, Oxford, 1986).

32. F. Nernike, Jr., J. Opt. Soc. Am. **54**, 1215 (1964).

Transient Flux Dynamics in Optically Irradiated YBCO Thin-Film Switches

Fast switching using thin films of high-temperature superconductor (HTS) has been a subject of interest in recent years. Several high-power applications, including fault current limiters, generation of fast current pulses, and energy extraction from superconducting magnetic energy storage (SMES), require an opening switch with high current-carrying capacity and fast rise times. The property requirements of the opening switch are diverse and depend on the application.[1] In this article, we discuss a contactless, inductively coupled opening switch that employs $YBa_2Cu_3O_{7-x}$ (YBCO) thin films.

In its simplest form, the switch consists of a film of HTS placed between the primary and secondary coils of a transformer, shown conceptually in Fig. 61.15.[2] A current source drives current in the primary coil. If the film is superconducting, it screens the magnetic flux, and there is no flux coupling between the two coils. If a load is connected across the secondary coil, the voltage across the load is zero. Upon illumination by a laser pulse, the film makes a transition to the normal state, allowing magnetic flux produced by the primary current to couple into the secondary coil. The temporal change of flux through the secondary coil results in an induced voltage $\left(V = -\partial\Phi/\partial t\right)$ across the load. A similar contactless arrangement has been used to measure critical temperature and critical current density of films.[3] Optically thick films (500–800 nm) were used in our experiment to enhance the current-carrying capacity. A ring of 5-mm width, 1-mm thickness, and 20-MA/cm^2 current density will correspond to a current of 1 kA that can produce a field $\left(B = \mu_0\, I/2a\right)$ of about 0.12 T at the center of the ring. This order-of-magnitude estimate suggests that a large field can be excluded using thin films with very high critical current density (J_c).

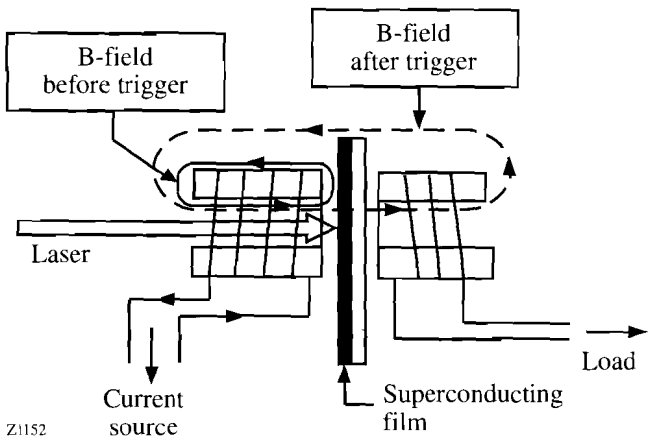

Figure 61.15
A conceptual diagram of the high-temperature superconducting thin-film switch. The superconducting film acts as a magnetic shield until triggered.

Figure 61.16 shows the configuration of our switching system, which has three components: the source (the primary coil in our discussion), the switch (the superconducting film), and the load circuit (the secondary coil and load). The superconducting magnet serves as the primary coil (source), while two superconducting films (switch) are placed on either side of the secondary coil.

Theory

For the described switch configuration, if the applied field, which is perpendicular to the film surface, is below the lower critical field (H_{c1}) of the superconductor, the superconductor is in a reversible Meissner state and will initially screen the flux produced by the magnet from coupling to the secondary coil. When it is driven to its normal state by heating with a laser pulse, the magnetic flux moves radially inward and produces a voltage pulse across the secondary coil. As the film cools down and returns to its superconducting state, it will expel the flux. Repetitive switching can then be performed with a train of laser pulses.[2] If the applied field exceeds H_{c1}, the flux will still be excluded from the superconductor up to a certain field strength depending upon the critical current density of the film (critical state model). Beyond this point, only a partial flux exclusion will take place as the screening currents in the superconductor redistribute to exclude the flux from the center of the film. Single-shot switching can still be performed under these conditions, allowing the excluded flux to couple to the secondary coil. As the film cools into the superconducting

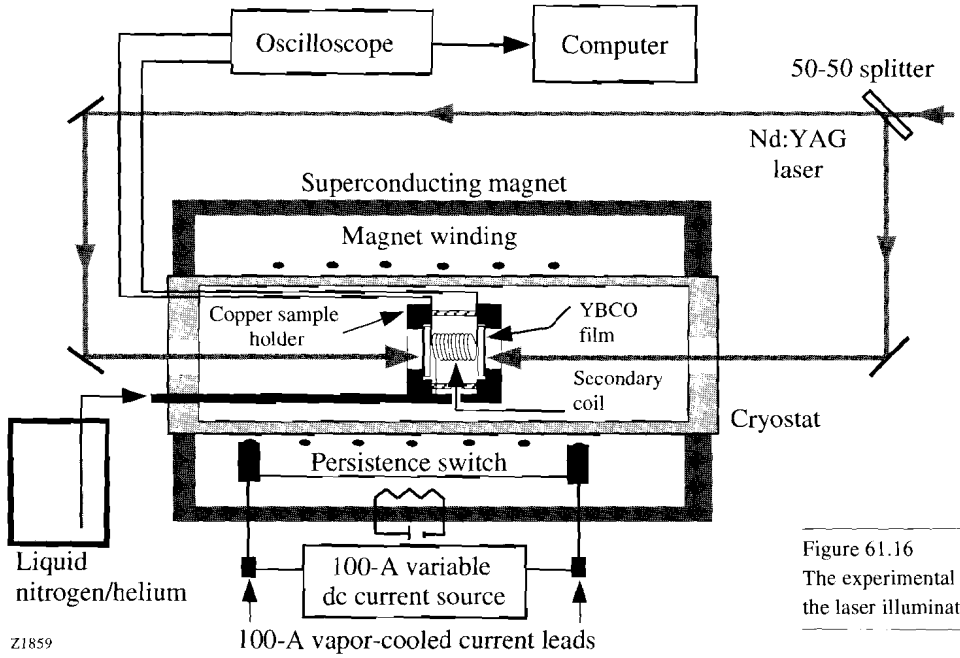

Figure 61.16
The experimental setup for the high-field experiments showing the laser illumination scheme and the data acquisition system.

state, however, it will no longer expel the penetrated flux. Because the thin-film geometry produces a large demagnetization factor that causes enhancement of the magnetic field at the edges of the film, some field penetration occurs at the edges, even when the applied field is less than H_{c1}.

To understand the motion of flux inside the superconductor following its transition into the normal state, we must analyze the distribution of screening currents and magnetic fields. Temporal variation of the flux in the secondary coil, which is inductively coupled to the superconducting films, must also be investigated.[4] We first calculate the current and field distribution in a film of thickness t, shaped like a circular disk of radius R, for a given externally applied field (B_{ext}) and critical current density (J_c) by dividing the disk into a set of n concentric circular strips of equal width ($w = R/n$, where $n = 25$ for our calculation). Starting from the current-density distribution $J(r)$ required for complete flux exclusion inside the film, the J_c-limited distribution is calculated iteratively. At each step of the iteration the field is allowed to penetrate from the edge by the width of one ring more than the previous step. If the field penetrates to a radius a, $J(r < a)$ is recalculated to make the region $0 < r < a$ flux free, and $J(r > a)$ is set equal to J_c. For a single film and field-independent critical current, our result, shown in Fig. 61.17, exactly matches the analytical expression given by Mikheenko and Kuzovlev.[5]

We then proceed to calculate the temporal evolution of current distributions in the two films and the secondary coil. This is done by treating each ring in the two films and the secondary coil as $(2n + 1)$ circuits. We then solve a set of linear equations of the form $[L]d[I]/dt + [R][I] = 0$, where $[L]$ and $[R]$ are matrices of dimension $(2n + 1) \times (2n + 1)$ and $[I]$ is a column vector. The diagonal elements of $[L]$ are the inductances of each circuit, and off-diagonal elements are the appropriate mutual inductances. $[R]$ is a diagonal matrix with elements equal to the normal-state resistances of the circuits. The elements of $[I]$ represent the current in each circuit. Using

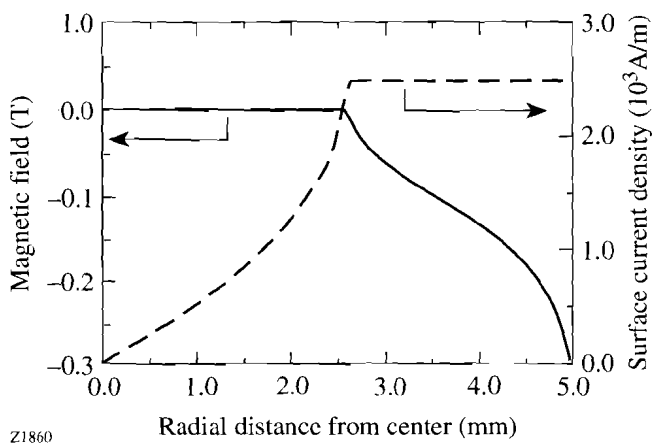

Figure 61.17
Static J_c-limited surface current and z-component of the magnetic field for a 1-cm-diam, thin superconducting disk of 500-nm thickness. A constant critical current density of 5.10^7 A/cm^2 and an externally applied field of −0.2 T are assumed.

this analysis we calculate the current in the secondary coil as a function of time; Fig. 61.18 shows the result of this calculation. The matrix formulation of the problem enables us to take advantage of the computationally efficient, matrix manipulation tools in commercial software packages such as MATLAB™. The numerical method discussed above can easily incorporate additional details,[4] e.g., field-dependent critical current densities $J_c(B)$ and field-dependent superconducting flux-flow resistances.

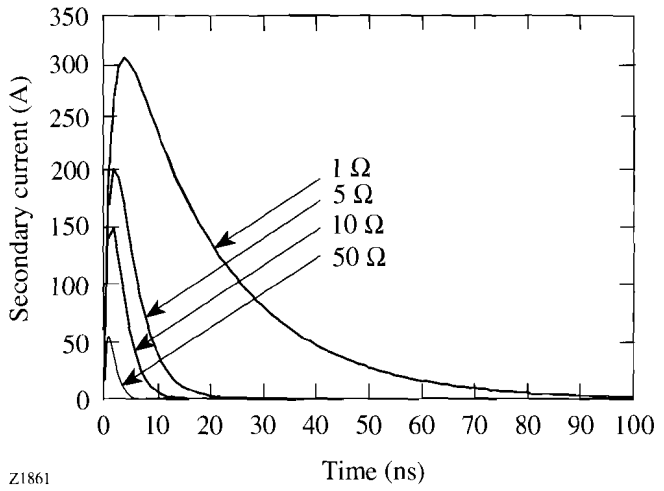

Figure 61.18
The simulated current pulse produced at a single-turn secondary coil for different values of load resistance. Two identical, 1-cm-diam, 500-nm-thick, disk-shaped superconducting films with $J_c = 5.10^7$ A/cm^2 are placed on either side of the secondary coil at a distance of 1 mm. The externally applied field (B_{ext}) is −0.2 T.

Experimental Results and Discussion

The magnet used in our experiment is a Nb-Ti solenoid cooled by liquid helium, rated at 100 A and a maximum field of 4 T. A schematic drawing of the entire experimental setup, including the cryostat and magnet, is shown in Fig. 61.16.

The secondary coil is a single-turn inductor patterned on a printed circuit board. The sample holder consists of two 2-in.-diam circular copper disks with 1-cm × 1-cm-sq windows. The films, 500-nm-thick YBCO on 1-cm × 1-cm $LaAlO_3$ substrates with $T_c > 88$ K, are placed on either side of the secondary coil and supported by the copper disks.

A Nd:YAG laser beam (λ = 1064 nm; pulse width = 150 ps) was used to illuminate the films from either side through a splitter arrangement (Fig. 61.16). A stainless steel, semirigid coaxial cable carries the secondary voltage signal out of the cryostat to a computer-interfaced oscilloscope for viewing (Fig. 61.16).

After cooling the sample to the desired temperature using liquid nitrogen or helium in zero magnetic field, the magnet was then charged at a ramp rate of 0.1 A/s up to the desired level and was maintained in persistent current mode. The magnetic field strength was measured using a Hall probe and a gaussmeter.

With the magnet charged, the switch was illuminated by the laser. The YBCO films screening the secondary coils were driven normal by this laser irradiation, which allowed the flux to penetrate. A secondary voltage (of negative sign) appeared across the load. The magnet was then discharged by heating the persistent switch, leaving some of the flux trapped in the superconductor. Driving the films normal again expelled the trapped flux, and the corresponding secondary voltage signal (of positive sign) was observed.

Figure 61.19 shows a comparison of the experimentally observed secondary voltage signal at an applied field of −0.2 T with the one obtained with the theoretical analysis described in the previous section. The simulation was done by varying J_c to match the flux associated with the output voltage pulse. The peak voltage of the simulated pulse is higher than the experimentally observed pulse because instantaneous transition to the normal slate was assumed. The critical current density required to match the flux was 1.33×10^6 A/cm^2, which

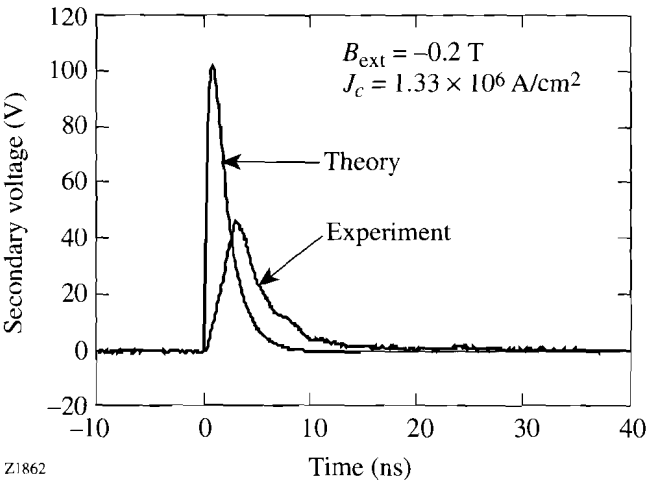

Figure 61.19
A comparison of experimentally obtained secondary voltage with the simulated voltage pulse representing the same flux. The experiment was carried out at 12.4 K, in −0.2-T field, and 8 mJ of laser energy per film.

is of the right order of magnitude but slightly lower than the value of J_c at zero field, as quoted by the film manufacturer. Possible sources of reduced effective J_c might include suppression in the magnetic field or sample inhomogeneity.

The variation of the secondary voltage signal for different laser energies is shown in Fig. 61.20. At lower laser energies, the entire bulk of the film is not heated instantaneously above the transition temperature. The 500-nm film thickness is greater than the optical penetration depth (≈120 nm); consequently the upper section of the film absorbs most of the energy when the laser pulse is incident on the film. The heat is eventually redistributed by diffusion, elevating the temperature of the entire film above the critical temperature. The heat is then redistributed throughout the remaining bulk of the film by thermal diffusion.[6] If we divide the film into a series of layers normal to the propagation direction of the incident laser radiation, the bottom layers will remain superconducting and carry the screening currents even after the top layers become nonsuperconducting. These screening currents continue to exclude flux and retard its motion. Since the secondary voltage is the temporal derivative of the flux, the peak voltage goes down, and rise and fall times increase, with the decrease in laser fluence. However, as shown in Fig. 61.20, the time integral of the secondary voltage pulse, representing the total flux that has traversed the film, is the same for pulses triggered by laser irradiation of varying intensity. Based on these results,

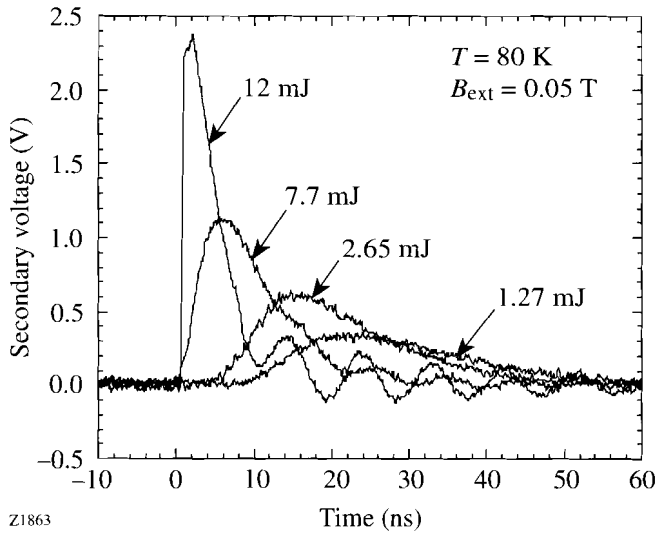

Figure 61.20
The speed of flux motion depends on the incident laser energy. For lower laser energy the bottom part of the film remains superconducting for a while, impeding the motion of flux. The film was a 1-cm-diam disk with a thickness of 500 nm.

we can conclude that higher laser fluence will give rise to faster signals with higher peak voltage. The energy (E) delivered to the load is given by $E = 1/R \int V^2(t)dt$, where R is the load resistance and $V(t)$ is the voltage across the secondary. For the same flux, $\Phi = \int V(t)dt$, a faster signal will deliver higher energy in the load. Both the peak voltage and the flux are larger at lower temperatures because J_c is higher.

An inductively coupled switch of the type we have described lends itself to a variety of applications. For example, in a current multiplication circuit using programmed inductive elements (PIE),[7] storage inductors are charged in series and discharged sequentially in stages that are connected in parallel with the load through a set of isolating closing switches. This circuit can be used to deliver a large load current using switches that are rated at a fraction of that current. The most important constraint in such a circuit is the synchronization of the opening switches with the closing switches. If the opening switches in this circuit are not triggered within a short temporal window, transient high current or voltages will catastrophically destroy the circuit elements. Optical triggering provides accurate timing. The optically triggered inductive opening switch will be suitable in circuits with such constraints.

The contactless arrangement of our switch is especially suited for applications such as energy extraction from SMES,[8–9] though there are some unresolved problems. The main application of SMES is as a backup source of energy to be delivered to the load in a crisis situation. If an opening switch is placed in series with the magnet winding, the finite closed-state resistance of the switch results in a continuous loss of energy while the system is idle. A contactless switch will solve this problem; the film properties, however, will need to be significantly improved for this design to be practical for high-power applications.

Conclusion

We have described the flux dynamics in a contactless opening switch. The switching is performed by the optical heating of YBCO thin films, which in their superconducting state screen the flux coupling between two inductively coupled circuits. A single-turn secondary coil with a small L/R time produces a fast voltage pulse. The rise time of the output signal is about 1 ns. At lower temperatures the critical currents are higher and can screen higher fields. Fast voltage pulses of 100 V and higher are possible and may have switching applications. We have developed a theoretical model, supported by experimental evidence, that can be used as a diagnostic tool to study flux motion.

ACKNOWLEDGMENT

This work was supported by BMDO through ONR Contract #N00014-92-J-1993, Rochester Gas and Electric, NSF Grant #DMR-9122727, the New York State Energy Research and Development Authority, and the Frank J. Horton Graduate Fellowship Program.

REFERENCES

1. E. M. Honig, in *Opening Switches*, edited by A. Guenther, M. Kristiansen, and T. Martin, Advances in Pulsed Power Technology, Vol. 1 (Plenum Press, New York, 1987), pp. 1–48.

2. D. Gupta, W. R. Donaldson, K. Kortkamp, and A. M. Kadin, IEEE Trans. Appl. Supercond. **3**, 2895 (1993).

3. J. H. Claassen, M. E. Reeves, and R. J. Soulen, Jr., Rev. Sci. Instrum. **62**, 996 (1991).

4. D. Gupta, W. R. Donaldson, and A. M. Kadin, submitted to the Journal of Applied Physics.

5. P. N. Mikheenko and Yu. E. Kuzovlev, Physica C **204**, 229 (1993).

6. D. Gupta, W. R. Donaldson, K. Kortkamp, and A. M. Kadin, in *Optically Activated Switching II*, edited by G. M. Loubriel (SPIE, Bellingham, WA, 1992), Vol. 1632, pp. 190–195.

7. T. Burke *et al.* (private communication); also presented at the IEEE's High Voltage Workshop, Monterey, CA, March 1988.

8. W. R. Donaldson, D. Gupta, and A. M. Kadin, U. S. Patent No. 5,339,062 (16 August 1994).

9. D. Gupta, W. R. Donaldson, and A. M. Kadin, in *Advances in Cryogenic Engineering*, edited by P. Kittel (Plenum Press, New York, 1994), Vol. 39, Part B, pp. 2015–2020.

Slurry Particle Size Evolution During the Polishing of Optical Glass

Significant advances have been made in the fabrication of glass optical components since Newton's time, especially in the mechanically dominated grinding operations; however, optical polishing remains a very challenging finishing operation, primarily because of uncontrolled chemical factors and associated chemo-mechanical interactions. Most modern fabrication shops still rely on the specialized skills of experienced opticians to manage the complex system of polishing agent, fluid, glass work, and polishing tool. As an added source of difficulty, the proprietary nature of compositional data for some of the system elements (especially the glass work and polishing agent) means that knowledge of the initial process conditions is usually incomplete. Coupled with inherently low glass removal rates, the optician's labor makes polishing the most expensive operation in precision optical fabrication.

In this article, evolution of the slurry particle size distribution during aqueous glass polishing is investigated. Our primary focus is on the role of slurry fluid chemistry, which can also be influenced by the in-process dissolution of glass constituents.[1] This issue is especially significant in commercial polishing processes, where recirculation of the slurry is an economic necessity. The discussion here is limited to three glass types (Corning 7940 fused silica, Schott BK7 borosilicate crown, and Schott SF6 dense flint) and three polishing agents (CeO_2, monoclinic ZrO_2, and nanocrystalline α-Al_2O_3). A more extensive treatment of the subject, including materials of purely academic interest, may be found in Ref. 2.

Introduction

In the fabrication of typical precision optical elements, the purpose of polishing is threefold: (1) to shape the glass work to within 0.1 μm ($\lambda/5$, $\lambda = 0.5$ μm) or less of the desired surface form, (2) remove subsurface damage (SSD) created by the preceding grinding operations, and (3) reduce the peak-to-valley (PV) surface roughness to less than 5 nm ($\lambda/100$). The mechanism of glass removal, while not entirely understood, is generally accepted as plastic scratching of the hydrated or corroded glass surface by a polishing agent suspended in an aqueous fluid.[3] This mechanism is considered to be the essence of the chemo-mechanical theory of glass polishing. The most common polishing agents are CeO_2 and ZrO_2 with mean particle sizes ranging from 0.01 to 3 μm. The polishing agent is supported by a viscoelastic tool made of pitch (wood or petroleum based) or polyurethane foam. Since the polishing agent sinks into the tool until the smallest grains are load-bearing, the glass removal rate is not strongly dependent on the particle size distribution within some poorly specified upper limit.[4] The total glass thickness removed is about 25 μm, with removal rates ranging from 0.1 to 1 μm/min. The creation of SSD is not an issue in the polishing of glass because, unlike grinding, there is no fracturing of the surface.

The mechanical aspects of polishing have been modeled as an area-averaged wear process using Preston's equation[5,6]

$$\frac{dz}{dt} = C_p \frac{L}{A} \frac{ds}{dt}, \tag{1}$$

where z is the height at a point on the surface of the glass work, C_p is Preston's coefficient (units of area/force), L is the total load, A is the area over which wear occurs, and s is the path traveled by the work relative to the tool. This equation predicts that the glass removal rate at any point on the surface is proportional to the local pressure (L/A) and velocity (ds/dt). The term C_p is generally used as either a fitting parameter or an empirical measure of polishing efficiency.[7,8] The latter use is made clear by solving Eq. (1) for C_p in terms of polishing process parameters:

$$C_p = \frac{1}{\rho L} \frac{\Delta m}{\Delta s}, \tag{2}$$

where ρ is the density of the glass work, Δm is the mass lost by the glass work during a given interval of polishing time, and Δs is the total path length traveled by the tool across the work during the same time interval. Typically reported values of C_p are of the order of 10^{-14} cm^2/dyne (10^{-13} Pa^{-1} or 9.806×10^{-7} mm^2/kgf).[4,8,9]

Preston's deceivingly simple model lacks an explicit accounting of the role of process chemistry. This point is clarified by the work of Brown *et al.* on purely abrasive (i.e., chemically inactive) polishing of metals.[10] For this specific case, they proposed an expression for C_p that is proportional to the inverse of Young's modulus of the bulk metal. If glass polishing was also a purely abrasive process, then there would be no hydrated surface layer. The corresponding value of C_p, calculated using the value of Young's modulus for the bulk glass, would be of the order of 10^{-12} cm^2/dyne, which is two orders of magnitude larger than typically reported empirical values. A major portion of this discrepancy is most likely due to three chemistry-related processes: (1) the complex hydration/corrosion of multicomponent silicate glass, (2) redeposition of silica species during polishing, and (3) surface charging of the glass work and the polishing agent. Cook's review of these processes and his proposed rate model suggested a number of interesting experiments, particularly relating to the influence of surface charge on mass transport during polishing.[4] This was a precursor to the trend of increasing interest in surface charge effects in the microgrinding[11] as well as polishing[9,12,13] of optical glass.

Hunter has summarized the mechanisms for the spontaneous separation of electric charges in systems consisting of oxides and fluids.[14] The mechanisms relevant to such systems consisting of two material phases are

(a) differences in the affinity of the two phases for ions of opposite charge, and

(b) ionization of surface groups.

Mechanism (a) involves the differential adsorption of anions or cations from the fluid onto the oxide surface as well as the differential dissolution of one type of ion over another from the oxide into the fluid. Equilibrium is established when the electrochemical potential is the same in both the oxide and fluid phases for any ion that can move freely between them.

For mechanism (b), the degree of charge development (and its sign) at the fluid-oxide interface due to ionization of surface groups on the oxide depends on the pH of the fluid. Metal-oxide surfaces typically possess a high density of amphoteric hydroxyl groups that can react with either H^+ or OH^- depending on the pH:

$$MOH_2^+ \xleftarrow{H^+} M-OH \xrightarrow{OH^-} MO^- + H_2O. \quad (3)$$

This behavior may be regarded as a specific example of mechanism (a), with H^+ and OH^- acting as the freely moving ions. These types of reactions can occur at the surface of a metal-oxide polishing agent particle as well as at an optical glass surface.

Well-developed techniques based on electrokinetic effects exist for measuring surface charge in systems containing either microscopic particles suspended in a fluid[15] or macroscopic solid bodies immersed in a fluid.[16] For suspended microscopic particles, measurement of the velocity of the particles under the influence of a known externally applied electric field permits the determination of the mobility of the particle. The mobility is related to the net electric charge, or surface potential, of the particle with respect to the bulk fluid. This technique is known as particle electrophoresis.

For the case of a macroscopic solid body, the surface charge can be determined by constraining the fluid to flow along a surface under the influence of a pressure gradient. Ionic charges at the surface tend to be swept along with the moving fluid, which results in an accumulation of charge downstream. The resultant potential difference induces an upstream electric current by ionic conduction through the fluid. A steady state is quickly established, and the measured potential difference along the portion of the surface over which the fluid is flowing is called the streaming potential. This streaming potential is related to both the pressure gradient driving the fluid motion and the surface potential of the solid with respect to the bulk fluid.

The above descriptions of electrokinetic measurement techniques refer to the term "surface potential." What is typically calculated from electrokinetic measurement data is known as the zeta (ζ) potential, defined as the average electric potential at the "surface of shear" near the solid (microscopic particle or macroscopic body) with respect to the bulk fluid potential. This surface of shear is an imaginary hydrodynamic boundary in the region of the fluid-solid interface. Between the solid surface and the surface of shear, the fluid is considered to be stationary in the reference frame of the solid.

Recent literature on polishing has referred to both the ζ potential[9,12] and the isoelectric point (IEP)[4] of the polishing agent and the glass work. The relationship between the IEP and the ζ potential can be readily understood in terms of the preceding discussion. The IEP of a hydrated surface is defined as the pH at which there is no net charge within the surface of shear, which clearly corresponds to $\zeta = 0$.

In spite of the complexity of the task, there has been recent progress toward the development of a deterministic glass-polishing model. Based on empirical data from two different sources, a polishing rate model has been proposed by Cook[4] that accounts for the single oxygen bond strength of the metal-oxide polishing agent (R-O, in kcal/mole), the pH of the fluid, and the IEP of the polishing agent:

$$R_c = \frac{1}{\log_{10}\left[(\mathrm{R-O}) \times |\mathrm{pH} - \mathrm{IEP}|\right]}. \quad (4)$$

The rate factor (R_c) is a predictor of the relative polishing activity of metal-oxide polishing agents.

Our earlier research with an atomic force microscope (AFM) showed that electrostatic forces between planar glass disks and individual metal-oxide polishing agent particles can be easily controlled by manipulating the pH of the surrounding fluid.[13] In this work, we investigate the manifestations of such chemically modulated forces in a planar continuous-polishing process and assess the effectiveness of manipulating the slurry chemistry to produce higher-quality surfaces in less time.

Experiment

Commercially available products were used in our experiments whenever feasible. Optical glass disks and polishing slurries were characterized in terms of the ζ potential. Slurries were further characterized in terms of the particle size distribution, and planar glass polishing experiments were conducted with a commercially compatible continuous polishing machine. Particle electrophoresis and streaming potential measurements were used to determine the IEP's of metal-oxide polishing agents and silicate glass types prior to actual polishing experiments.

1. Materials

Three glass types commonly used for precision optical components were examined in this study: Corning 7940 (fused silica),[17] Schott BK7 (borosilicate crown), and Schott SF6 (dense lead silicate flint).[18] Their chemical compositions[19,20] along with some of their fundamental properties[2,19,21] are listed in Tables 61.III and 61.IV, respectively. The action of three high-purity metal-oxide polishing agents on these three glass types was evaluated at three levels of slurry fluid pH (4, 7, and 10), spanning the range of values normally encountered in polishing. Two of the three polishing agents, Transelco CeO_2[22] and Norton monoclinic ZrO_2,[23] are supplied as aqueous slurries with a median particle size of 1 μm. The third polishing agent, Norton nanocrystalline α-Al_2O_3,[24] is also supplied as an aqueous slurry but with a median particle size of 0.6 μm. It is engineered for greater friability (i.e., a lower resistance to crumbling) than conventional α-Al_2O_3 grinding abrasives, thereby improving the prospects for successful glass polishing.[25]

Table 61.III: Composition of the three glass types (weight %).

Glass Type	SiO_2	B_2O_3	Na_2O	K_2O	BaO	PbO	As_2O_3
7940	99.9	–	–	–	–	–	–
BK7	68.9	10.1	8.8	8.4	2.8	–	1.0
SF6	26.9	–	0.5	1.0	–	71.3	0.3

The scope of our core experimental program was thus defined as the evaluation of 27 different combinations (3^3) of glass, polishing agent, and fluid.

2. Equipment and Methods

a. Preparation of glass surfaces. To ensure consistent initial conditions for each polishing experiment, a uniform planar

Table 61.IV: Some thermal and mechanical properties of the three glass types.

Glass Type	Transition Temp. (T_g) (°C)	α (10^{-6}C) (a)	Density (g/cm^3)	Young's Modulus (GPa)	H_v (kgf/mm^2)(b)	K_c (MPa m$^{1/2}$)(c)
7940	1075	0.5	2.20	73.1	953	–
BK7	559	7.1	2.51	81.0	772	0.86
SF6	423	8.1	5.18	56.0	465	0.44

(a) Linear thermal expansion coefficient (α) of 7940 determined over a temperature range of 5°C to 35°C.[9] α of BK7 and SF6 determined over a range of –30°C to 70°C.[21]
(b) Vickers hardness (H_v) measured using 0.05 kgf with samples immersed in water.[2]
(c) Fracture toughness (K_c) also measured using 0.05 kgf with samples immersed in water.[2] K_c is undefined here for fused silica because it does not fracture radially under such a low load.

disk geometry was adopted for all glass samples. Fine annealed plates were rough ground to a thickness of 15 mm and then core drilled to produce at least two dozen 40-mm-diam disks of each glass type. The individual disks were beveled and then processed using a controlled grinding strategy to minimize the depth of subsurface damage (SSD).[26] A cast iron tool and Microgrit #9 Al_2O_3 abrasive,[27] which has a median particle size of 5.75 μm, were used in the last fine-grinding operation. The resultant PV surface roughness was measured over a 4-mm scan length using a Pocket Surf III roughness gage,[28] and the depth of SSD was measured using a modification of the Itek ball method.[29] All surface sampling measurements, including PV roughness and SSD, were taken at five sites per disk: the center site plus the four sites within 5 mm of the edge at the 3, 6, 9, and 12 o'clock positions.

b. ζ potential and particle-size analysis. The ζ potential values of the three optical glass types were determined using a Brookhaven EKA electrokinetic analyzer.[30] Six disks of each glass type were cut and rough ground to the rectangular dimensions ($33 \times 20 \times 5$ mm) required to line the fluid cell of the Brookhaven EKA. One large face of each rectangular sample was fine ground as specified above and then polished using a pitch tool with an aqueous slurry of monoclinic ZrO_2. The polished surfaces were planar to within $\lambda/2$ with a scratch/dig quality of 60/40.[31] Samples of a given glass type were cleaned and mounted end-to-end in the upper and lower recesses of the EKA streaming potential cell with the polished surfaces exposed to the fluid. The streaming potential that developed along the surface of the glass-lined channel was measured while an electrolyte solution (1×10^{-3} M aqueous KCl) was forced, by external pressure, to flow along the surface. The pH values were varied between 3 and 10 by adding either HCl or NaOH to the transport electrolyte. The ζ potential values, calculated from the streaming potential measurements using the Briggs method,[15,16] were plotted as a function of fluid pH. The corresponding IEP values of each glass type (pH at which $\zeta = 0$) were obtained by interpolation.

The ζ potential values of the three polishing agents were determined using a Brookhaven ZetaPlus zeta potential analyzer,[32] which measures the electrokinetic mobility of particles suspended in a fluid using electrophoretic light scattering (ELS). The ζ potential, calculated from the electrokinetic mobility using the Smoluchowski equation,[15] was measured with the polishing agents suspended in water as well as in aqueous solutions of NaCl and catechol ($1,2\text{-}(HO)_2C_6H_4$). Catechol was chosen as a fluid additive because of its reported role as a potential silica sequestering agent during polishing with pitch tools.[4,9,33] Since a salt-rich, aqueous environment is known to effectively screen out electrostatic interactions near macroscopic oxide surfaces[34] and between particles in colloidal systems,[35,36] NaCl was also chosen as a fluid additive. Samples of each of the three slurries as received from the manufacturers were diluted (10:1) with three different carrier fluids: deionized water, aqueous catechol (500 ppm, 4.5×10^{-3} M), and aqueous NaCl [500 ppm, (0.01 M)]. The catechol concentration was chosen based on the maximum conceivable evolution of analogous compounds from a pitch polishing tool in recirculated slurry systems.[37] The maximum salt concentration was limited by the electrolytic current handling capability of the ZetaPlus instrument. Small working volumes of the nine polishing agent/fluid combinations were prepared at three pH values (4, 7, and 10) adjusted by the addition of HCl or NaOH. Measured ζ potential values of each polishing agent/fluid combination were then plotted as a function of pH, and the corresponding IEP values were obtained by interpolation.

The particle size distribution of polishing slurries was measured using a Horiba LA900.[38] This instrument optically determines the size of particles suspended in a fluid over a range of 0.04 to 1000 μm by combining Fraunhofer diffraction and Mie scattering information.[39] Typically, two or three droplets of a given slurry were dispersed directly into the carrier fluid ($V \approx 250$ ml) of the LA900. An aqueous solution of an anionic surfactant [$(NaPO_3)_6$, 0.2% by weight] was used as the carrier fluid to prevent any agglomeration of the suspended metal-oxide particles. The diluted slurry was recirculated through the LA900 until the forward-scattered red light ($\lambda = 633$ nm) signal stabilized, indicating uniform mixing. The particle size distribution was then measured and stored as a 74-bin histogram.

c. Glass polishing experiments. Glass polishing experiments were conducted on a custom-built, 535-mm-diam continuous polishing machine (CPM) with a 297-mm-diam conditioner and a pair of 178-mm-diam work rings (for individual work pieces). The theory and operational considerations of this planar polishing machine have been presented elsewhere by Preston[5] and Cooke *et al.*[40] and will not be discussed here. Unique features of our CPM include a vacuum-activated slurry agitation/recirculation system,[11] a mechanical agitator in the outer catchment trough to prevent liquid/solid separation by settling, and *in situ* measurement of the frictional force (F_T) between the polishing tool and an individual 40-mm-diam glass work piece using an Entran load cell.[41] The overall sensitivity of the frictional force measurement system is approximately ±0.1 N.

Given the ambitiously large number of material combinations to be evaluated and the need to eliminate any chemical carryover between experiments, polyurethane foam was used instead of pitch as the polishing tool. Although this choice simplifies tool replacement between experiments, the surface figure of the work, or edge roll-off, was compromised. On the basis of cost and the availability of die-cut sheets large enough to cover the 535-mm-diam turntable of our CPM, we selected a 0.5-mm-thick blown polyurethane pad, Rodel HSP.[42] The open cellular structure of this material provides a high density of sites for retaining polishing agent particles, which is a necessary condition for efficient glass removal during polishing with any polyurethane tool.[43]

The primary role of the CPM conditioner in our polishing experiments was to dominate the process chemistry by providing a significant surface area for tool/slurry/glass interactions. The conditioner also functioned as a truing device by shearing off any local asperities on the surface of the polyurethane tool.[44] To isolate glass-specific chemical effects, a separate conditioner was prepared for each of the three glass types that were polished. Each conditioner was fabricated by blocking 17 individual glass disks (40-mm diam, 15 mm thick) to a large Pyrex disk (297-mm diam, 25 mm thick). Since the functional surface of the conditioner was made of the same glass type as the individual work piece in the frictional force measurement system, only the particular glass type being studied in a given experiment participated in the process chemistry. This choice of common glass types essentially eliminated any competing effects that could be attributed to a different conditioner material.

A consistent CPM operational procedure was followed in each of the glass polishing experiments. Since chemistry-related issues were our primary concern, constant values of pressure (40 gf/cm^2) and synchronous rotation rate (9 RPM for the turntable and work rings) were maintained throughout the experiments.

At the conclusion of each experiment, the roughness of a blocked disk near the center of the conditioner was measured using a Zygo Maxim-3D laser interference microscope.[45] The surface figure of the glass work and the conditioner disk was evaluated using a Davidson Optronics Fizeau interferometer, which has a He-Ne laser source ($\lambda = 632.8$ nm) and a 127-mm-diam reference flat for testing planar surfaces.[46]

The glass removal rate ($\Delta z/\Delta t$) was calculated from the mass loss (Δm) of the glass work over a given time interval (Δt) using[11]

$$\frac{\Delta z}{\Delta t} = \frac{1}{\rho A}\frac{\Delta m}{\Delta t}, \tag{5}$$

where ρ is the glass density and A is the area of the work in contact with the polyurethane pad. The mass loss was determined by weighing the work before and after polishing using an analytical balance with a reproducibility (one standard deviation) of 20 μg. The maximum uncertainty in the reported glass removal rates was 3%.

A typical polishing experiment required approximately 7 h, including cleanup time. The polyurethane pad was replaced whenever an experiment called for a change in glass type or polishing agent. New pads were preconditioned by an 8-h polishing session with the slurry and glass type of interest, which ensured that the pad was fully charged with polishing agent particles.

Results and Discussion

1. Glass Surface Conditions prior to Polishing

The surface conditions of each glass type following fine grinding with #9 Al_2O_3 abrasive are summarized in Table 61.V in terms of the PV roughness and depth of SSD. The results clearly demonstrate that the performance of a given loose abrasive grinding operation is highly dependent on the glass type. From Table 61.V, we see that only 7940 follows the constant SSD-to-PV roughness ratio of 4.0 (±0.4) for loose abrasive grinding advanced by Aleinikov.[47] The two multicomponent glass types, BK7 and SF6, have significantly lower SSD-to-PV roughness ratios.

Table 61.V: Roughness and subsurface damage of the three glass types after fine grinding with #9 Al_2O_3 abrasive.

Glass Type	PV Roughness (μm) (average of five sites)	Standard Deviation (μm)	SSD Depth (μm) (average of five sites)	Standard Deviation (μm)
7940	2.2	0.3	8.1	0.6
BK7	2.4	0.5	5.3	0.4
SF6	4.2	0.7	4.0	0.2

2. Isoelectric Point (IEP) Values of Optical Glasses and Polishing Agents

The pH dependence of the ζ potential values obtained for each glass type using the Brookhaven EKA instrument is

shown in Fig. 61.21. The corresponding IEP values of each glass type, obtained by interpolation, are listed in the legend.

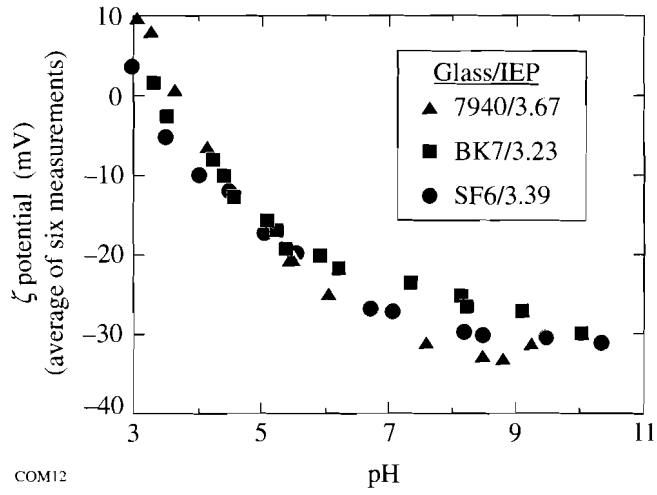

Figure 61.21
Zeta potential of 7940, BK7, and SF6 versus fluid pH. The pH was adjusted by the addition of HCl or NaOH to the transport fluid (1×10^{-3} M aqueous KCl). Error bars ≤ ±2 mV (±3 standard deviations) have been omitted for clarity.

Several important observations can be made concerning the results shown in Fig. 61.21:

- The measured value of the IEP of 7940 is in excellent agreement with that reported by Jednacak *et al.* for vitreous silica.[48]

- The ζ potential values of the three glass types are all negative (i.e., the surfaces are negatively charged due to the dissociation of OH groups) for the entire range of pH values usually encountered in optical polishing ($4 \leq pH \leq 10$).

- While the presence of significant amounts of intermediates and/or modifiers in BK7 and SF6 results in only a modest reduction of their IEP values relative to that of 7940, the ζ potential values are fairly distinctive for pH values between 6 and 9. This behavior is caused by differences in the density and charging characteristics of active surface oxide species, ostensibly due to the compositional differences between the three glass types.

The ζ potential values of each polishing agent were measured in all nine combinations of fluid additive and pH using the Brookhaven ZetaPlus instrument. The results for each polishing agent/fluid combination, when plotted as a function of pH, allowed us to determine the IEP values by interpolation, as shown for nanocrystalline Al_2O_3 suspended in aqueous catechol in Fig. 61.22. The IEP values for the eight remaining combinations of polishing agent and fluid additive were obtained by similar means and are summarized in Table 61.VI. The IEP values published by Cook[4] are also included in the table for reference.

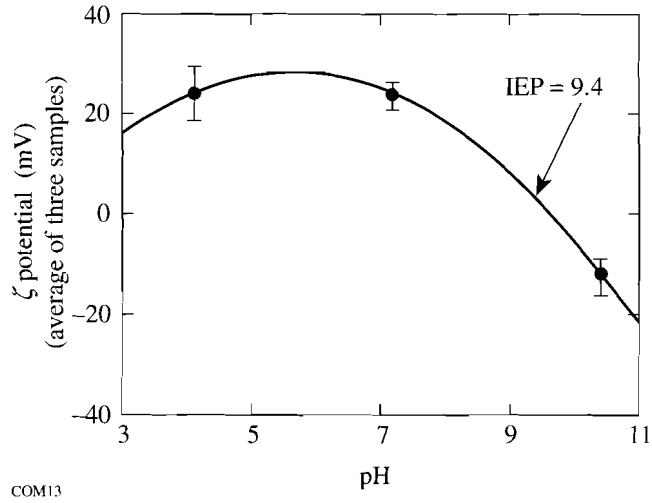

Figure 61.22
Zeta potential of the nanocrystalline Al_2O_3 polishing agent diluted in aqueous catechol (500 ppm, 4.5×10^{-3} M) versus fluid pH. The pH was adjusted by the addition of HCl or NaOH to the fluid. The data shown represents an average of three samples with ±1 standard deviation error bars.

A remarkable feature of the data in Table 61.VI is the consistency between the measured and previously published IEP values for nanocrystalline Al_2O_3, which is an indication of the lack of specifically adsorbed ions on the surface of the polishing agent.[49] Conversely, the IEP values of CeO_2 and ZrO_2 are very sensitive to the fluid chemistry. The presence of either additive reduces the IEP values of both polishing agents, which suggests that catechol and NaCl provide ions that are specifically adsorbed at the surfaces of CeO_2 and ZrO_2. These results are considered valid only in the absence of mechanical action since individual polishing agent particles are not subjected to mechanical forces that might cause them to crumble during ζ potential measurements. The total active surface area of the polishing agent particles also remains essentially constant, unlike the case when glass is polished.

3. Original Particle Size Distribution and Friability of the Polishing Agents

The original particle size distribution of each slurry as re-

Table 61.VI Isoelectric point (IEP) values of the three polishing agents in deionized water, aqueous catechol, and aqueous sodium chloride.

Polishing Agent	IEP previously published (Ref. 4)	IEP measured in deionized water	IEP measured in catechol (aq) (4.5×10^{-3} M) (500 ppm)	IEP measured in NaCl (aq) (1.0×10^{-2} M) (584 ppm)
CeO_2	6.8	8.8	7.0	7.3
m-ZrO_2	6.2	6.3	3.0	5.0
n-Al_2O_3	9.5	9.3	9.4	9.3

ceived from the manufacturers was measured using the Horiba LA900 instrument. All three polishing agents fall within the median particle size range of 0.01 to 3.0 μm that is typical of precision polishing operations, as shown in Table 61.VII.

Table 61.VII Original particle size statistics of the three polishing agents.

Polishing Agent	Median Size (μm)	Maximum Size (μm)	Minimum Size (μm)
CeO_2	1.00	4.47	0.23
m-ZrO_2	1.34	5.12	0.23
n-Al_2O_3	0.59	5.12	0.26

The friability of each polishing agent was assessed by evaluating particle size distribution in recirculated slurry samples exposed to 20-kHz, 40-W ultrasound in the LA 900 instrument. These measurements were conducted between successive, 3-min exposures to ultrasound.

Figure 61.23 illustrates the effect of ultrasonic energy on the particle size distribution of CeO_2. The initial distribution (t = 0 min) is bimodal, with the dominant mode representing the larger particles in the population. After 3 min of ultrasonic exposure, the distribution character is reversed, with the dominant mode representing the smaller particles in the population. Evidently, the ultrasonic energy induced a significant fraction of the CeO_2 particles to break apart. After 6 min (not shown) and 9 min of ultrasonic vibration, the size distribution shifts further toward smaller particle diameters, but not as dramatically as within the first 3 min.

The effect of ultrasonic energy on the median particle size of all three polishing agents is shown in Fig. 61.24. Based on the decaying exponential character of the size dependence shown in the figure, we can define an empirical ultrasonic friability index F_{us} as

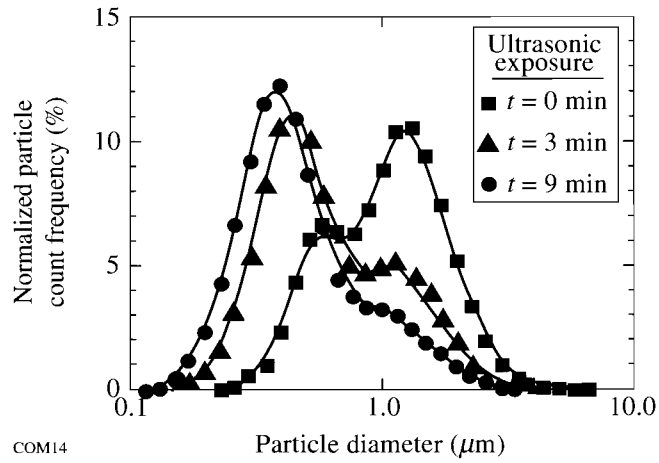

Figure 61.23
Effect of ultrasonic energy on the particle size distribution of the CeO_2 slurry. Particle size measurements were performed between successive 3-min exposures to ultrasound (40 W, 20 kHz). For clarity, the t = 6 min. distribution has been omitted.

$$F_{us} = -\frac{1}{U}\ln\left(\frac{D}{D_0}\right), \tag{6}$$

where D is the median particle size measured after exposure to ultrasonic energy U and D_0 is the original median particle size. This friability index F_{us} is a useful measure of the relative change in median particle size per unit of ultrasonic energy, i.e., the more friable the polishing agent, the larger the value of F_{us}.

The median particle size and corresponding value of F_{us} for all three polishing agents after 3 and 6 min of ultrasonic exposure are listed in Table 61.VIII. The original median particle size (t = 0) is also given in Table 61.VIII for convenient reference. In terms of F_{us}, nanocrystalline Al_2O_3 is the most friable polishing agent, followed in decreasing order by CeO_2 and monoclinic ZrO_2.

Table 61.VIII: Median particle size and ultrasonic friability index of the three polishing agents.

Polishing Agent	Median Size (μm) (t = 0 min)	Median Size (μm) (t = 3 min)	F_{us} (t = 3 min) ($\times 10^{-5}$/J)	Median Size (μm) (t = 6 min)	F_{us} (t = 6 min) ($\times 10^{-5}$/J)
CeO_2	1.00	0.50	9.6	0.43	5.9
m-ZrO_2	1.34	0.89	5.7	0.87	3.0
n-Al_2O_3	0.59	0.29	9.9	0.21	7.2

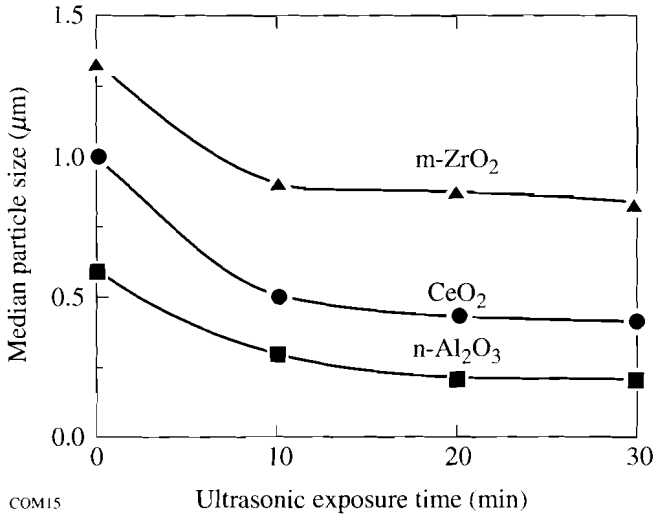

Figure 61.24
Effect of ultrasonic exposure time on the median particle size of the polishing agents.

4. Glass Polishing Experiments

Two preliminary experiments with the CPM were conducted using the most commercially important glass and polishing agents, BK7 and CeO_2, respectively. The goals of these experiments were

- to assess the in-process evolution of slurry particle size over a prolonged period of polishing, and
- to study the effect of catechol and NaCl as slurry additives.

The core experiments were then conducted using all 27 combinations of polishing agent, glass type, and slurry fluid pH. The results of each experiment are discussed below.

a. Assessment of in-process particle size evolution. The effective working lifetime of the polyurethane pad and slurry was initially determined by running the CPM with a new pad, a BK7 work and conditioner, and a fresh batch of CeO_2 slurry at pH 7 for 30 consecutive hours. The mass loss of the work and the slurry particle size distribution were measured hourly for the first 8 h, then at 15- and 30-h intervals.

The resulting glass removal rate and median particle size are plotted versus polishing time in Fig. 61.25. The glass removal rate is seen to stabilize after 6 h, which validates the need to condition new pads for at least this length of time. Between 8 and 30 h of polishing, the glass removal rate is essentially constant. This experiment established a reasonable minimum pad lifetime of 30 h, which was never exceeded during the remaining CPM experiments.

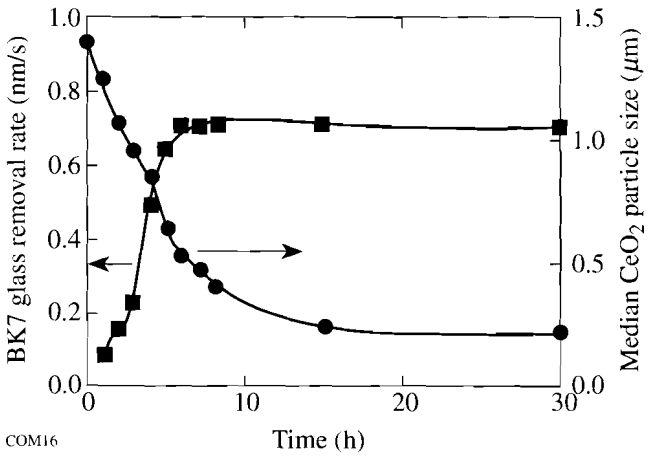

Figure 61.25
Removal rate of BK7 and the corresponding median size of the CeO_2 polishing agent versus polishing time.

After 6 h of polishing, the median CeO_2 particle size was reduced to 0.64 μm (approximately 50% of the initial value). Comparison of Figs. 61.24 and 61.25 suggests an equivalence relationship between 6 h of BK7 polishing under these conditions with 3 min of ultrasonic vibration in the Horiba LA900. These results also serve as a reminder that the glass polishing process also functions as a milling process for the polishing agent.

b. Effect of catechol and sodium chloride as slurry additives. Our earlier AFM screening experiments[13] revealed that catechol and NaCl function only to buffer mildly the forces between individual metal-oxide particles and polished glass surfaces. Their strong influence on the measured IEP values of CeO_2 and ZrO_2, as indicated in Table 61.IV, suggests the possibility of more-complex interactions between slurry particles. To resolve this issue, we studied the effect of catechol and NaCl as slurry additives using the CPM.

The average BK7 glass removal rate obtained during 4 h of polishing with aqueous CeO_2 slurries containing no slurry fluid additive, aqueous catechol (500 ppm, 4.5×10^{-3} M), and NaCl (5% by weight, 0.86 M) is plotted as a function of slurry pH in Fig. 61.26. At each of the three pH levels, the relative effect of the additives on the glass removal rate was quite consistent. The additive-free slurry fluid yielded the maximum removal rate, followed by aqueous catechol and aqueous NaCl. The maximum removal rate was obtained with no additive at pH 7. In contrast with the glass removal rate, the final rms surface roughness values (average of five measurements) of the conditioner for all nine combinations of slurry fluid additive and pH were nearly indistinguishable, averaging from only 10 to 16 Å.

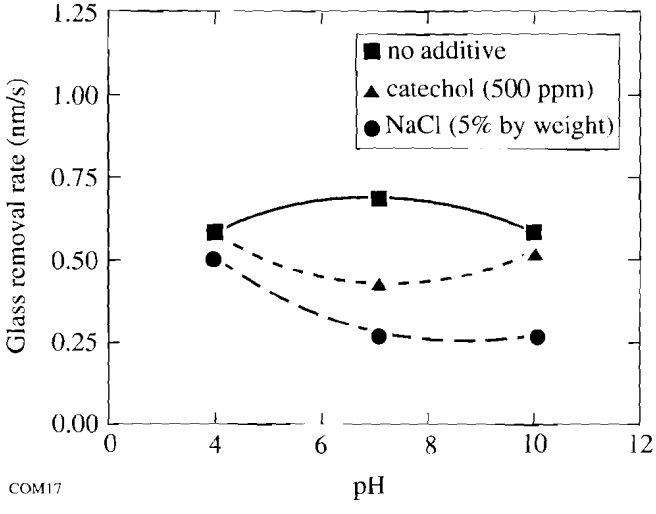

Figure 61.26
Glass removal rate as a function of slurry pH and slurry additive for polishing of BK7 with CeO_2.

These results demonstrate that, in terms of final BK7 surface roughness, the performance of CeO_2 is insensitive to significant variations in fluid chemistry. This insensitivity to fluid chemistry variations implies that an insignificant level of specifically adsorbed ions evolve from BK7 glass during the polishing process. There also is a penalty for using either catechol or NaCl as a slurry additive between pH 4 and pH 10, as evidenced by the lower glass removal rate. Since these additives made no significant impact on the polishing process, they were excluded from the remaining experiments.

c. Core glass polishing experiments. The results of the 27 core polishing experiments with CeO_2, monoclinic ZrO_2, and nanocrystalline Al_2O_3 are summarized in Table 61.IX. The range of data presented includes the average glass removal rate (RR) during each 4-h polishing session, the corresponding value of Preston's coefficient (C_p), the coefficient of friction (μ) between the work and the polyurethane pad, the final rms surface roughness of the conditioner, and the ratio of the final and original median particle size (D_f/D_0) of the slurry.

A careful review of Table 61.IX shows that polishing slurries containing monoclinic ZrO_2 are clearly the least sensitive to glass type or slurry pH, while those containing nanocrystalline Al_2O_3 are the most sensitive to these chemistry-related process factors. The CeO_2 results are intermediate to the other two polishing agents. This ordering of chemical sensitivity is identical to the ultrasonic friability index ordering (Table 61.VIII) but is contrary to the IEP stability (Table 61.VI). This apparent inconsistency can be reconciled if the available surface area of the polishing agent is taken into account. From Eq. (3), the total number of hydroxyl groups able to participate in ionization reactions scales with the combined surface area of the polishing agent particles in the recirculated slurry. Highly friable polishing agent particles will crumble progressively with use, exposing new active surface groups and accentuating the chemical aspect of their performance.

The coefficient of friction (μ) has been shown previously to be a good quantitative indicator of the efficiency of glass removal[9,12] and, as such, is a useful element with which to begin quantitative interpretation of the data in Table 61.IX. In Fig. 61.27, C_p is plotted as a function of μ for all 27 core polishing experiments. Although there are a number of outlying points, the reasonably good linear correlation ($r^2 = 0.718$) confirms quantitatively that μ may be regarded as a measure of the useful mechanical work done during polishing. Those process conditions that induced a value of μ in excess of 0.4 always resulted in a value of C_p characteristic of efficient mass transport away from the work ($\geq 10^{-13}$ cm^2/dyne).

If one studies the effect of slurry pH on the efficiency of glass removal, an interesting pattern emerges from the data.

Table 61.IX: Results of the core polishing experiments.

Polishing Agent	Glass Type	Slurry pH	RR (nm/s)	C_p ($\times 10^{-14}$ cm^2/dyne)	Friction Coefficient (μ)	rms Roughness (Å)	D_f/D_0
CeO_2	7940	4	0.141	2.2	0.27	13	1.22
"	"	7	0.215	3.3	0.31	12	1.11
"	"	10	0.200	3.1	0.30	10	0.61
"	BK7	4	0.582	8.9	0.32	16	2.36
"	"	7	0.680	10.4	0.41	13	0.55
"	"	10	0.580	8.8	0.29	11	0.25
"	SF6	4	0.270	4.1	0.32	478	1.78
"	"	7	0.104	1.6	0.28	308	0.37
"	"	10	0.788	12.0	0.48	13	0.51
m-ZrO_2	7940	4	0.307	4.7	0.35	13	0.85
"	"	7	0.241	3.7	0.35	12	0.20
"	"	10	0.253	3.8	0.33	13	0.47
"	BK7	4	0.673	10.3	0.38	19	2.15
"	"	7	0.530	8.1	0.40	16	0.80
"	"	10	0.524	8.0	0.37	14	0.62
"	SF6	4	1.110	16.9	0.49	24	1.36
"	"	7	0.733	11.2	0.48	21	0.83
"	"	10	0.778	11.8	0.48	14	0.76
n-Al_2O_3	7940	4	0.123	1.9	0.28	243	0.54
"	"	7	0.033	0.5	0.25	167	3.92
"	"	10	0.147	2.2	0.31	16	0.56
"	BK7	4	0.353	5.4	0.32	24	0.64
"	"	7	0.029	0.4	0.24	66	3.75
"	"	10	0.364	5.5	0.29	10	0.29
"	SF6	4	0.713	10.9	0.38	19	0.80
"	"	7	0.077	1.2	0.34	609	4.00
"	"	10	0.966	14.7	0.41	12	0.56

Except for the case of CeO_2 and SF6, a glass prone to selective corrosion of the PbO network modifier in acidic to neutral fluids,[50] each polishing agent exhibits a unique, glass-independent optimum pH for the maximum removal rate. For CeO_2, monoclinic ZrO_2, and nanocrystalline Al_2O_3, the glass removal rates were maximized at pH 7, 4, and 10, respectively. Returning to Table 61.VI, these optimum pH values roughly correspond to the respective IEP values measured in the presence of specifically adsorbed ions (i.e., in 0.01-M aqueous NaCl). An abundance of such ions was assumed to be present during our polishing experiments because of the dissolution of glass constituents and the use of HCl or NaOH to adjust the slurry pH. Given this assumption, our results are partially consistent with Cook's rate model, which predicts a maximum glass removal rate for a given polishing agent if the slurry pH is close to the IEP of the polishing agent [Eq. (4)]. However, as shown in Figs. 61.28–61.31, the reliability of the rate constant (R_c) as a predictor of glass removal rates is suspect. This reliability issue is especially apparent in Figs. 61.30 and 61.31, which show that R_c is not positively correlated with removal rates obtained in fluids that are corrosive to the glass.

The optimum pH for maximum glass removal did not result necessarily in the smoothest possible surfaces, which is a primary objective of polishing. Minimum surface roughness values for all nine combinations of polishing agent and glass

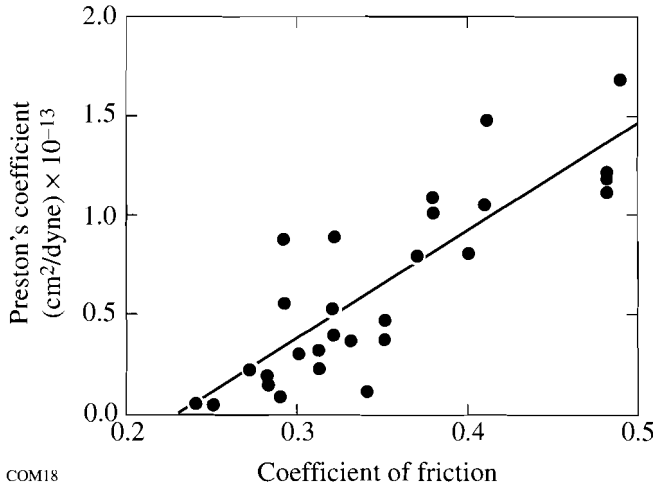

Figure 61.27
Preston's coefficient versus the coefficient of friction between the glass work and the polyurethane pad.

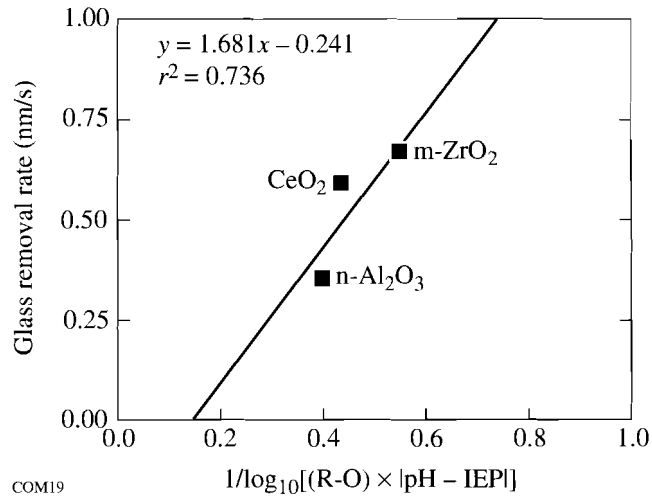

Figure 61.28
Glass removal rate versus the rate constant [4] for BK7 polishing at pH 4. (R-O) is the single oxygen bond strength (units of kcal/mole) of the polishing agent.

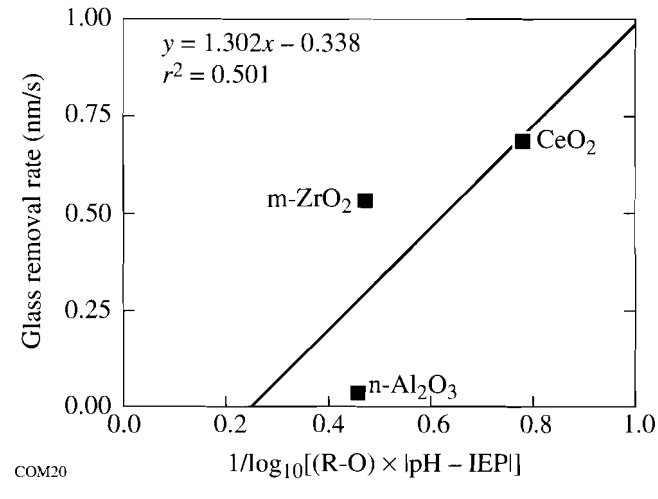

Figure 61.29
Glass removal rate versus the rate constant [4] for BK7 polishing at pH 7. (R-O) is the single oxygen bond strength (units of kcal/mole) of the polishing agent.

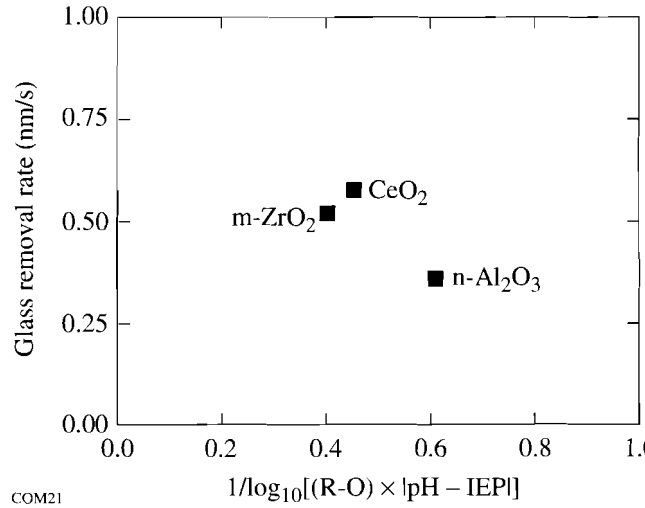

Figure 61.30
Glass removal rate versus the rate constant [4] for BK7 polishing at pH 10. (R-O) is the single oxygen bond strength (units of kcal/mole) of the polishing agent.

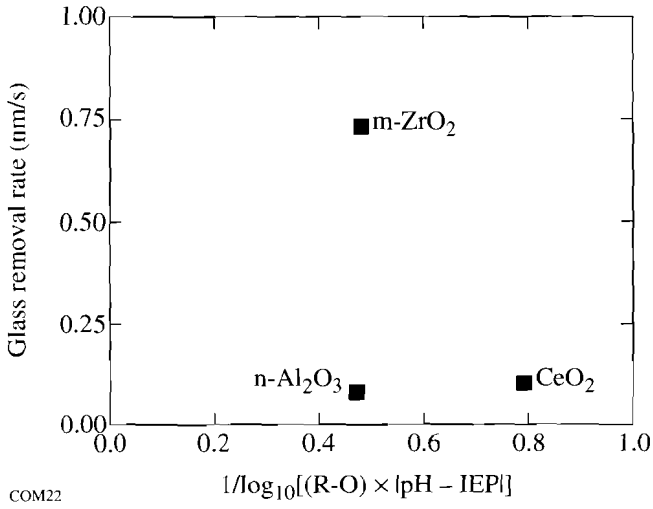

Figure 61.31
Glass removal rate versus the rate constant [4] for SF6 polishing at pH 7. (R-O) is the single oxygen bond strength (units of kcal/mole) of the polishing agent.

type were obtained when the slurry was maintained at pH 10. To understand this result, it should first be noted that all three polishing agents and all three glass types have a negative surface charge density at pH 10. As indicated by D_f/D_0, significant in-process reduction of the mean slurry particle size occurred for all nine combinations of polishing agent and glass type at this pH level. The repulsive electrostatic interparticle forces induced by the basic fluid environment inhibit the formation of agglomerates in the slurry, thereby preventing the formation of deep scratches or sleeks on the surface of the glass work. The aqueous solubility of silica, which forms the network of all three glass types, is also sharply accelerated above pH 8.[51] At pH 10, it is therefore quite plausible to expect preferential dissolution of any microscopic irregularities on the silicate surface because of their relatively high surface-area-to-volume ratios. Supportive evidence for the above can be found in the scatter diagram of Fig. 61.32, which is a plot of the average rms surface roughness values on a logarithmic scale obtained at the conclusion of each of the 27 core polishing experiments versus the difference between the fluid pH and the IEP values of the polishing agents. Each plotted symbol in Fig. 61.32 represents one polishing session for the indicated glass type and polishing agent at a given pH value. The abscissa, pH–IEP, is an opposite indicator of the sign of the surface charge on the polishing agent. Note that for pH values larger than the IEP of the polishing agent (i.e., for which the polishing agent and glass are negatively charged), the surface roughness values were, without exception, quite low. When the pH is less than the IEP, large values of roughness were observed for some combinations of polishing agent, glass type, and pH; we term this phenomenon the *slurry charge control effect.*

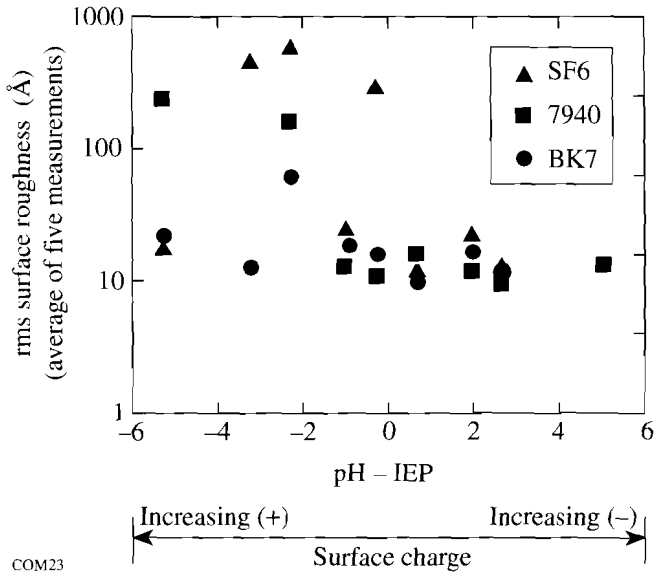

Figure 61.32
Dependence of the glass surface roughness on the difference between the fluid pH and the isoelectric point of the polishing agent (measured in 0.01-M aqueous NaCl). Each data point corresponds to a unique combination of polishing agent (CeO_2, monoclinic ZrO_2, or nanocrystalline Al_2O_3), glass type (7940, BK7, or SF6), and slurry pH (4, 7, or 10).

Interpretation of the slurry charge control effect is quite simple as summarized in Table 61.X. For glass types with a silica network, the combination of fluid and polishing agent should be selected so that the fluid pH is always larger than the IEP of the polishing agent. This precaution ensures that both the polishing agent particles and any silica species have surface charge of the same sign. As was mentioned previously, the corresponding repulsive electrostatic force inhibits agglomeration of any particles suspended in the slurry, resulting in the smoothest possible surface finishes.

Referring to Figs. 61.33 and 61.34, the polishing of 7940 with nanocrystalline Al_2O_3 provides an excellent example of the slurry charge control effect. In terms of both removal rate and surface roughness, the best results were obtained at pH 10, where both the polishing agent particles and the glass work had relatively large negative charge densities. At pH 7, where the polishing agent particles and the glass work were oppositely charged, significant agglomeration occurred, causing an increase in the surface roughness and a decrease in the removal

Table 61.X: Qualitative summary of the slurry charge control effect. *The smoothest surfaces are obtained using combinations of polishing agent and glass type with surface charge of the same sign.*

Materials	IEP	Surface Charge State at pH 4	Surface Charge State at pH 7	Surface Charge State at pH 10
Polishing Agents				
CeO_2	7.3 (a)	++	0^+	–
m-ZrO_2	5.0 (a)	+	–	– –
n-Al_2O_3	9.3 (a)	++	+	–
Glass Types				
7940	3.7 (b)	0^-	–	– –
BK7	3.2 (b)	–	–	– –
SF6	3.4 (b)	–	–	– –

(a) Measured in aqueous NaCl (0.01 M) using electrophoretic light scattering
(b) Measured in aqueous KCl (0.001M) using the streaming potential technique
++ Relatively large positive charge density
+ Relatively small positive charge density
0^+ Slight positive charge density (pH close to the IEP)
0^- Slight negative charge density (pH close to the IEP)
– Relatively small negative charge density
– – Relatively large negative charge density

rate. At pH 4, no agglomeration occurred since the polishing agent particles had a relatively high positive charge density, while the glass work had only a slight negative charge density. The removal rate in this system was nearly as high as with the pH 10 slurry. The corresponding large value of surface roughness at pH 4 is probably due to the reduced solubility of silica in the acidic environment, which inhibited corrosion of the network.

Landingham *et al.* have previously encountered agglomeration problems in the pitch polishing of fused silica with Al_2O_3.[52] In hindsight, this is not surprising since their investigation was limited to slurry pH values between 7.4 and 9.0, where silica and Al_2O_3 are oppositely charged. Although the more recent success of Tesar *et al.*[12] in the pitch polishing of fused silica with CeO_2 and monoclinic ZrO_2 at pH 4 appears to be at odds with the slurry charge control effect, their slurries were dispensed at a very low rate (1.2 ml/min.) and were not recirculated. These two process features reduced the tendency of the polishing agent to agglomerate because the accumulation of silica species in the slurry was negligible. Since no results were reported by Tesar *et al.* at pH 10, we were unable to make a more direct comparison of their results with our own.

Conclusions

The concepts and analytical tools of colloid science for characterization of surface charge effects were used in this work to demonstrate the strengths and limitations of a newly proposed polishing process rate model. The pivotal role of slurry fluid chemistry, particularly pH, in maintaining

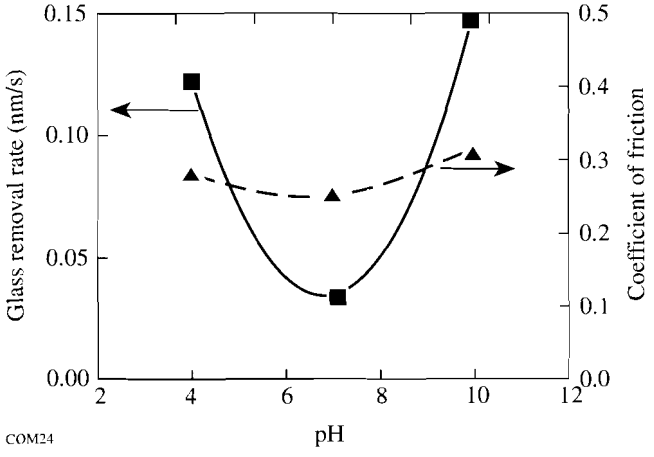

Figure 61.33
Glass removal rate and coefficient of friction between the work and the polyurethane pad as a function of slurry pH for polishing of 7940 with nanocrystalline Al_2O_3.

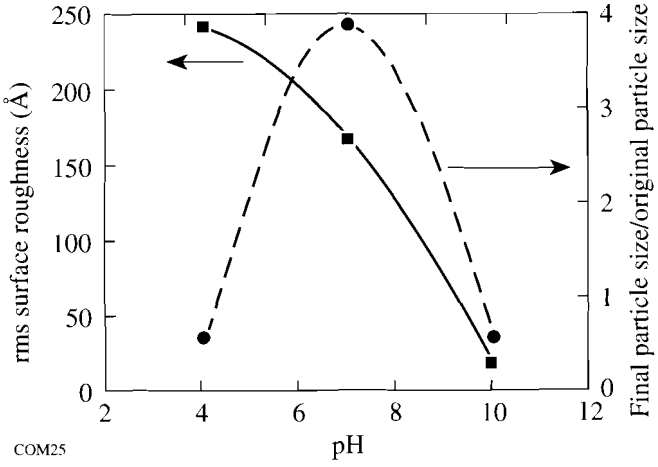

Figure 61.34
Surface roughness and the final median particle size of the slurry divided by the original median particle size as a function of slurry pH for polishing of 7940 with nanocrystalline Al_2O_3.

electrokinetically favorable conditions for a well-dispersed polishing agent was also identified and explored. For the silicate glass types studied here, these electrokinetically favorable conditions were sufficient for obtaining the smoothest possible surfaces. A relationship between fluid pH and the isoelectric point of the polishing agent, termed the slurry charge control effect, was also established, and its importance in controlling surface roughness was demonstrated. Our results have shown that there are chemically modulated forces present in the polishing system that can be equal to and, in some cases, exceed the mechanical forces and that these chemically modulated forces exert their effect at the interparticle level, not between individual particles and the glass work. The latter was most clearly demonstrated by the performance of nano-crystalline Al_2O_3, which was limited by the slurry fluid pH and not by the mechanical friability of individual polishing agent particles. The pH of the fluid and the IEP of the polishing agent were also shown to be the process parameters that, if carefully controlled, can lead to the production of higher-quality surfaces in less time.

ACKNOWLEDGMENTS

The authors extend their thanks to the following individuals and organizations for providing many helpful suggestions: T. S. Izumitani (Hoya Corporation) and L. M. Cook (Rodel Products Corp.). Glass samples were prepared under the skillful guidance of the University of Rochester's master opticians, K. H. Kubath and A. Maltsev. Generous financial support was provided by Bausch & Lomb, the Center for Optics Manufacturing (COM) through the U.S. Army Mantech Program, the New York State Center for Advanced Optical Technology (NYSCAOT), and the U.S. Department of Energy Office of Inertial Confinement Fusion under Cooperative Agreement No. DE-FC03-92SF19460.

REFERENCES

1. R. H. Doremus, *Glass Science* (Wiley, NY, 1973), Chap. 13, pp. 229–252.
2. M. J. Cumbo, "Chemo-Mechanical Interactions in Optical Polishing," Ph.D. thesis, University of Rochester, 1993.
3. T. S. Izumitani, *Optical Glass* (AIP Translation Series, NY, 1986), Chap. 4, pp. 91–146.
4. L. M. Cook, J. Non-Cryst. Solids **120**, 152 (1990).
5. F. W. Preston, J. Soc. Glass Technol. **11**, 214 (1927).
6. G. M. Sanger and S. D. Fantone, in *CRC Handbook of Laser Science and Technology*, Vol. V, Part 3, edited by M. J. Weber (CRC Press, Boca Raton, FL, 1987), pp. 461–500.
7. N. J. Brown, Lawrence Livermore National Laboratory Report MISC 4476, p. 6 (1990).
8. A. A. Tesar and B. A. Fuchs, in *Optical Fabrication and Testing Workshop*, OSA Technical Digest, Vol. 24, WB9-1 (Optical Society of America, Washington, DC, 1992), pp. 137–140.
9. A. A. Tesar and B. A. Fuchs, in *Advanced Optical Manufacturing and Testing II*, edited by V. J. Doherty (SPIE, Bellingham, WA, 1991), Vol. 1531, pp. 80–90.
10. N. J. Brown, in *Contemporary Methods in Optical Fabrication*, edited by C. L. Stonecypher (SPIE, Bellingham, WA, 1981), Vol. 306, pp. 42–57.
11. D. Golini and S. D. Jacobs, Appl. Opt. **30**, 2761 (1991).
12. A. A. Tesar, B. A. Fuchs and P. P. Hed, Appl. Opt. **31**, 7164 (1992).
13. M. J. Cumbo and S. D. Jacobs, Nanotechnology **5**, 70 (1994).
14. R. J. Hunter, *Zeta Potential in Colloid Science: Principles and Applications* (Academic Press, New York, 1981), pp. 17–18.
15. *Ibid.*, pp. 59–178.
16. D. Fairhurst and V. Ribisch, "Zeta Potential Measurements of Irregular Shape Solid Materials," in *Particle Size Distribution II*, American Chemical Society Symposium Series, No. 472, 337–353 (1991).
17. Corning 7940 fused silica, courtesy of L. Sutton, Corning Inc., Canton, NY 13617.
18. Schott BK7 (borosilicate crown) and Schott SF6 (dense flint), courtesy of A. Marker, Schott Glass Technologies Inc., Duryea, PA 18642.
19. "Corning Premium-Quality Fused Silica Low Expansion Material Code 7940," Corning Inc., Corning, NY 14830.
20. T. S. Izumitani, *Optical Glass* (AIP Translation Series, NY, 1986), p. 21.
21. Optical Glass Catalog, Schott Glass Technologies, Duryea, PA.
22. CE-RITE HP, High Purity Cerium Oxide, Code 480-G, lot # 910876, courtesy of D. Coller, Transelco Div., Ferro Corp., Penn Yan, NY 14527.
23. Zirconia Q, batch #15030492, courtesy of D. Rostoker, Saint Gobain/Norton Industrial Ceramics Corp., Worcester, MA 01615.
24. NANO-SIZE ALPHA, batch #0001-92, courtesy of D. Rostoker, Saint Gobain/Norton Industrial Ceramics Corp., Worcester, MA 01615. This is a blocky a-Al_2O_3 abrasive with individual crystallite sizes of the order of 50 nm (patent pending).
25. T. Izumitani, in *Treatise on Material Science and Technology*, edited by M. Tomozawa and R. H. Doremus (Academic, New York, 1979), Vol. 17, pp. 138–140.
26. S. D. Jacobs, "Optical Glasses and Optical Fabrication," Optics 443 course notes, University of Rochester (1994), Chap. 6, p. 11.
27. "Microgrit WCA Specifications," Micro Abrasives Corporation, Westfield, MA 01086.

28. Pocket Surf III, Federal Products Corp., Providence, RI 02905.

29. A. Lindquist, S. D. Jacobs, and A. Feltz, in *Science of Optical Finishing*, OSA Technical Digest, Vol. 9., SMC3-1 (Optical Society of America, Washington, DC, 1990), pp. 57-60. SSD measurements courtesy of T. M. Rich, Center for Optics Manufacturing, University of Rochester.

30. Brookhaven EKA, Brookhaven Instruments Corp., Holtsville, NY 11742.

31. MIL-0-13830A, Revision L, (1980).

32. Brookhaven ZetaPlus, Brookhaven Instruments Corp., Holtsville, NY 11742.

33. F. M. Ernsberger, J. Am. Ceram. Soc. **42**, 373 (1959).

34. J. Jednacak, V. Pravdic and W. Haller, J. Colloid Interface Sci. **49**, 16 (1974).

35. R. J. Hunter, *Zeta Potential in Colloid Science: Principles and Applications* (Academic Press, London, 1981), p. 249.

36. R. H. Ottewill, "Electrokinetic Properties," Fifth Annual Short Course on Colloid Science Principles & Practice, University of Massachusetts (1992), p. 7.10.

37. L. M. Cook, Rodel Products Corp., Newark, DE 19713 (personal communication, 1992).

38. Horiba LA900, Horiba Instruments Inc., Irvine, CA 92714.

39. J. S. Reed, *Introduction to the Principles of Ceramic Processing* (John Wiley & Sons, NY, 1988), pp. 90–92.

40. F. Cooke, N. Brown and E. Prochnow, Opt. Eng. **15**, 407 (1976).

41. EL Load Cell, Model #ELF-1000-100, Entran Devices, Inc., Fairfield, NJ 07004.

42. HSP, Rodel Products Corp., Scottsdale, AZ 85258.

43. J. J. Bohache, "A Study of the Optical Polishing Process," Ph.D. thesis, University of Rochester, 1978, p. 143.

44. As suggested by H. Koch, Planar Optics, Inc., Webster, NY 14580 (personal communication, 1992).

45. Zygo Maxim-3D Model 5700, Zygo Corp., Middlefield, CT 06455. Using a 20X Mirau objective, this noncontact optical profiler has a 0.1-nm vertical resolution, a field of view of 0.453×0.411 mm, and a 1.75-μm lateral resolution.

46. Davidson D305LV, Davidson Optronics Inc., West Covina, CA 91790.

47. F. K. Aleinikov, Sov. Phys.-Tech. Phy. **27**, 2529 (1957).

48. J. Jednacak, V. Pravdic, and W. Haller, J. Colloid Interface Sci. **49**, 16 (1974). The authors confined most of their study to chemically durable silica-rich glass types.

49. R. J. Hunter, *Zeta Potential in Colloid Science: Principles and Applications* (Academic Press, London, 1981), p. 233. Any ion whose adsorption at a surface is influenced by factors other than the electrical potential there (e.g., covalent bonding with surface atoms) is regarded as being specifically adsorbed.

50. J. H. Escard and D. J. Brion, J. Am. Ceram. Soc. **58**, 296 (1975).

51. R. H. Doremus, *Glass Science* (Wiley, NY, 1973), p. 243.

52. R. L. Landingham, A. W. Casey, and Roy O. Lindahl, in *The Science of Ceramic Machining and Surface Finishing II*, edited by B. J. Hockey and R. W. Rice, NBS Special Publication 562 (U.S. Government Printing Office, Washington, DC, 1979), pp. 231–245.

Effect of Thermal and Mechanical Processing on Molecular Ordering in Liquid Crystal Elastomers

Liquid crystalline polymers have been the focus of intensive research in recent years because of their potential for use in a wide range of optical as well as photonic applications.[1–3] Although the macroscopic alignment required for practical applications can be achieved by surface treatment and the application of an external electric or magnetic field, the effectiveness of these processing techniques is limited to films with a thickness less than 100 μm.[4] To overcome this problem, liquid crystalline (LC) *elastomers* have been explored in view of the relative ease with which mesogenic moieties can be aligned by stretching.[5–11] An additional feature of these materials is the ability to "lock-in" this stress-induced alignment via crosslinking of reactive side-chains to produce a three-dimensional polymer network.

Finkelmann *et al.*[12] have previously described a novel two-stage reaction scheme for the preparation of LC elastomers; this process is shown in Fig. 61.35. In the first stage, a hydrosilylation reaction was conducted on the terminal methylene groups of the polymer to obtain a partially crosslinked elastomer carrying two pendant groups: a nematogen and a methacrylate. In the second stage, a constant stress was applied to produce uniform nematic alignment followed by a second crosslinking step by means of the less-reactive methacryloyl groups. Poly(methylhydrosiloxane), with a degree of polymerization n of 120, was employed exclusively in these experiments.

In this article we describe the preparation of mesogenic elastomer systems based on two commercially available polysiloxanes, poly(methylhydrosiloxane) (n = 40) and poly(ethylhydrosiloxane) (n = 80), and their characterization by Fourier transform infrared (FTIR) spectroscopy, differential scanning calorimetry (DSC), hot-stage polarized optical microscopy, stress-strain analysis, and x-ray diffraction to elucidate the dynamic features of preparation and processing of LC elastomers.

Experimental Section

1. Materials

Poly(methylhydrosiloxane) (PMHS), $-[(CH_3)SiH-O-]_{40}-$, (0.30 Stoke, Spectrum Chemicals); poly(ethylhydrosiloxane) (PEHS), $-[(C_2H_5)SiH-O-]_{80}-$, (1.00 Stoke, Gelest); toluene (anhydrous, 99+% Aldrich Chemical Company); and a Pt-catalyst (PC072, United Chemical Technologies) were all used as received without further purification. The nematic monomer and cross-linking agents were synthesized by standard literature methods, as shown in Figs. 61.36 and 61.37.

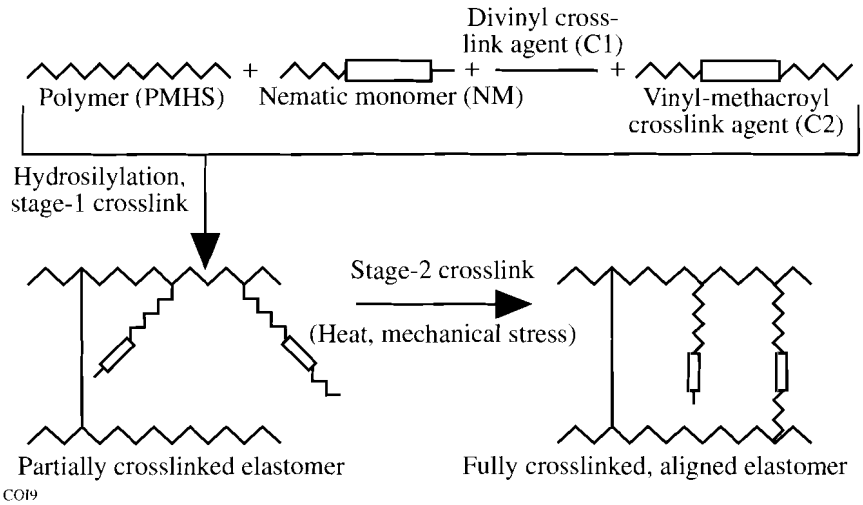

Figure 61.35
The two-step process for the preparation of aligned LC elastomers. The components are combined and reacted to form a partially crosslinked elastomer; the combination of heat and mechanical stress completes the crosslinking reaction and aligns the mesogenic pendant groups.

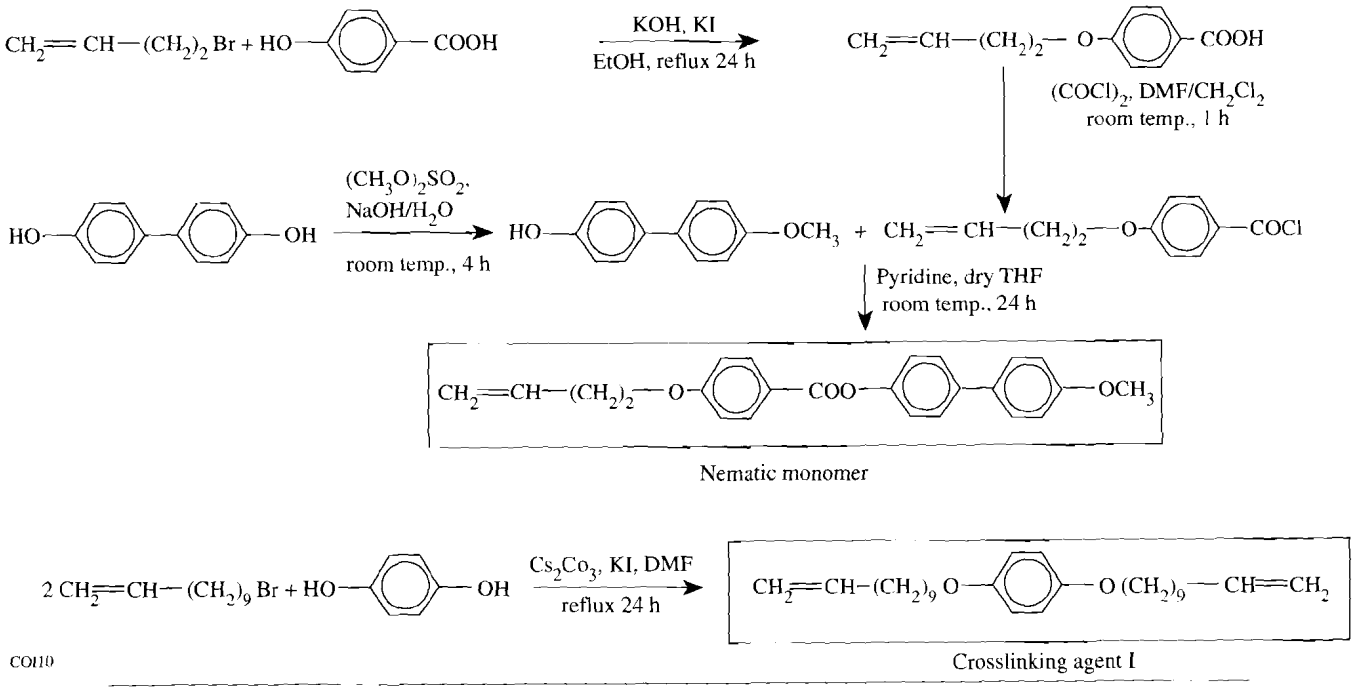

Figure 61.36
Synthesis scheme for the preparation of the nematic monomer and the diacrylate crosslinking agent used for elastomer preparation.

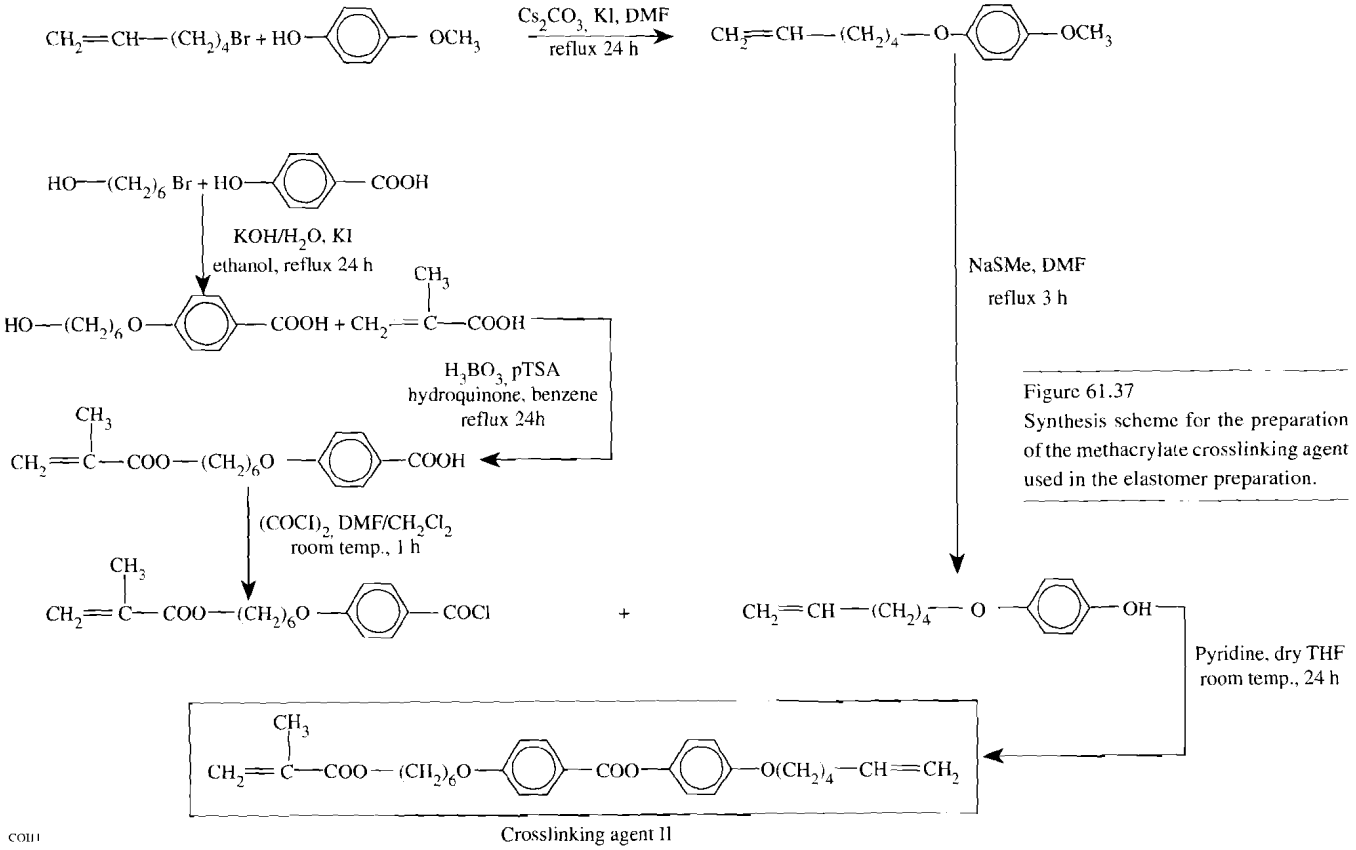

Figure 61.37
Synthesis scheme for the preparation of the methacrylate crosslinking agent used in the elastomer preparation.

2. Preparation of Elastomers

To prepare the elastomers, appropriate quantities of the nematic monomer (NM), the first crosslinking agent (C1), and the second crosslinking agent (C2), as shown in Fig. 61.38, were added to PEHS or PMHS in a round-bottomed reaction flask to ensure a polymer:NM:C1:C2 molar ratio of 1:0.3:0.1:0.1. Upon addition of toluene (13.6 ml/g-material), the flask was sealed, flushed with nitrogen, and heated to ensure dissolution of solids. The catalyst was added ([Pt/CH_2 = CH–] ≈ 0.002), and the flask was shaken vigorously for 30 s before quickly transferring the contents to a heated Teflon™ mold kept overnight at 60°C under a nitrogen purge (first-stage reaction). The elastomer was carefully removed from the mold, stretched by the desired amount, and left for three days on a hot plate at 60°C to complete the elastomer preparation (second-stage reaction). This method of elastomer preparation is similar to that reported by Finkelmann *et al.*,[12] with the exception that a constant *strain*, as opposed to a constant *stress*, was used in our experiments. The extent of reaction was monitored using FTIR spectroscopy. The elastomers prepared from PEHS and PMHS parent polymers were denoted as ES and MS, respectively.

3. Methods of Characterization

The degrees of polymerization of PEHS and PMHS were evaluated from a viscosity versus molecular weight relationship derived from product data (United Chemical Technologies). Infrared spectra of both the parent polymers and the elastomers were obtained using a Nicolet 20SXC FTIR spectrophotometer. Differential scanning calorimetry (DSC) data were collected using a Perkin Elmer DSC-4 at +20°C/min under a helium purge with liquid nitrogen cooling. A hot-stage polarized optical microscope (Leitz Orthoplan-Pol and a Mettler FP52 hot stage) was used for mesophase identification and verification of transition temperatures determined by DSC. Mechanical characterization of elastomers was conducted in a water bath at 55±1°C using an Instron Table Model 1102 instrument. The stress σ is determined in terms of the original cross sectional area, and the strain is defined as $\varepsilon = (l - l_0)/l_0$, where l and l_0 are the length at the time of data collection and original length, respectively.

Two-dimensional, flat-plate x-ray diffraction patterns were collected using a Statton box camera with a sample-to-film distance of 5.0 cm. An image-plate storage phosphor detector was utilized in place of x-ray film to reduce data-collection time.[13] Samples were irradiated with nickel-filtered copper radiation. A qualitative assessment of orientation and liquid crystallinity was accomplished using the flat-plate diffraction data. The x-ray diffraction patterns were obtained with a Rigaku RU-300 pole figure goniometer used in the Bragg-Brentano geometry. This diffractometer was equipped with a copper rotating anode operated at 50 kV and 280 mA, a diffracted-beam nickel filter, and a scintillation detector. Reflection-mode $\theta/2\theta$ scans provided information on planar orientation, while symmetrical transmission-mode $\theta/2\theta$ scans provided a preliminary assessment of in-plane orientation. A quantitative orientation analysis was performed by an azimuthal diffraction technique.[14] Data were collected using the Rigaku RU-300 pole goniometer as mentioned above. Azimuthal analysis involved positioning a sample at a fixed angle θ in the symmetric transmission mode with the detector

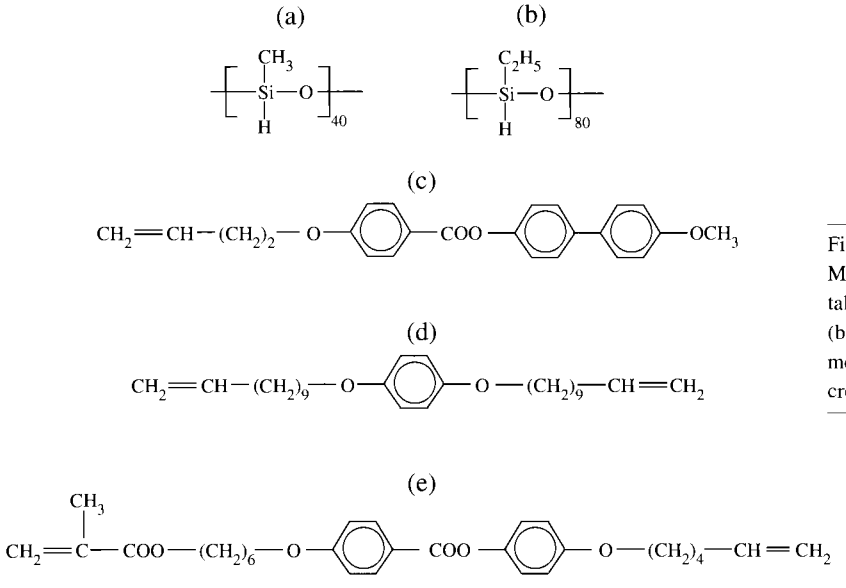

Figure 61.38
Materials used in the preparation of the liquid crystalline elastomers: (a) poly(methylhydrosiloxane); (b) poly(ethylhydro-siloxane); (c) nematic monomer; (d) first crosslinking agent; and (e) second crosslinking agent.

CO12

at a fixed 2θ to detect a desired Bragg diffraction peak. The sample was then rotated 360° around the normal to the sample plane, defined as the χ rotation. In this study the transverse direction was mounted at zero azimuthal angle, i.e., parallel to the plane of the x-ray beam. Azimuthal data allowed the determination of in-plane orientation. Orientation distribution was quantified by the use of the Herman's orientation distribution function (HOF_A) defined for in-plane alignment as[14]

$$HOF_A = \frac{3\langle \cos^2 \chi \rangle - 1}{2} \quad (1)$$

with $\langle \cos^2 \chi \rangle$ defined as

$$\langle \cos^2 \chi \rangle = \frac{\Sigma I(\chi) \sin \chi \cos^2 \chi}{\Sigma I(\chi) \sin \chi}, \quad (2)$$

where $I(\chi)$ denotes intensity as a function of azimuthal angle χ. The value of HOF_A ranges from –0.5 to 1 for in-plane orientation distribution, with a value of –0.5 indicating a perfect alignment of polymer chains along the strain direction, a value of 0 indicating a random or balanced alignment, and a value of 1 indicating perfect alignment of polymer chains along the transverse direction.[14]

Results and Discussion

Fourier transform infrared spectrometry was used to monitor the extent of hydrosilylation reaction, as illustrated in Fig. 61.39 for elastomer MS, where a comparison of scans recorded after the first- [Fig. 61.39(a)] and second-stage [Fig. 61.39(b)] reactions shows the expected reduction in the intensity of the Si-H stretching band at 2160 cm^{-1}. The effect of reaction on the mechanical properties of both the ES and MS elastomers is illustrated in the stress versus strain curves of Fig. 61.40. In light of the reported effect of crosslink density on glass transition (T_g) and liquid-crystal-to-isotropic transition temperatures,[4–11] it is important to ensure that a valid comparison of ES to MS elastomers is made. The crosslink density in terms of the molecular weight between crosslinks, M_c, is related to the elastic modulus E (N/mm^2) at low strains and at temperatures above T_g by Eq. (3):[6]

$$E = \frac{3\rho RT}{M_c}, \quad (3)$$

where ρ is the density estimated at 1.0 g/cm^3,[8,11] R the ideal gas constant, and T the temperature (°K). Since the data were collected at a temperature (55°C) that is above the T_g for all samples considered, Eq. (3) is appropriate for evaluating E from Fig. 61.40. Using Eq. (3), an M_c of 660 g/mole (E = 12.4 N/mm^2) and 560 g/mole (E = 14.6 N/mm^2) were found for the ES and MS elastomers, respectively. Figure 61.37 also shows the expected increase in E (*i.e.*, a decrease in M_c) with an increased extent of reaction. Since samples must be stretched during the second-stage reaction to achieve bulk alignment of the nematic pendant groups, the maximum strain sustained, ε_b, is an important parameter. For our elastomer composition as defined earlier, ES and MS possessed an ε_b value of 0.31 and 0.16, respectively. The difference in ε_b is attributed to the higher molecular weight of the ES system since the degrees of polymerization of the PEHS and PMHS polymers are 80 and 40, respectively.

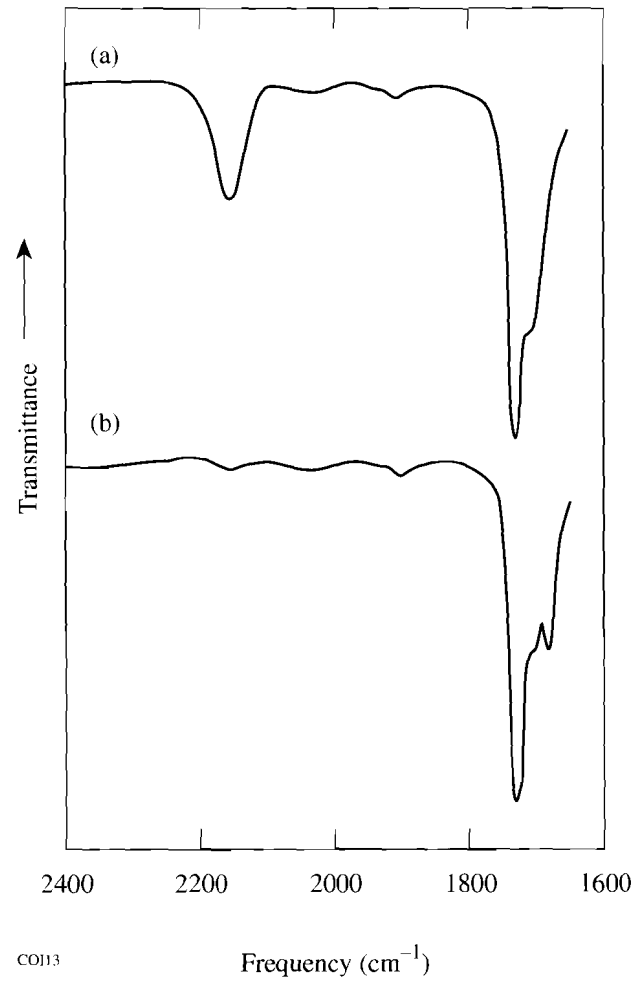

Figure 61.39
FTIR spectra of the MS elastomer after (a) first-stage and (b) second-stage reaction.

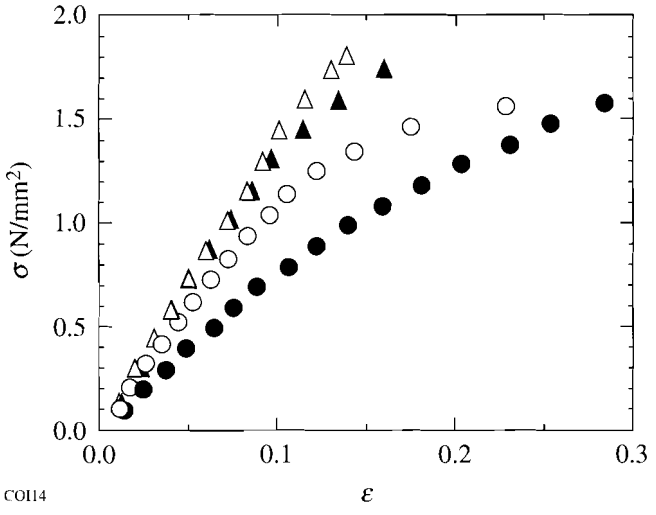

Figure 61.40
Stress (σ) versus strain (ε) recorded at 55°C for MS elastomer after first-stage (▲) and second-stage reaction (△), and ES elastomer after first-stage (●) and second-stage reaction (○).

The DSC thermograms of ES and MS are presented in Fig. 61.41, where the subscripts *s* and *n* refer to samples that were stretched and not stretched, respectively, during the second-stage reaction. Samples described as "stretched" are those that were strained to the fullest possible extent without tearing during the second-stage reaction. Since the glass transitions of pure PEHS and PMHS are −149°C and −140°C, respectively, the substitution and crosslinking reactions would appear to be responsible for the elevated glass transitions of both polymer hosts. This factor is consistent with the increase in E observed in Fig. 61.40. In the first heating scan of the ES elastomer prepared without stretching, an endotherm occurs at 82°C [Fig. 61.41(a)] due to a nematic-to-isotropic transition. A lower value for the transition enthalpy (ΔH) was obtained for an equivalent sample that had been stretched. After the ES sample is heated through this transition temperature and slowly cooled to room temperature, the nematic-isotropic endotherm now appears at 63°C [Fig. 61.38(b)] with a greatly reduced ΔH. If this same ES elastomer sample is instead rapidly cooled to low temperatures (i.e., quenched) from 90°C and then annealed at 60°C, subsequent heating gives an endotherm at 70°C with a ΔH of 1.9 J/g, identical to the value shown in Fig. 61.38(b). These results infer that the ΔH for the nematic-isotropic transition is independent of thermal history applied after the initial heating cycle, while, in contrast, the nematic-isotropic transition temperature ($T_{n\text{-}i}$) displays total thermal history dependence. For the MS elastomer [Fig. 61.41(c)], the endotherm at 80°C is accompanied by a reduced ΔH as compared to the ES elastomer, even though the nematic texture was clearly visible between T_g and 80°C by hot-stage polarizing microscopy. The absence of an endotherm for elastomer MS when the same sample is rescanned [Fig. 61.41(d)] suggests a lack of nematic ordering. Finkelmann *et al.*,[12] however, have reported values for T_g, $T_{n\text{-}i}$, and $\Delta H_{n\text{-}i}$ of 0°C, 83°C, and 1.7 J/g°K, respectively, for the elastomer prepared from PMHS with a degree of polymerization of 120. Other than the differences in the chain length of the starting PMHS and in the

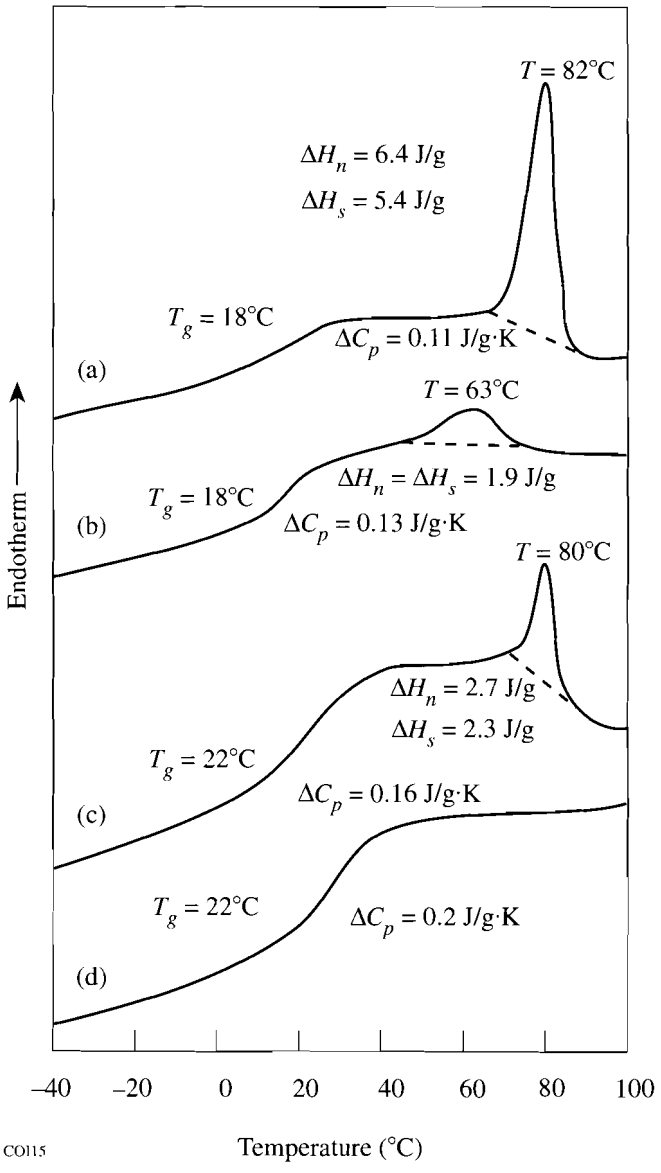

Figure 61.41
DSC thermograms recorded at 20°C/min. of (a) ES elastomer; (b) second heating scan of ES elastomer after the sample was first heated to 90°C and cooled at 5°C/min to room temperature; (c) MS elastomer; and (d) second heating scan of MS elastomer after the sample was heated to 90°C and cooled at 5°C/min to room temperature.

crosslink density, no explanation can be offered for the discrepancy with our experimental results. It appears that the observed values of ΔH_n and ΔH_s of the ES and MS elastomers without any previous thermal history are both greater than those that can be properly accounted for by a typical nematic-to-isotropic transition.

To gain further insights into the relationship between molecular ordering and the endotherms acquired during the first heating scans of the ES and MS elastomers, we turned to x-ray diffraction techniques. The flat-plate diffraction pattern for the unstretched ES sample [Fig. 61.42(a)] shows two broad diffraction rings characteristic of a polydomain nematic, as was also observed for the unstretched MS elastomer. Interplanar spacing calculations reveal that the inner and outer rings have d-spacings of 8.8 Å and 4.38 Å, respectively. Upon stretching the elastomers, in-plane orientation occurs, as evidenced by the formation of arcs in the flat-plate diffraction pattern for the ES elastomer with $\varepsilon = 0.3$ [Fig. 61.42(b)], which is characteristic of a monodomain nematic.[15] Due to the lower sustainable strains in the MS elastomer (see Fig. 61.40), the effect of strain on orientation in this system is not pronounced, as evidenced by the lack of arc formation in the flat-plate camera photographs. In the ES samples, the majority of the diffraction scatter lies in the equatorial position (zeroth order) in the flat-plate pattern, which indicates that the 8.8-Å and 4.38-Å diffraction peaks are of the type ($hk0$). In the following discussion, the term "thermal treatment" indicates that the samples were heated at 90°C for 10 min and then cooled to room temperature. Upon thermal treatment of the stretched ES elastomer, the nematic order is retained, as evidenced by the absence of any discernible effect on arc formation in comparing Figs. 61.42(b) and 61.42(c). In fact, the $\Delta H_{n\text{-}i}$ at 63°C, 1.9 J/g as noted in Fig. 61.41(b), is typical of a nematic-to-isotropic transition. Thus, the $\Delta H_{n\text{-}i}$ observed in Fig. 61.41(a) appears to be caused by a combination of nematic-to-isotropic transition and molecular relaxation.

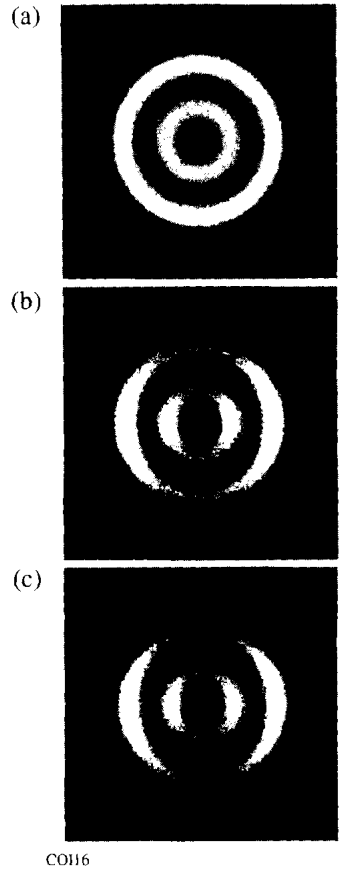

Figure 61.42
Flat-plate x-ray diffraction patterns of ES elastomer: (a) unstretched; (b) stretched to $\varepsilon = 0.3$; and (c) as in (b) but first heated to 90°C and then cooled to room temperature.

Transmission-mode x-ray diffraction data were collected for elastomer ES over a selected range of 2θ, as shown in Fig. 61.43. An inspection of Fig. 61.43 reveals that, for both unstretched [I(a)] and stretched [II(a)] ES samples, the 4.38-Å peak (corresponding to the outer ring shown in Fig. 61.42) observed in the flat-plate diffraction data actually comprises *two* peaks with d-spacings of 4.47 Å and 4.13 Å. The two peaks can be resolved because of the 20-cm sample-to-detector distance, as compared to the 5-cm distance utilized in the flat-plate diffraction work. The intensity of the 4.13-Å peak relative to that of the 4.47-Å peak is clearly diminished by stretching. The 4.13-Å peak disappears with an increase in intensity of the 4.47-Å peak with thermal treatment, as revealed in comparing I(b) to I(a) and II(b) to II(a) (Fig. 61.43). These observations indicate that stretching and thermal treatment may induce some degree of molecular relaxation, consistent with the facts that $\Delta H_n > \Delta H_s$ and that ΔH_n and ΔH_s both decrease to 1.9 J/g upon thermal treatment (see Fig. 61.41).

Azimuthal diffraction data collected on the 4.47-Å peak, as shown in Fig. 61.44, permit a quantitative assessment of molecular relaxation resulting in an enhanced order reflected by the HOF_A parameter defined by Eq. (1). These data suggest that the unstretched ES sample has no in-plane alignment, which implies a near-random distribution of lattice planes based on a HOF_A value of 0.02. For the stretched ES sample, the peaks at 0° and 180° azimuthal positions in Fig. 61.44 (along the sample transverse direction) and a HOF_A value of 0.35 reveal the effect of stretching on the preferred orientation of ($hk0$) lattice planes. Thermal treatment of the stretched sample shows an enhancement of the azimuthal intensity along the transverse direction, resulting in an increased HOF_A value of 0.43 apparently due to the alignment of nematic domains. To be consistent with the observed order in which the HOF_A value

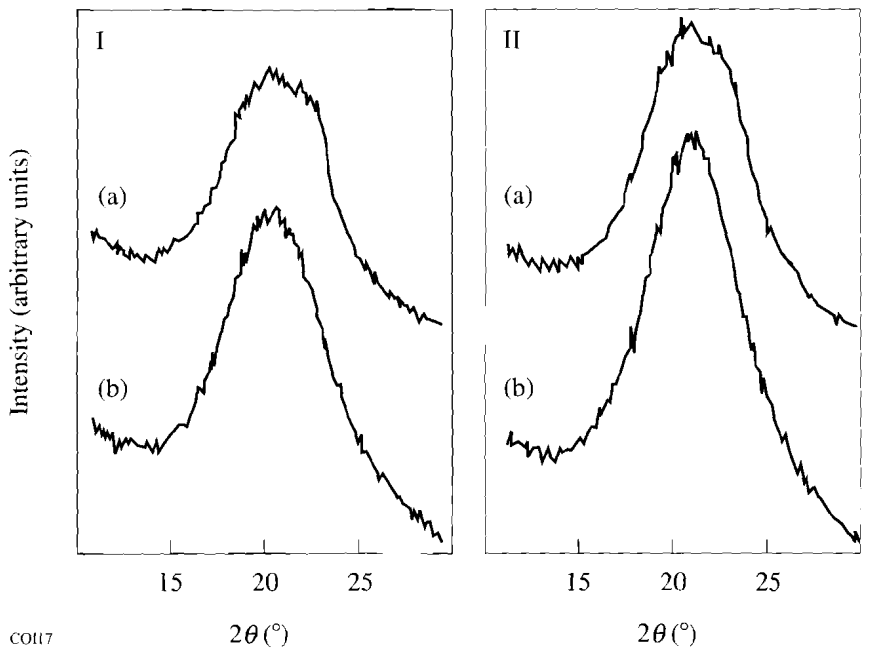

Figure 61.43
X-ray diffraction patterns of ES elastomer: I(a) unstretched, no thermal processing; I(b) sample I(a) heated at 90°C for 10 min and by cooled to room temperature; II(a) stretched to $\varepsilon = 0.3$, no thermal processing; II(b) stretched as in II(a) followed by heating at 90°C for 10 min and cooled to room temperature.

increases upon stretching and thermal treatment, the DSC thermograms in Figs. 61.41(a) and 61.41(b) should be interpreted in terms of stored enthalpy at the molecular scale that is released to some extent by stretching during the second-stage reaction and completely released by thermal treatment. This mode of enthalpy storage does not seem to contribute to the experimentally quantified HOF_A parameter on a relatively macroscopic scale in the case of nematic ordering.

From the x-ray diffraction and thermal analysis data reviewed above, we can make several observations regarding the effect of processing on mesomorphic behavior:

- Based on the flat-plate x-ray diffraction pattern, an imposed strain gives rise to a monodomain nematic character, whereas a polydomain character is observed in the absence of applied strain. Furthermore, the monodomain character achieved with the application of strain is retained when the sample is heated above the nematic-isotropic transition temperature and cooled back to room temperature.

- The DSC thermograms, coupled with the transmission-mode x-ray diffraction data, suggest that (a) enthalpy is stored in the freshly prepared elastomer; (b) the imposed strain helps to release the stored enthalpy to some extent; and (c) the stored enthalpy is almost completely released upon thermal cycling between the nematic-isotropic transition and room temperature.

- The transmission mode and azimuthal x-ray diffraction data demonstrate that, although the stored enthalpy does not lead to an increased order parameter (HOF_A), the enthalpy is released through molecular relaxation upon stretching or thermal treatment. This enthalpy release appears to enhance nematic ordering and increase HOF_A values.

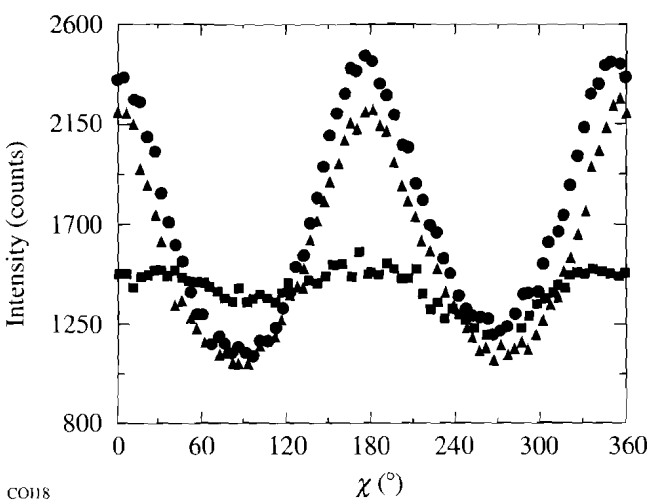

Figure 61.44
X-ray diffraction azimuth plots for ES elastomer at $2\theta = 19.8°$, i.e., the 4.47-Å peak in Fig. 61.40: unstretched (■), stretched to $\varepsilon = 0.3$ (▲), and stretched to $\varepsilon = 0.3$ (●) while heating at 90°C for 10 min followed by cooling to room temperature.

Summary

Liquid crystalline elastomers derived from siloxane polymers, PMHS and PEHS, were prepared following a two-stage reaction scheme to investigate the effects of processing conditions and thermal treatment on mesomorphic characteristics. A thorough analysis of these elastomers by a combination of FTIR, DSC, mechanical analysis, polarized hot-stage optical microscopy, and x-ray diffraction techniques has shown that the chain length of the precursor siloxane polymer plays an important role in achieving bulk alignment via stretching during the second-stage reaction. The imposed strain was also demonstrated to be critical in achieving a monodomain nematic character, which is completely recoverable after repeated thermal cycling from $T_{n\text{-}i}$ to room temperature. The latter feature is especially important in the preparation of freestanding, optical-quality birefringent films for laser and other optical device applications.

ACKNOWLEDGMENT

This work was supported in part by the Army Research Office under Contract #DAAL03-92-G-0147, the Contact Lens Division of Bausch & Lomb, Inc., the U.S. Department of Energy Office of Inertial Confinement Fusion under Cooperative Agreement No. DE-FC03-92SF19460, and the University of Rochester. The support of DOE does not constitute an endorsement by DOE of the views expressed in this article. The authors would like to thank Craig Barnes of Eastman Kodak Company for assistance in gathering the x-ray data, Eric J. Leibenguth and Linda Slapelis of Bausch & Lomb for assistance in the stress-strain analysis, Dr. Jay F. Kunzler of Bausch & Lomb for helpful discussions, Darin Phelps of the Department of Chemical Engineering for assistance in monomer synthesis, and Professor Burns of the Department of Mechanical Engineering, University of Rochester for helpful discussions.

REFERENCES

1. (a) H. Finkelmann, Angew. Chem. Int. Ed. Engl. **26**, 816 (1987); (b) H. Finkelmann, in *Liquid Crystallinity in Polymers: Principles and Fundamental Properties*, edited by A. Ciferri (VCH Publishers, New York, 1991), p. 315.
2. G. W. Gray, in *Side Chain Liquid Crystal Polymers*, edited by B. McArdle (Chapman and Hall, New York, 1989), p. 106.
3. V. Percec and Q. Zheng, J. Mater. Chem. **2**, 475 (1992).
4. J. Schätzle and H. Finkelmann, Mol. Cryst. Liq. Cryst. **142**, 85 (1987).
5. W. Gleim and H. Finkelmann, in *Side Chain Liquid Crystal Polymers*, edited by C. B. McArdle (Chapman and Hall, New York, 1989), p. 287.
6. F. J. Davis, J. Mater. Chem. **3**, 551 (1993).
7. M. Brehmer and R. Zentel, Mol. Cryst. Liq. Cryst. **243**, 353 (1994).
8. T. Tsutsui and R. Tanaka, Polymer **22**, 117 (1981).
9. (a) R. Zentel and M. Benalia, Makromol. Chem. **188**, 665 (1987); (b) R. Zentel and G. Reckert, Makromol. Chem. **187**, 1915 (1986).
10. H. Loth and A. Euschen, Makromol. Chem., Rapid Commun. **9**, 35 (1988).
11. (a) J. Küpfer and H. Finkelmann, Macromol. Chem. Phys. **195**, 1353 (1994); (b) J. Schätzle, W. Kaufhold, and H. Finkelmann, Makromol. Chem. **190**, 3269 (1989); (c) H. Finkelmann, H.-J. Kock, and G. Rehage, Makromol. Chem., Rapid Commun. **2**, 317 (1981).
12. J. Küpfer and H. Finkelmann, Makromol. Chem., Rapid Commun. **12**, 717 (1991).
13. T. N. Blanton, in *Advances in X-Ray Analysis* (Plenum Press, New York, in press), Vol. 37.
14. L. E. Alexander, *X-Ray Diffraction Methods in Polymer Science* (Wiley-Interscience, New York, 1969).
15. J. Falgueirettes and P. DeLord, in *Liquid Crystals & Plastic Crystals, Vol 2: Physicochemical Properties and Methods of Investigation*, edited by G. W. Gray and P. A. Winsor (Halsted Press, New York, 1974), p. 63.

Publications and Conference Presentations

Publications

S. Augst and D. D. Meyerhofer, "Field Ionization of Noble Gas Atoms with a Keldysh Adiabaticity Parameter of One," Laser Phys. **4**, 1155 (1994).

R. Betti, V. Goncharov, R. L. McCrory, E. Turano, and C. P. Verdon, "Multiple Cutoff Wave Numbers of the Ablative Rayleigh-Taylor Instability," Phys. Rev. E. **50**, 3968 (1994).

X. D. Cao and D. D. Meyerhofer, "All-Optical Switching Via Collisions of Spatial Vector Solitons," Opt. Lett. **19**, 1711 (1994).

X. D. Cao and D. D. Meyerhofer, "Frequency-Domain Interferometer for Measurement of the Polarization Mode Dispersion in Single-Mode Optical Fibers," Opt. Lett. **19**, 1837 (1994).

X. D. Cao, D. D. Meyerhofer, and G. P. Agrawal, "Optimization of Optical Beam Steering in Nonlinear Kerr Media Via Spatial Phase Modulation," J. Opt. Soc. Am. B **11**, 2224 (1994).

W. R. Donaldson and L. Mu, "Effect of Illumination Uniformity on GaAs Photoconductive Switches," IEEE J. Quantum Electron. **30**, 2866 (1994).

W. Gob, W. Lang, W. Kula, and R. Sobolewski, "Transport Properties and Superconducting Fluctuations in Oxygen Deficient Y-Ba-Cu-O Thin Films," Physica C **235–240**, 1535 (1994).

D. Gupta, W. R. Donaldson, and A. M. Kadin, "Energy Extraction from Superconducting Magnets Using Optically Activated YBa2Cu_3O_{7-x} Switches," in *Optically Activated Switching IV*, edited by W. R. Donaldson (SPIE, Bellingham, WA, 1994), Vol. 2343, pp. 128–134.

S. D. Jacobs, K. L. Marshall, and A. Schmid, "Liquid Crystals for Laser Applications," in CRC Handbook of Laser Science and Technology, Supplement 2: Optical Materials, edited by M. J. Weber (CRC Press, Boca Raton, FL, 1995), Sec. 14, pp. 509–577.

W. Kula and R. Sobolewski, "Effect of Hydrogen Doping on Electrical Properties of Y-Ba-Cu-O Thin Films," Physica C **235–240**, 587 (1994).

Y. Lin and T. J. Kessler, "Raman Scattering in Air: Four-Dimensional Analysis," Appl. Opt. **33**, 4781 (1994).

K. Mizuno, R. Bahr, B. S. Bauer, R. S. Craxton, J. S. DeGroot, R. P. Drake, W. Seka, and B. Sleaford, "Direct Measurements of the Ion Acoustic Decay Instability in a Laser-Produced, Large-Scale, Hot Plasma," Phys. Rev. Lett. **73**, 2704 (1994).

L. Mu, W. R. Donaldson, J. C. Adams, and R. A. Falk, "Electromagnetic Wave Interaction with Laser-Induced Plasmas in GaAs," in *Optically Activated Switching IV*, edited by W. R. Donaldson (SPIE, Bellingham, WA, 1994), Vol. 2343, pp. 107–112.

H. Shi and S.-H. Chen, "Novel Glassy Nematic and Chiral Nematic Oligomers Derived from 1,3,5-Cyclohexanetricarboxylic and (1R,3S)-(+)-Camphoric Acids," Liq. Cryst. **17**, 413 (1994).

M. D. Skeldon, A. Okishev, S. A. Letzring, W. R. Donaldson, K. Green, and W. Seka, "Optically Activated Switches for the Generation of Complex Electrical Waveforms with Multigigahertz Bandwidth," in *Optically Activated Switching IV*, edited by W. R. Donaldson (SPIE, Bellingham, WA, 1994), Vol. 2343, pp. 94–98.

B. Yaakobi, R. Epstein, F. J. Marshall, D. K. Bradley, P. A. Jaanimagi, and Q. Su, "New Diagnostic Features in the Laser Implosion of Argon-Filled Targets," Opt. Commun. **111**, 556 (1994).

Forthcoming Publications

M. S. Adams, M. V. Fedorov, V. P. Krainov, and D. D. Meyerhofer, "Comparison of Quasiclassical and Exact Dipole Moments for Bound-Free Transitions in Hydrogen," to be published in Physical Review A.

U. Alon, J. Hecht, D. Ofer, and D. Shvarts, "Power Laws and Similarity of Rayleigh-Taylor and Richtmyer-Meshkov Mixing Fronts at All Density Ratios," to be published in Physical Review Letters.

R. Betti and J. P. Freidberg, "Stability Analysis of Resistive Wall Kink Modes in Rotating Plasmas," to be published in Physical Review Letters.

T. R. Boehly, R. S. Craxton, T. H. Hinterman, J. H. Kelly, T. J. Kessler, S. A. Kumpan, S. A. Letzring, R. L. McCrory, S. F. B. Morse, W. Seka, S. Skupsky, J. M. Soures, and C. P. Verdon, "The Upgrade to the OMEGA Laser System," to be published in the Review of Scientific Instruments.

T. R. Boehly, R. S. Craxton, T. H. Hinterman, P. A. Jaanimagi, J. H. Kelly, T. J. Kessler, R. L. Kremens, S. A. Kumpan, S. A. Letzring, R. L. McCrory, S. F. B. Morse, W. Seka, S. Skupsky, J. M. Soures, and C. P. Verdon, "The Upgrade to the OMEGA Laser System," to be published in the Proceedings of the American Nuclear Society.

D. K. Bradley, P. M. Bell, O. L. Landen, J. D. Kilkenny, and J. Oertel, "Development and Characterization of a Pair of 30–40 ps X-Ray Framing Cameras," to be published in the Review of Scientific Instruments.

X. D. Cao and D. D. Meyerhofer, "Optimization of Pulse Shaping Using Nonlinear Polarization Rotation," to be published in Optical Communication.

X. D. Cao, L. Zheng, and D. D. Meyerhofer, "A Novel Method for the Measurement of Temporal Walk-Off of Short Pulses in Nonlinear Crystals," to be published in Optics Letters.

S. H. Chen and S. Krishnamurthy, "Some Fundamental Issues Governing Thermotropic Chiral Nematic Copolymers," to be published in the Proceedings of the 42nd Society for Polymer Science, Kyoto, Japan, 31 May–2 June 1993.

C. Y. Chien, G. Korn, J. S. Coe, J. Squier, G. Mourou, and R. S. Craxton, "Highly Efficient Second-Harmonic Generation of Ultra-Intense Nd:Glass Laser Pulses," to be published in Optics Letters.

C. T. Cotton, "The Design of an All-Spherical, Three-Mirror, Off-Axis Telescope Objective," to be published in the OSA Proceedings of the International Optical Design Conference '94.

M. J. Cumbo, D. Fairhurst, S. D. Jacobs, and B. E. Puchebner, "Slurry Particle Size Evolution during the Polishing of Optical Glass," to be published in Applied Optics.

D. Fried, R. E. Glena, J. D. B. Featherstone, and W. Seka, "The Nature of Light Scattering in Dental Enamel and Dentin at Visible and Near Infrared Wavelengths," to be published in Applied Optics.

R. E. Giacone, C. J. McKinstrie, and R. Betti, "Angular Dependence of Stimulated Brillouin Scattering in Homogeneous Plasma," to be published in Physics of Plasmas.

D. Gupta, W. R. Donaldson, and A. M. Kadin, "Rapid Flux Motion and Critical State Dynamics in a Superconducting Disk," to be published in the Journal of Applied Physics.

D. A. Haynes, C. F. Hooper, R. C. Mancini, D. K. Bradley, J. Delettrez, R. Epstein, and P. A. Jaanimagi, "Spectroscopic Analysis of Ar-Doped Laser Driven Implosions," to be published in the Review of Scientific Instruments.

J. Hecht, D. Ofer, U. Alon, D. Shvarts, S. A. Orszag, and R. L. McCrory, "Three-Dimensional Simulations and Analysis of the Nonlinear Stage of the Rayleigh-Taylor Instability," to be

published in Laser and Particle Beams.

P. A. Jaanimagi, R. C. Elton, B. L. Welch, Y. Leng, and H. R. Griem, "Extending X-Ray Streak Camera Operation to VUV Wavelengths," to be published in the Review of Scientific Instruments.

J. P. Knauer, R. L. Kremens, M. A. Russotto, and S. Tudman, "Using Cosmic Rays to Monitor Large Scintillator Arrays," to be published in the Review of Scientific Instruments.

E. M. Korenic, K. L. Marshall, and J. A. Maiolo, "Blending Polysiloxane 'Glass Resins' to Produce Optical Films with a Specific Refractive Index," to be published in Optics and Photonics News.

Y. Kostoulas, L. J. Waxer, I. A. Walmsley, G. W. Wicks, and P. M. Fauchet, "Femtosecond Carrier Dynamics in Low-Temperature-Grown Indium Phosphide," to be published in Applied Physics Letters.

W. Lang, W. Gob, W. Kula, and R. Sobolewski, "Anisotropic Magnetoresistance in the Normal State of Oxygen-Deficient $YBa_2Cu_3O_{7-x}$ Thin Films Induced by Superconducting Fluctuations," to be published in Physica B.

W. Lang, G. Heine, W. Kula, and R. Sobolewski, "Study of Superconducting Fluctuations in $Bi_2Sr_2Ca_2Cu_3O_x$ Thin Films: Paraconductivity, Excess Hall Effect, and Magneto-conductivity," to be published in Zeitschrift Fur Physik B.

Y. Lin, T. J. Kessler, and G. Lawrence, "Distributed Phase Plates for Supergaussian Focal-Plane Irradiance Profiles," to be published in Optics Letters.

F. J. Marshall and B. Yaakobi, "Quantitative Measurements with X-Ray Microscopes in Laser-Fusion Experiments," to be published in the Review of Scientific Instruments.

K. L. Marshall, S. D. Jacobs, and J. E. Miller, "Mid-Infrared Modulation Using Field-Induced Scattering in Ferroelectric Liquid Crystals," to be published in Applied Optics.

J. C. Mastrangelo, T. N. Blanton, and S.-H. Chen, "Crystallization upon Thermal Annealing of a Glass-Forming Liquid Crystal in the Nematic Regime," to be published in Applied Physics Letters.

R. L. McCrory, "Progress Toward Ignition with Direct Drive," to be published in Concerning Major Systems in Science and Technology.

R. L. McCrory, J. M. Soures, C. P. Verdon, T. R. Boehly, D. K. Bradley, R. S. Craxton, J. A. Delettrez, R. Epstein, P. A. Jaanimagi, S. D. Jacobs, R. L. Keck, J. H. Kelly, T. J. Kessler, H. Kim, J. P. Knauer, R. L. Kremens, S. A. Kumpan, S. A. Letzring, F. J. Marshall, P. J. McKenty, S. F. B. Morse, A. Okishev, W. Seka, R. W. Short, M. D. Skeldon, S. Skupsky, M. Tracy, and B. Yaakobi, "Direct-Drive Laser Fusion Experimental Program at the University of Rochester Laboratory for Laser Energetics," to be published in the Proceedings of the Conference on Plasma Physics and Controlled Nuclear Fusion Research.

C. J. McKinstrie, R. Betti, R. E. Giacone, T. Kolber, and E. J. Turano, "Two-Dimensional Stimulated Scattering of Short Laser Pulses," to be published in Physical Review E.

J. Peatross and D. D. Meyerhofer, "Intensity-Dependent Atomic Phase Effects in High-Order Harmonic Generation," to be published in Physical Review A.

J. Z. Roach, A. Ninkov, S. W. Swales, and T. Morris, "Design and Evaluation of a Screen CCD Imaging System," to be published in Optical Engineering.

W. Seka, D. Fried, J. D. B. Featherstone, and S. F. Borzillary, "Light Deposition and Thermal Response in Dental Hard Tissue," to be published in the Journal of Dental Research.

H. Shi and S.-H. Chen, "Novel Glass-Forming Liquid Crystals. 2. Systems Containing High Optical Birefringence Moiety 1-(Phenyl)-2-(6-Cyanonaphth-2-yl)Ethyne," to be published in Liquid Crystals.

H. Shi and S.-H. Chen, "Effects of Stereochemistry, Mesogenic Core, and Space Length on Crystallization from Nematic and Isotropic Melts of Cyclohexane-Based, Glass-Forming Liquid Crystals," to be published in Liquid Crystals.

D. Shvarts, U. Alon, D. Ofer, R. L. McCrory, and C. P. Verdon, "Nonlinear Evolution of Multimode Rayleigh-Taylor Instability in Two and Three Dimensions," to be published in Physics of Plasmas.

M. D. Skeldon, "Transverse Modulational Instabilities in the Presence of Stimulated Rotational Raman Scattering with a High-Energy Laser," to be published in Optics Letters.

R. Sobolewski and T. Y. Hsiang, "Progress in Ultrafast Superconducting Electronics," to be published in the Proceedings of the International Workshop on Superconductivity and Particle Detection. (invited)

C. J. Twomey, T. N. Blanton, K. L. Marshall, S. H. Chen, and S. D. Jacobs, "Some Dynamic Features of the Preparation of Liquid Crystalline Elastomers," to be published in Liquid Crystals.

C. P. Verdon and R. L. McCrory, "Direct-Drive Capsule Physics," to be published in the Proceedings of ECLIM '94.

C.-C. Wang, M. Currie, R. Sobolewski, and T. Y. Hsiang, "Subpicosecond Electrical Pulse Generation by Edge Illumination of Silicon and Indium Phosphide Photoconductive Switches," to be published in Applied Physics Letters.

C.-C. Wang, M. Currie, D. Jacobs-Perkins, M. J. Feldman, R. Sobolewski, and T. Y. Hsiang, "First Direct Observation of Single-Flux-Quantum Pulses," to be published in Appled Physics Letters.

M. D. Wittman, R. Q. Gram, H. Kim, C. K. Immesoete, S. G. Noyes, and S. Scarantino, "Increased Retention Time for Hydrogen and Other Gases by Polymer Shells Using Optically Transparent Aluminum Layers," to be published in the Journal of Vacuum Science and Technology.

B. Yaakobi, Q. Su, F. J. Marshall, and R. Epstein, "Monochromatic Backlighting as a Laser-Fusion Diagnostic," to be published in the Journal of X-Ray Science and Technology.

B. Yaakobi, D. Shvarts, F. J. Marshall, R. Epstein, and Q. Su, "Target Imaging and Backlighting Diagnosis," to be published in the Review of Scientific Instruments.

B. Yaakobi, R. Epstein, F. J. Marshall, D. K. Bradley, P. A. Jaanimagi, and Q. Su, "New Diagnostic Features in the Laser Implosion of Argon-Filled Targets," to be published in the Review of Scientific Instruments.

B. Yaakobi, D. Shvarts, R. Epstein, and Q. Qu, "X-Ray Backlighting Imaging of Mixed Imploded Targets," to be published in the Journal of Applied Physics.

M. Yu, C. J. McKinstrie, and G. P. Agrawal, "Modulational Instabilities in Dispersion-Flattened Fibers," to be published in Physical Review E.

L. Zheng and D. D. Meyerhofer, "A Linear Cross-Correlation Technique for Single-Shot Measurements of Weak Light Pulses," to be published in Optics Letters.

X. Zhou, S. Alexandrou, and T. Y. Hsiang, "Monte Carlo Investigation of the Mechanism of Subpicosecond Pulse Generation by Nonuniform Gap Illumination," to be published in Applied Physics Letters.

J. D. Zuegel and W. Seka, "Direct Measurements of Lower-Level Lifetime in Nd:YLF," to be published in the Bulletin of the American Physical Society.

Conference Presentations

The following presentations were made at the OSA Annual Meeting/ILS-X '94, Dallas, TX, 2–7 October 1994:

W. I. Kordonsky and S. D. Jacobs, "Optical Finishing with Magnetorheological Fluids."

D. D. Meyerhofer, C. Bamber, T. Blalock, S. Boege, T. Kotseroglou, and A. C. Melissinos, "1-Hz, 1-ps, Terawatt, Chirped Pulse Amplification Laser System with a Nd:Glass Slab Amplifier."

C. I. Moore, J. P. Knauer, and D. D. Meyerhofer, "Relativistic Ponderomotive Acceleration of Electrons from a Laser Focus."

J. D. Zuegel and W. Seka, "Direct Measurements of Lower-Level Lifetime in Nd:YLF."

S. H. Chen, "Novel Low Molar Mass Glass-Forming Liquid Crystals: Synthesis, Characterization, and Morphological

Stability," 43rd Symposium on Macromolecules, Fukuoka, Japan, 12 October 1994.

The following presentations were made at the 1994 Applied Superconductivity Conference, Boston, MA, 16–21 October 1994:

M. Currie, C.-C. Wang, D. Jacobs-Perkins, R. Sobolewski, and T. Y. Hsiang, "An Optoelectronic Testing System of Rapid, Single-Flux Quantum Circuits."

D. Gupta, W. R. Donaldson, and A. M. Kadin, "Transient Flux Dynamics in Optically Irradiated YBCO Thin Film Switches."

W. Kula, W. Xiong, R. Sobolewski, and J. Talvacchio, "Laser Patterning of $YBa_2Cu_3O_x$ Thin Films Protected by *in-situ* Grown $SrTiO_3$ Cap Layer."

C.-C. Wang, M. Currie, and T. Y. Hsiang, "Ultrafast, Integrable, Optics-Based Interface between Superconducting and Room-Temperature Electronics."

C.-C. Wang, M. Currie, D. Jacobs-Perkins, L. Shi, and T. Y. Hsiang, "Picosecond Cryogenic Nb/Si/Nb Metal-Semiconductor-Metal (MSM) Photodiode on Superconducting Microstrip Transmission Lines."

W. Xiong, M. Currie, W. Kula, and R. Sobolewski, "Thin-Film YBCO Photodetectors Based on Oxygen-Depleted Structures."

The following presentations were made at the XXVI Annual Symposium on Optical Materials for High Power Lasers, Boulder, CO, 24–26 October 1994:

S. S. Papernov and A. W. Schmid, "A Comparison of Laser-Induced Damage Micromorphology in Three Model Thin-Film Systems: HfO_2, Y_2O_3, and Ta_2O_5."

D. J. Smith, J. F. Anzellotti, A. W. Schmid, S. Papernov, Z. R. Chrzan, and S. J. Van Kerkhove, "Damage Fluence at 1054 nm and 351 nm of Coatings Made with Hafnium Oxide Evaporated from Metallic Hafnium."

M. D. Wittman, H. Kim, and A. S. Chow, "Determination of the Wall Thickness and Uniformity of Inertial-Fusion Capsules Using the Self-Interference Fringes Produced with Narrow-Bandwidth Illumination," 41st National Symposium of the American Vacuum Society, Denver, CO, 24–28 October 1994.

The following presentations were made at LEOS '94 7th Annual Meeting, Boston, MA, 31 October–3 November 1994:

W. R. Donaldson, L. Mu, D. Jacobs-Perkins, and T. Y. Hsiang, "Two-Dimensional Electro-Optic Sampling in GaAs Photoconductive Switches."

Y. Kostoulas, K. B. Ucer, L. Waxer, G. W. Wicks, I. A. Walmsley, and P. M. Fauchet, "Ultrafast Carrier Lifetime in Low-Temperature-Grown GaAs, InP, and InGaP."

The following presentations were made at SPIE's International Symposium on Photonic Sensors & Controls for Commercial Applications, Boston, MA, 31 October–4 November 1994:

D. Gupta, W. R. Donaldson, and A. M. Kadin, "Energy Extraction from Superconducting Magnets Using Optically Activated $YBa_2Cu_3O_{7-x}$ Switches."

L. Mu, W. R. Donaldson, J. C. Adams, and R. A. Falk, "Electromagnetic Wave Interaction with Laser-Induced Plasmas in GaAs."

M. D. Skeldon, A. Okishev, S. A. Letzring, W. R. Donaldson, K. Green, and W. Seka, "Optically Activated Switches for the Generation of Complex Electrical Waveforms with Multigigahertz Bandwidth."

The following presentations were made at the 36th Annual Meeting, APS Division of Plasma Physics, Minneapolis, MN, 7–11 November 1994:

R. Betti, H. L. Berk, and J. P. Freidberg, "Theory of the Beta-Induced Alfven Eigenmode."

R. Betti and J. P. Freidberg, "The Effect of Plasma Rotation on the Resistive Wall Mode."

T. R. Boehly, R. S. Craxton, P. A. Jaanimagi, J. H. Kelly, T. J. Kessler, R. L. Kremens, S. A. Kumpan, S. A. Letzring, R. L.

McCrory, S. F. B. Morse, W. Seka, S. Skupsky, J. M. Soures, M. D. Tracy, and C. P. Verdon, "Initial Performance Results from the Upgraded OMEGA Laser."

A. V. Chirokikh, W. Seka, R. E. Bahr, R. S. Craxton, R. W. Short, A. Simon, and M. D. Skeldon, "Observations and Simulation of Stimulated Brillouin Scattering in Long-Scale-Length Laser Plasmas."

R. S. Craxton, M. Dunne, and O. Willi, "Competition between Target Self-Emission and Soft X-Ray Backlighting."

S. Cremer, J. P. Knauer, R. L. Kremens, M. A. Russotto, D. Shvarts, S. Skupsky, and C. P. Verdon, "Relation of Primary- to Secondary-Reaction Products to the Final Core Parameters of Pure Deuterium Targets in Laser Fusion Experiments."

J. A. Delettrez, D. K. Bradley, and C. P. Verdon, "A Mix Model in *LILAC* for the Linear and Weakly Nonlinear Regimes of the Rayleigh-Taylor Instability."

E. M. Epperlein and R. W. Short, "Nonlocal Electron Transport in the Presence of High-Intensity Laser Irradiation."

R. Epstein, J. A. Delettrez, C. P. Verdon, D. Shvarts, and B. Yaakobi, "Simulations of Spectral Signatures and Images of Core-Shell Mixing in Laser-Driven Implosions."

R. E. Giacone, C. J. McKinstrie, T. Kolber, and R. Betti, "Two-Dimensional Stimulated Brillouin Scattering."

V. Goncharov, R. Betti, R. L. McCrory, and C. P. Verdon, "The Effect of Thermal Conduction on the Ablative Rayleigh-Taylor Instability."

J. P. Knauer, P. W. McKenty, C. P. Verdon, S. G. Glendinning, S. V. Weber, D. M. Pennington, and R. J. Wallace, "Growth of Low-Amplitude Mass Perturbations due to the Rayleigh-Taylor Instability."

T. Kolber, C. J. McKinstrie, R. Betti, and R. E. Giacone, "The Effects of Realistic Geometry on Two-Dimensional Stimulated Brillouin Scattering."

R. L. Kremens, M. A. Russotto, and S. Tudman, "Simulation of 'Saturated' Operation of the MEDUSA Neutron Detector Array."

J. S. Li, C. J. McKinstrie, C. Joshi, and K. Marsh, "Thermal Filamentation of Counterpropagating Laser Beams."

F. J. Marshall, A. Hauer, J. Oertel, and R. Watt, "Monochromatic X-Ray Imaging of Laser-Fusion Targets."

C. J. McKinstrie, R. Betti, R. E. Giacone, and T. Kolber, "Stimulated Raman Scattering of Short Pulse Lasers."

W. Seka, A. V. Chirokikh, R. S. Craxton, R. E. Bahr, C. Labaune, H. A. Baldis, N. Renard, E. Schifano, A. Michard, S. Baton, B. Bauer, K. Baker, R. P. Drake, and K. Estabrook, "Stimulated Brillouin Scattering in Long-Scale-Length, Preformed Plasmas at 1 mm: Experiments and Simulations."

R. W. Short, "Smoothing of Speckle Irradiation Patterns by Temporal Evolution of the Target Corona."

D. Shvarts, U. Alon, D. Ofer, J. Hecht, R. L. McCrory, and C. P. Verdon, "Nonlinear Evolution of Multi-Mode Rayleigh-Taylor and Richtmyer-Meshkov Instabilities in Two and Three Dimensions."

A. Simon and R. W. Short, "Parametric Instability of Bernstein and Fluid Modes in Laser-Produced Plasma."

E. J. Turano, C. J. McKinstrie, and W. L. Kruer, "Relativistic Saturation of Forward Stimulated Raman Scattering."

T. R. Boehly, R. S. Craxton, T. H. Hinterman, P. A. Jaanimagi, R. L. Keck, J. H. Kelly, T. J. Kessler, R. L. Kremens, S. A. Kumpan, S. A. Letzring, R. L. McCrory, S. F. B. Morse, W. Seka, S. Skupsky, J. M. Soures, and C. P. Verdon, "The Upgrade to the OMEGA Laser System," IAEA, Paris, France, 14–18 November 1994.

UNIVERSITY OF
ROCHESTER